International Journal of Chemical Engineering

Recent Advances in Fuel Cells as Complex Energy Systems

Lead Guest Editor: Mohammad Hossein Ahmadi
Guest Editors: Pouria Ahmadi, Mamdouh H. Assad, and Emin Açıkkalp

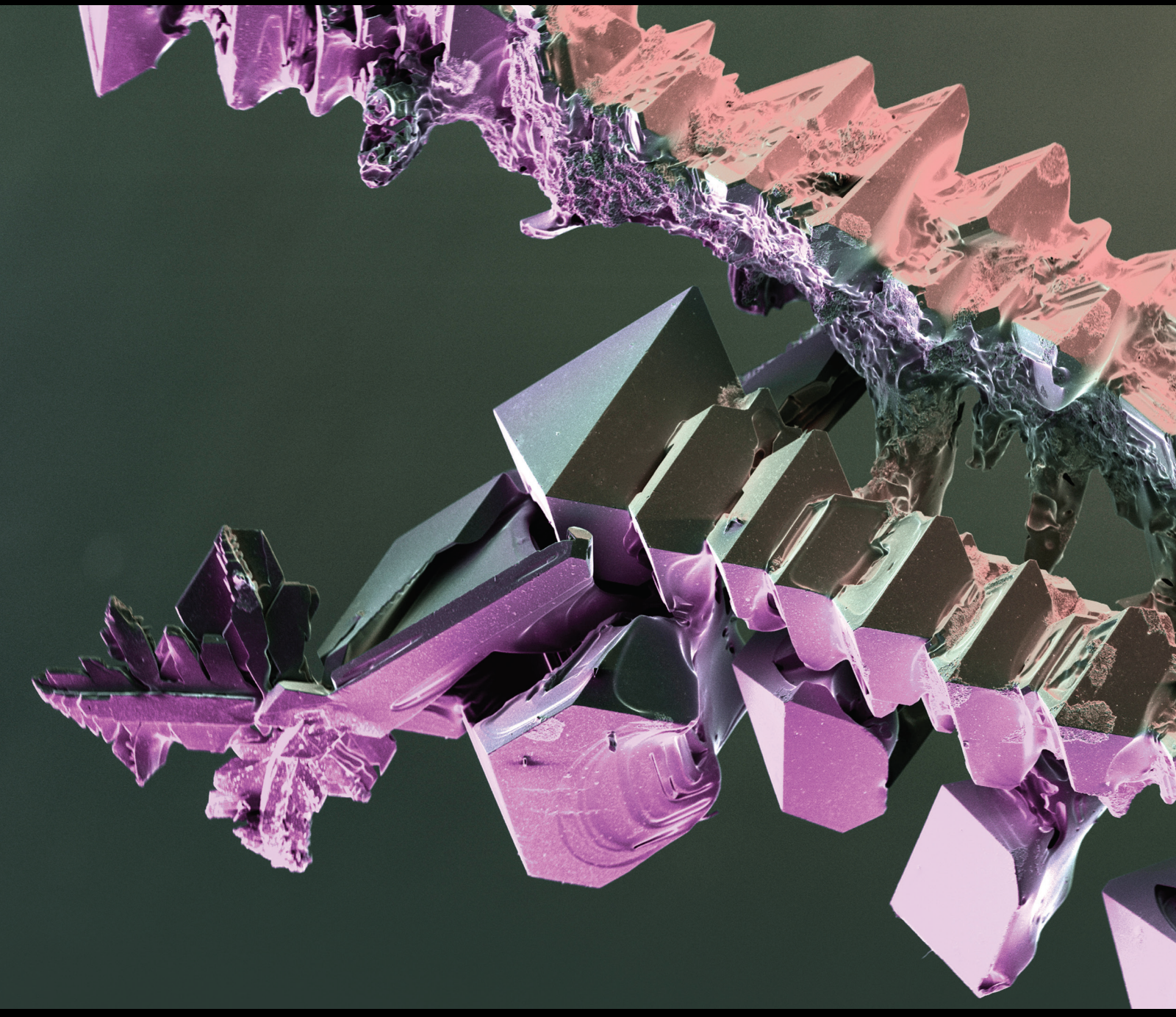

Recent Advances in Fuel Cells as Complex Energy Systems

International Journal of Chemical Engineering

Recent Advances in Fuel Cells as Complex Energy Systems

Lead Guest Editor: Mohammad Hossein Ahmadi
Guest Editors: Pouria Ahmadi, Mamdouh H. Assad, and Emin Açıkkalp

Contents

Hindawi
International Journal of Chemical Engineering
Volume 2021, Article ID 5536221, 10 pages
https://doi.org/10.1155/2021/5536221

Research Article

Management of Cattle Dung and Novel Bioelectricity Generation Using Microbial Fuel Cells: An Ingenious Experimental Approach

Gagandeep Kaur,[1] Yadwinder Singh Brar,[1] Jaspreet Kaur,[2] Akhil Gupta,[1] Kamal Kant Sharma,[3] Jasgurpreet Singh Chohan,[4] Raman Kumar,[4] Shubham Sharma,[5] Somnath Chattopadhyaya,[6] Shashi Prakash Dwivedi,[7] Alibek Issakhov,[8] and Nima Khalilpoor[9]

[1]*Electrical Engineering Department, I. K. Gujral Punjab Technical University Jalandhar, Kapurthala 144603, Punjab, India*
[2]*Electronics and Communication Engineering Department, Beant College of Engineering & Technology, Gurdaspur, Punjab, India*
[3]*Electrical Engineering Department, Chandigarh University, Mohali 140413, Punjab, India*
[4]*Department of Mechanical Engineering, Chandigarh University, Gharuan, Mohali, Punjab 140413, India*
[5]*Department of Mechanical Engineering, I. K. Gujral Punjab Technical University, Main Campus-Kapurthala, Jalandhar, Punjab 144603, India*
[6]*Department of Mechanical Engineering, Indian Institute Technology (Indian School of Mines), Dhanbad, Jharkhand, India*
[7]*G. L. Bajaj Institute of Technology & Management, Greater Noida, Gautam Buddha Nagar, U. P. 201310, India*
[8]*Faculty of Mechanics and Mathematics, Department of Mathematical and Computer Modelling, Al-Farabi Kazakh National University, Almaty, Kazakhstan*
[9]*Department of Energy Engineering, Graduate School of the Environment and Energy, Science and Research Branch, Islamic Azad University, Tehran, Iran*

Correspondence should be addressed to Nima Khalilpoor; nimakhalilpoor@gmail.com

Received 11 February 2021; Revised 21 March 2021; Accepted 8 October 2021; Published 31 October 2021

Academic Editor: Sébastien Déon

Microbial fuel cells (MFCs) are the rising modern equipment for the generation of bioelectricity from organic matters. In this study, MFCs in two formats are assembled and concurrently operated for a 30-day period in a batch mode manner. Natural biowaste cattle dung slurry with mediators is used as a substrate persistently for the enhancement of electron transfer rate and additionally for the augmentation of required electrical parameters. Under similar conditions, the MFC setups are experimented with a variety of anode-cathode material combinations, namely carbon-carbon, copper-carbon, and zinc-carbon. The performance of these MFCs during the testing period is evaluated independently and compared by plotting polarization data generated by them. It is revealed that maximum current and power densities are achieved from all these MFCs and the best attained values are 1858 mA/m^2 and 1465 mW/m^2, respectively, for the novel single-chamber zinc-carbon electrode MFC. The corresponding findings present that the MFC with zinc-carbon electrodes has the better power density than other MFCs. Being conductive and higher standard potential metal electrodes have improved the capability to act in place of carbon family electrodes for MFC-based power applications. Although the MFC power generation is low, but modifications in configurations, electrodes, microbe-rich biowaste, mediators, and power management may enhance the power output to a significant level for commercialization of this technology. The unique feature of this research is to explore the pertinent use of conductive metal electrodes to enhance the power generation capability of MFCs through biowaste as an alternative power source for small applications. The novelty of this research is presented through usage of conductive metal electrodes for the performance analysis of MFCs.

1. Introduction

Globally, the consumption of energy has augmented exponentially during the first decade of the 21st century and is continuing to do so. The dire need of the present scenario is to meet the ever-increasing energy demand and identify more and all feasible sources of energy. Nonrenewable sources are presently the most conspicuous means for catering to the world's energy consumption pattern in which the key role is played by fossil fuels [1]. It is common knowledge that fossil fuels are likely to be exhausted and indiscriminate exploitation of fossil fuels have posed a threat to the biological life on the planet via their secondary effects such as global warming and environmental pollution [2]. The need for alternatives to fossil fuels have encouraged researchers to seek alternative sources for power, which can be harnessed by utilizing modern tools of technology developed in recent years and in a better manner than in the past [3, 4]. As a consequence of these efforts, one of the recently proposed alternatives is energy derived from fuel cells utilizing presently wasted biomasses. A fuel cell is an electrochemical engine that converts the existing energy of chemical bonds into electricity [5]. Being a green source of energy, this option seems attractive as the energy obtained thereof is both renewable and environmentally friendly. Fuel cells utilizing biological material are biological fuel cells, capable of directly transforming chemical energy to electrical energy by the way of electrochemical reactions [6]. Biological fuel cells are classified in two types: MFCs and EFCs. If biological fuel cells are using biomass to act as a biocatalyst for bioelectricity production, then it may be named as biomass cells.

MFCs are devices that use bacterial community as the catalyst for oxidation of organic or inorganic matters, thus leading to generate current [7]. The MFC unit has an anodic and a cathodic chamber, and the two are separated by a semipermeable membrane known as PEM. In the anodic chamber, the microflora results in generation of protons and electrons via oxidation of organic matter in an anaerobic environment, generating carbon dioxide and other compounds as final products. The movement of electrons generated in the process is facilitated via an external circuit, whereby protons are transmitted to the cathodic chamber via PEM. In the cathode chamber, protons and electrons react along with parallel reduction of oxygen to water. A biopotential developed between the bacterial metabolic and these conditions led to generate bioelectricity in MFCs [1]. Anaerobic conditions are necessary in the anodic chamber as oxygen will hamper electricity production, consequently a pragmatic arrangement have to assemble for bacterial separation from oxygen [1, 6–8]. The chemical reactions taking place in the anode and cathode chambers with organic matter substrates and water are as follows:

$$C_6H_{12}O_6 + 6H_2O = 6CO_2 + 24H + 24e^- \text{ (anode chamber)}$$
$$24e^- + 24H + 6O_2 = 12H_2O \text{ (cathode chamber)}$$
$$C_6H_{12}O_6 + 6H_2O + 6O_2 = 6CO_2 + 12H_2O \text{ (MFC reaction)}$$

MFC performance mainly depends on several important factors such as system configuration, nature of organic matter, bacterial species, electrode material and surface area, type of catholyte, operating conditions, rate of oxidation in the anodic chamber, electron shuttle from the anodic chamber to surface of anode, way of supply and amount of consumption, and permeability of PEM [1, 9]. An MFC is an incredible technology with the capability to use a wide range of substrates, configurations, and materials with bacteria to get bioelectricity generation despite the fact that power levels are low. This is a preferred method for longer sustainable power applications. The glimpse of pros and cons of MFCs is shown in Table 1 and is an indicative of motivation for research.

Recent literature reviews evidence that power generation from microalgae biomass using MFCs is a recent significant way to enhancing its efficiency and achieving large-scale applications. The mixed microalgae in the single chamber with normal carbon electrodes achieved the maximum power of 76 mW/m^2, and again with mixed microalgae in a single chamber with gold-graphite electrodes achieved the maximum power density of 10 W/m^2 [10]. A comprehensive review on MFCs and plant MFCs being renewable energy sources has presented that it has been developed for many applications such as waste water treatment, biosensors, biofuels, and contaminated sediments [11]. An overview on the development and modification of anode materials for MFCs presents that MFCs follow the electrochemical approach for natural conversion of organic waste to energy. The conductivity, surface area, porosity, biocompatibility, stability, availability, and cost of material are prime factors for selection of anodes. Except carbon anodes, metal or metal-oxide anodes such as zinc, nickel, copper, gold, and iron, are also making a place for energy generation [12]. A comprehensive review on the MFC technology presented various processes, utilization, and recent developments in usage of various carbon electrodes with different substrates and bacterial species [13]. The bioelectricity generation from different biomass feed with analysis of vital parameters presented the experimental results that showed the presence of percentage organic matter in cow dung along with drain water was 0.85 and same generated 230 mV of voltage [14]. This has demonstrated the scope for bioremediation and manufacturing of anionic and polymeric bioemulsifiers with promising dispersing characteristics. A new biomolecule was utilized and prepared from UCP 1601 with emulsifying behaviour [15]. Another study [16] reported the use of pomegranate peel that acts as bioadsorbents for wastewater treatment. The potential of agriculture biomass for adsorption properties has been verified and approved by various studies. Similarly, an investigation for the treatment of synthetic textile using anaerobic and combined anaerobic-aerobic reactor systems has been carried out. Removal of toxic matter with minimal environmental degradation has been demonstrated [17].

Mostly, a review of advanced research referred in [10–17] indicates a research gap that no comprehensive performance analysis of MFCs with cattle dung as a substrate for a wide range management of cattle waste and the effect of different

Table 1: Pros and cons of MFCs.

Pros	Cons
Direct generation of power	Low power output
Sustainable alternate source of energy	Slow rate of growth of microbial population
Environment friendly	Toxicity of material
Effective conversion of energy	High material cost
Low cost for small applications	High cost for large-scale applications
Possibility of several MFC designs	High internal resistance

electrodes like popularly used carbon and novel metals on the performance of MFCs have been done. In addition, the scientometric analysis has been conducted based on keywords generated through the Scopus database. Thus, the studies conducted related to MFCs and bioelectricity in past research have raised many issues related to the performance of MFCs, and this present study tries to contribute through this paper. Figure 1 shows the scientometric chart generated through the VOSviewer analytical tool, which indicates that limited research has been carried out on manures acquired from animal waste. This analysis indicates that cattle dung must be considered for energy generation through MFCs.

Thus, the present study purposefully aims to investigate the performance parameters of cattle dung-based MFCs with carbon and metal electrodes. The aim behind this study has opened up the way for novelty of this research as an experimental work for the performance analysis of technical parameters of cattle dung-based MFCs in different designs with commonly used carbon and metal electrodes.

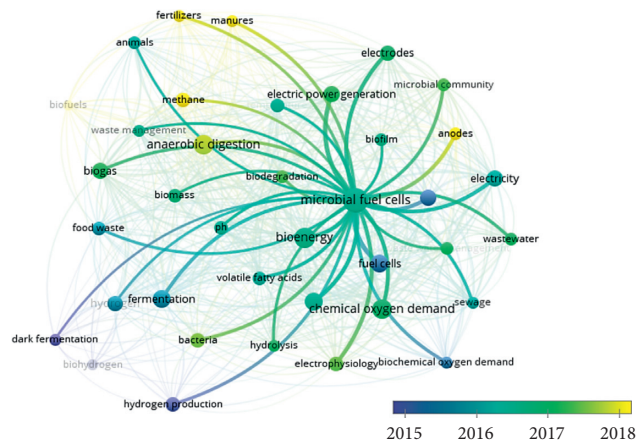

Figure 1: Scientometric chart analysis.

2. Materials and Methods

2.1. Material for MFC Assemblies. The different types, sizes, and structures of anode and cathode materials for MFC assemblies have been used by researchers to maximize the power generation and columbic efficiencies of MFCs [18–23]. In this research, for MFC assemblies, materials for anode electrodes with surface areas of 42.4 cm^2 are carbon, copper, and zinc and for cathode electrodes only carbon is used. Before using for assemblies, the electrodes are washed with 1% $HgCl_2$ and stored in 0.1 M HCl and soaked in deionized water for a period of 24 hours. For physical separation of anode and cathode chambers in MFC designs, the separator materials are classified in terms of their qualities of filtration as resulting ion-exchange membranes, salt bridge, and size selective separators [7, 24]. The lab-grade chemicals/materials as PEM are used for assemblies and supplied by Merck. The popularly used DuPont USA Nafion (117) membrane is used as per the size of MFC reactor. The substrates for these assemblies are cattle dung available in abundant as waste, rich in microorganism and nutrients. The substrate is prepared in the lab by adding distilled water to fresh cattle dung, making it as slurry in a ratio of 1 : 4 to act as the anolyte without any pretreatment and distilled water or natural air as the catholyte to make O_2 as an electron acceptor. Quantitative analysis evidences that different quantities of cellulose, hemicelluloses, and lignin are found in dung with a small number of other extractives [6, 25]. Fibre content of lignocellulose dung, such as cellulose, hemicellulose, and lignin, has been found by the analysis of ADF, NDF, and ADL using the reflux apparatus and by following standard method of testing. Total lignocellulose material has been estimated by NDF and ADF is used to estimate the content of lignin and cellulose, which are the prime criteria for energy conversion technique. In the present work, the random samples of fresh cattle dung are collected by trained persons from local dairy farms of one region, Punjab, by following the standard method of sample collection and tested at SSNIBE, Punjab, and the results of fibre analysis are presented in Table 2.

2.2. Microbial Community Analysis. Cattle dung is an ideal candidate as energy a feedstock because of easily degradable high organic matter. Since long, manure has been extensively appreciated as a fertilizer but harmful due to considerable water and air pollution. Cattle dung is an alternative option for generation of electricity through MFCs and simultaneously maintains fertilizer value. This study explores the treatment of dung in terms of examining the presence of microbial species to activate the generation of bioelectricity process in MFCs. It is well known that microorganisms such as *Bacillus* and *Pseudomonas* act as electrifying bacteria in organic matters, which further help in microbial degradation of pollutants [26]. The results of microbial analysis are presented in Table 3. Furthermore, the scientometric analysis has been performed to highlight the use of manure as a fertilizer and energy source in India. Figure 2 shows the keyword relationship between cattle dung and its implementation as a manure and fertilizer for

Table 2: Fibre analysis of fresh cattle dung.

Lignocellulose (%)	24
Hemicellulose (%)	14
Lignin (%)	04
Extractives/volatiles (%)	44
Ash (%)	14
Lignin-to-cellulose ratio	0.167

agriculture purpose. In India, cattle dung is considered an excellent alternative to chemical-based fertilizers as India is a country with large rural population. The presence of chemicals such as phosphorus, carbon, and other minerals improves the fertility of soil with minimum cost. The chart in Figure 2(b) depicts the utilization of cattle dung as an energy source, which is highlighted as reported in recent studies. In rural areas, cattle dung is still used as an energy source due to its availability in abundance. Biogas plants are installed to extract biogas, which is used for cooking and industrial applications.

2.3. MFC Configurations. An inexpensive and widely used configuration is the H-shaped double-chamber MFC consisting of two chambers separated by a membrane or salt bridge. These H-shaped chambers are acceptable for examining power production with different materials, microbes, mediators, etc. However, the produced power density is limited by high internal resistance and subsequent scaling is cumbersome in such configurations [7]. Power density and system internal resistance are the key characteristics dependent on properties such as the surface area of the cathode, anode, or separator and distance kept between electrodes [27]. To conquer this complexity, a virtual alternative that offers cost and operational saving is a single-chamber MFC [6, 12]. In the single chamber, the anode electrode is kept in anaerobic conditions in an anodic compartment and the cathode electrode is exposed to air called single-chamber air cathode MFC. Higher currents and voltages can be attained by series and parallel stacking of MFCs [6, 8, 9, 16]. However, the key issue is the long-term impact of voltage reversal in stacked MFCs, which need further research for improved voltage production [9]. In this study, novel single-chamber MFC assemblies are fabricated and examined with standard test procedures for feasibility of MFCs as a power source. DCMFC assemblies are experimented with formation of three individual cells: DCMFC1, DCMFC2, and DCMFC3. In these double-chamber MFCs, the common materials used are two plastic containers as the anode and cathode chamber, Nafion membrane of suitable dimensions, and cattle dug slurry of 700 ml in the anode chamber and 700 ml distilled water in the cathode chamber with potassium permanganate of 300 μmol/l as the mediator in the cathode chamber. Carbon-carbon electrodes in DCMFC1, copper-carbon electrodes in DCMFC2, and zinc-carbon electrodes in DCMFC3, all are of same area and shape, act as anode and cathode electrodes, respectively, and the basic design prepared and implemented in this study is shown in Figure 3(a). To analyze the performance of SCMFCs, SCMFC assemblies named as SCMFC4, SCMFC5, and SCMFC6 are experimented with formation of three independent cells. Each SCMFC consists of a single chamber containing an anode electrode without any aerated cathode chamber. The anode compartment of the plastic container is loaded with dung slurry of 700 ml with methylene blue of 300 μmol/l as the mediator coupled to the porous cathode exposed directly to air. The anode compartment and cathode are provided with sample port, wire point inputs, and ports for electrode wires. The cathode electrode is pasted through Nafion membrane of suitable dimensions with a 20–30% of electrode area is embedded in the membrane and the rest is exposed to air outside of the anode compartment. Carbon-carbon electrodes in SCMFC4, copper-carbon electrodes in SCMFC5, and zinc-carbon electrodes in SCMFC6, all are of same area, are used as anode and cathode electrodes, respectively. The basic schematic of SCMFC assembly designed and implemented in this study is shown in Figure 3(b). The six experimental setups of DCMFC and SCMFC are operated continuously in batch mode for a period of 30 days under ambient conditions.

Table 3: Isolated microbial analysis.

Isolate	Identified bacteria
B1	*Bacillus subtilis*
B2	*Escherichia coli*
B3	*Streptococcus species*
B4	*Pseudomonas aeruginosa*
B5	*Clostridium species*
B6	*Peptostreptococcus species*
B7	*Bacillus cereus*
B8	*Klebsiella species*
B9	*Bacteroides species*

2.4. Calculation of Electrical Parameters. The maximum voltage theoretically attained by MFCs with organic substrate and carbon family electrodes is of the order of 1.1 V. The oxygen reduction reaction at the cathode does not provide the theoretical potential of +0.84 V because of the impact of activation losses on potential. Moreover, the ohmic and activation losses are more dominant as resistances are lowered and current increases. Due to these losses, the measured MFC voltage is considerably lower. These voltages are recorded using a multimeter. The commonly achieved maximum working voltage for MFCs is 0.3–0.7 V. The peak voltage attained in MFCs is always the OCV. Current and power are calculated as per standards followed by research works. Primary parameters like "current" and "power density" were calculated by dividing current and power, respectively, by the projected surface area of electrodes. Polarization data are obtained by changing external resistances from 25 Ω to 1000 Ω [7, 8, 27–29].

3. Results and Discussion

3.1. Characterization of Cattle Dung. For the utilization of cattle dung as a substrate, the characterization of dung has been done by fibre analysis and microbial analysis. The

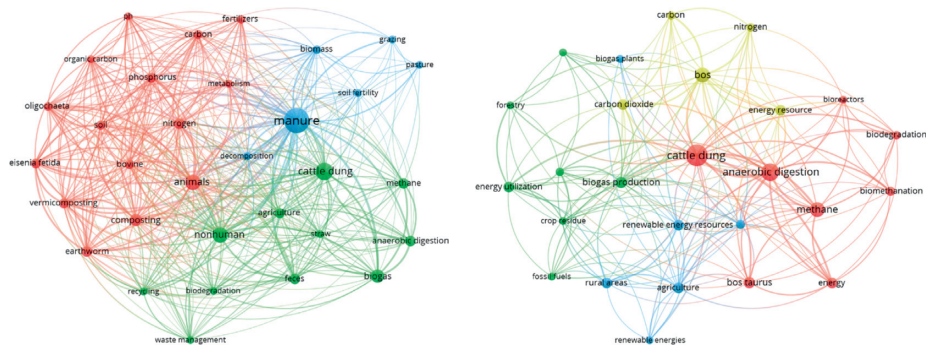

(a) (b)

Figure 2: Scientometric analysis of utilization of cattle dung as (a) manure and (b) energy source.

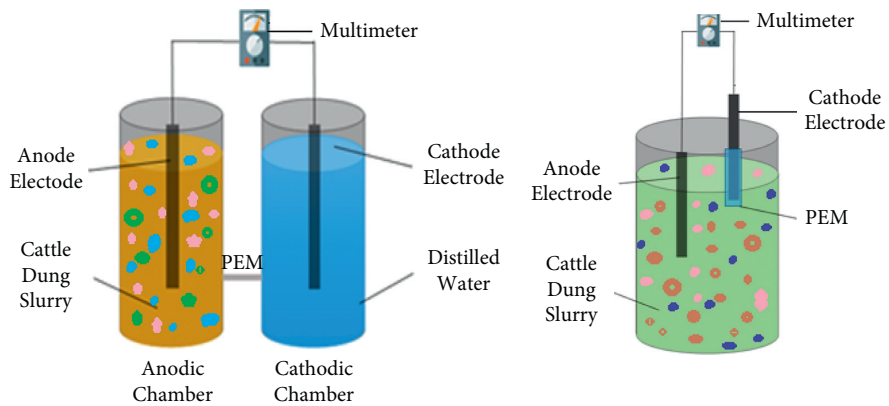

(a) (b)

Figure 3: (a) Double-chamber MFC. (b) Single-chamber MFC.

results of fibre and microbial analyses are presented in Tables 2 and 3, respectively.

The results of fibre analysis in Table 2 reveal the lignin-to-cellulose ratio along with other polymers, namely cellulose, hemicelluloses, lignin, extractives or volatiles, and ash content. Higher cellulose represents good potential for biomethanation. Cattle dung has a medium range of (24%) cellulose and moderately good for the process. Hemicellulose of 14% for dung is most appropriate for anaerobic digestion (AD). Higher the lignin content lower is the digestibility as it is difficult to degrade in anaerobic conditions. Cattle dung has (4%), very less value of lignin and suitable for the AD process. In case of lignocellulose biomass, the lignin-to-cellulose ratio is normally used to define the degree of digestibility of biomass. The lignin-to-cellulose ratio for dung was 0.167 with extractives of 44% and ash 14%. All above results for the characterization of biomass are comparable with the results of [9, 21, 30, 31]. The results conclude that dung has immense properties to act as a sustainable renewable energy source for electrical power generation.

Similarly, the microbial population of specific species is necessary for decomposition of organic matters, which further activates the electron flow process and generation of bioelectricity. Bacterial isolates are classified on the basis of their features in different forms of species. The isolation and identification of bacterial count are the most important steps for dung analysis. Isolation of microbes in dung has shown the prominent presence of nine bacterial species (Table 3), which play a vital role in the anaerobic process and also have been previously shown by researchers [10, 32, 33]. To enhance the power generating capabilities of MFCs, identification of power-developing bacteria is mandatory. Identification and viable count always helped in addition of particular types of bacteria as mediators for the augmentation of power density.

3.2. Performance of Double-Chamber MFCs. DCMFCs are continuously operated in batch mode for a period of 30 days, and the OCV of all cells are measured daily and the maximum achieved voltages are shown in Table 4. This relatively high voltage can be attributed to a high standard electrode potential and conductivity of the anode electrode with the same substrate for each cell [34–41]. With the stabilization of cells' output voltages, the performance of each cell is evaluated at a ten-day interval by plotting polarization curves. The polarization curves are plotted in Figure 4 after making measurements by utilizing multiple external resistances with values ranging from OCV, 1000 Ω, 500 Ω, 250 Ω, 100 Ω, 50 Ω, to 25 Ω. The voltages across

Table 4: Electrical parameters of DCMFCs and SCMFCs.

Cell number	DCMFC1	DCMFC2	DCMFC3	SCMFC4	SCMFC5	SCMFC6
OCV (mV)	946	915	1184	1098	1078	1292
Current (mA)	4.73	4.58	5.68	6.81	6.68	7.88
Current density (mA/m^2)	1116	1080	1340	1606	1575	1858
Power (mW)	2.24	2.10	3.23	4.64	4.46	6.21
Power density (mW/m^2)	528	495	762	1094	1052	1465

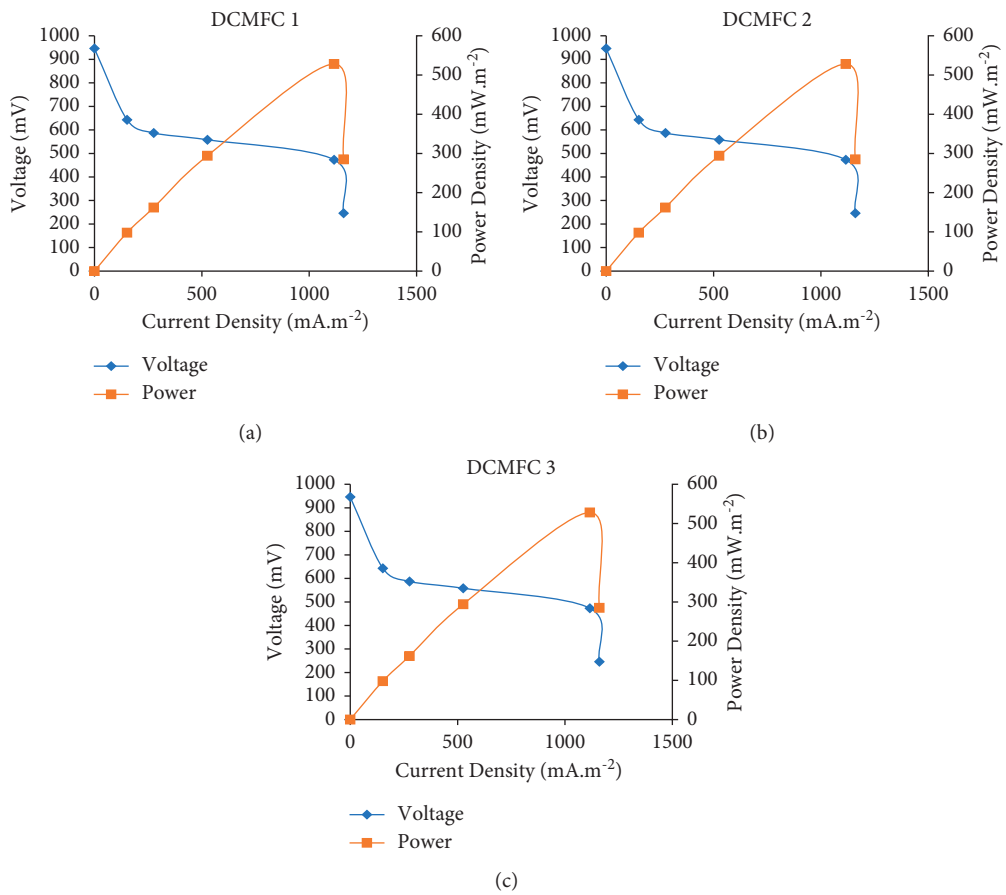

Figure 4: Polarization curves of (a) DCMFC1, (b) DCMFC2, and (c) DCMFC3.

these resistors are recorded every 3 hours in order to allow the bacterial cultures to produce sufficient current at lower voltages, which in addition provide enough time for biofilm to adapt changes in resistances. The polarization curves of cells evidence that the voltage drop is 50% as current increased to 4.73 mA at 100 Ω in order to maximize power production in case of DCMFC1. Similarly, in DCMFC2, the drop in voltage is 49% as current increased to 4.58 mA at 100 Ω, and in DCMFC3, the drop in voltage is 48% as current increased to 5.68 mA at 100 Ω. The maximum generated power densities and current densities for cells DCMFC1, DCMFC2, and DCMFC3 are 528 mW/m^2 and 1116 mA/m^2, 495 mW/m^2 and 1080 mA/m^2, and 762 mW/m^2 and 1340 mA/m^2, respectively, and are shown in Table 4.

3.3. Performance of Single-Chamber MFCs. The performance of SCMFCs differs considerably from DCMFCs due to the different MFC reactor design. The experimental conditions and materials used for SCMFCs are similar to DCMFCs, such as electrode material, substrates, and membranes [42–45]. Like DCMFCs, SCMFCs are continuously operated for 30 days in batch mode. The maximum OCV achieved in all three SCMFCs is shown in Table 4. The performance of these cells is also evaluated by the polarization curves as shown in Figure 5 at maximum voltages using adjustable external resistances of the same range as in DCMFCs to determine current and power densities. The maximum generated power and current densities for cells SCMFC4, SCMFC5, and SCMFC6 are 1094 mW/m^2 and 1606 mA/m^2, 1052 mW/m^2 and 1575 mA/m^2, and 1465 mW/m^2 and

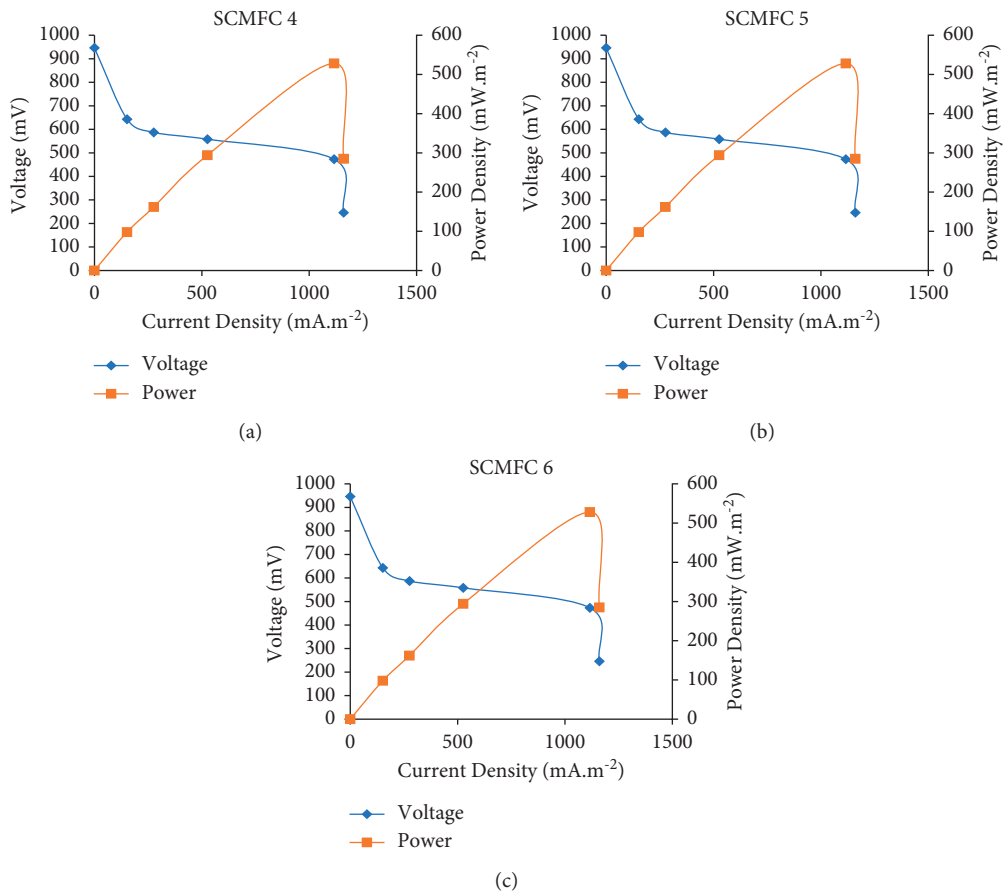

Figure 5: Polarization curves of (a) SCMFC4, (b) SCMFC5, and (c) SCMFC6.

1858 mA/m^2, respectively. Performance parameters of other electrical quantities are similarly recorded and presented in Table 4.

The comparison of power densities and current densities of DCMFCs and SCMFCs operated in this study have shown that SCMFC6 performed best among all cells with the maximum power density of 1465 mW/m^2 and current density of 1858 mA/m^2. Results in references [7, 32] have amply defended those performances of MFCs and cannot be compared with our results because of simultaneous variations of so many parameters such as configuration, electrode type, surface area, substrate, electron transfer, microbial population, atmospheric conditions, and anaerobic conditions. Though there are few research works on biomass wastes-based MFCs with carbon and metal electrodes, their findings are compared with this study results and presented in Table 5.

Broadly, the results of present study are much better than those of others in terms of power densities, but this approximate comparative chart has neglected many significant factors such as electron transfer rate, microbial population, and size and shape of electrodes. Results of the studies indicate that cattle dung when used as a substrate in an MFC results in a full-grown and well-formed biofilm due to microbial action, which is the primary parameter for consistent electrical performance. The higher power and current densities of metal electrode MFCs can perform better in rich organic matters.

4. Challenges in Implementation of MFC Technology

There are immense challenges in implementation of this technology, and multiple issues have been faced by many researchers who worked on various configurations, but till date no configuration has been commercialized. MFC performance especially power and energy output are not only dependent on technical parameters rather it mainly associates with the process of biochemical conversion. Low power density and low current are the major barriers in commercialization of this technology. Cells polarity, voltage overshoots, and voltage reversals are the main issues of low MFC performance. Measurement of such low values requires lots of precision and accuracy of high technology instruments. There are also technical hitches in comparing the MFC performances on corresponding basis. As an agricultural country like India, it is indeed challenging to use such technology since organic matter seems abundant; however, contamination of organic matter is widespread ubiquitous.

Table 5: Comparison analysis of various studies.

Substrate	Anode	Cathode	Power density	References
Glucose with *Pseudomonas aeruginosa* bacteria	Carbon/graphite	Carbon/graphite	$2096.5 \pm 11.8\,\mu W/m^2$	[34]
Glucose with *Escherichia coli*	Carbon/graphite	Carbon/graphite	$1606\,mW/m^2$	[35]
Glucose with *Escherichia coli*	Carbon/graphite	Carbon/graphite	$2420\,mW/m^2$	[36]
Algae strain	Carbon	Copper sheet	$19151\,mW/m^2$	[37]
—	Alumina and nickel nanoparticles	Polymer alumina and nickel nanoparticles	$1270 + 30\,mW/m^2$	[38]
Biowaste from environment	Carbon/graphite	Carbon/graphite	$396.7\,mW/m^2$	[39]
Livestock waste	Carbon/graphite	Carbon/graphite	$122\,mW/m^2$	[40]
Mixed microalgae	Carbon	Carbon	$76\,mW/m^2$	[10]
Mixed microalgae	Gold	Graphite	$10\,W/m^2$	[10]
Cattle dung with B1–B9 bacteria	Zinc	Carbon	$1465\,mW/m^2$	Present study

5. Conclusions

DCMFCs with conventional H-design and SCMFCs with novel designs are fabricated and operated successfully in batch mode for a period of 30 days under similar physical conditions. The objectives of these MFC assemblies are to analyze the significant electrical performance parameters as power densities and current densities using cattle dung substrate and carbon and metal electrodes. Usage of metal electrodes is rarely preferred in MFC configurations with a perception of metal corrosion and difficulty in accumulation of microbes on plane surfaces. The main findings of this study are the successful operation of metal electrode MFCs with the rough surface of novel metal electrodes for both configurations and SCMFC6 having zinc-carbon electrodes achieved the maximum power density. The maximum OCV achieved for SCMFC6 is 1292 mV, and with standard tests the maximum obtained current is 8 mA, the maximum power of 6.21 mW, and the maximum power density is$1465\,mW/m^2$ at $100\,\Omega$. The MFC is a prominent technology for bioelectricity generation and offers prospects for utilization of various organic wastes with novel metal electrodes. This study has more scope for further research as this technology is still at the laboratory level and needs bundles of diverse approaches before commercialization. A number of organic wastes, carbon family materials, and especially metals are open for research to enhance the power outputs of cells. New designs of cells, simulation and modelling of cells, and quality of power can be the advance areas of research. Handling of trouble shootings for MFC assembly and operation are the thrust areas, which require comprehensive research.

Abbreviations

MFC: Microbial fuel cell
EFCs: Enzymatic fuel cells
PEM: Proton-exchange membrane
$HgCl_2$: Mercury chloride
HCl: Hydrogen chloride
ADF: Acid detergent fibre
NDF: Neutral detergent fibre
ADL: Acid detergent lignin
O_2: Dioxygen
DCMFC: Double-chamber MFC
SCMFC: Single-chamber MFC
OCV: Open circuit voltage.

Data Availability

The data presented in this study are available on request from the corresponding author.

Additional Points

(i) (ii) Management of waste cattle dung through bioelectricity generation has been demonstrated. Bioelectricity generation using carbon and metal electrodes in MFC is highlighted

(iii) Polarization data have been plotted for testing the performance of cells independently

(iv) Achievement of high current and power densities with single-chamber MFC has been reported

Conflicts of Interest

The authors declare that there are no conflicts of interest with anyone.

Authors' Contributions

Conceptualization of the study was developed by Gagandeep Kaur, Yadwinder Singh Brar, and Raman Kumar. Methodology of the study was designed by Jaspreet Kaur, Akhil Gupta, and Shubham Sharma. Study investigations were carried out by Gagandeep Kaur, Kamal Kant Sharma, Jasgurpreet Singh Chohan, and Shubham Sharma. Original draft preparation was done by Gagandeep Kaur, Shubham Sharma, S Chattopadhyaya, SP Dwivedi, Alibek Issakhov, and Nima Khalilpoor.

Acknowledgments

The work is based on the doctorate thesis of the first author, who wants to affectionately express gratitude to her mentors. The authors are deeply indebted to Ms. Harbhajan Kaur and

Mr. Gobinder Singh, retired officers of PSPCL of Punjab province, India, for their invaluable contributions in the experimental work. The authors also than I. K. Gujral Punjab Technical University Jalandhar, India, for all technical and academic support.

References

[1] M. Rahimnejad, A. Adhami, S. Darvari, A. Zirepour, and S.-E. Oh, "Microbial fuel cell as new technology for bio-electricity generation: a review," *Alexandria Engineering Journal*, vol. 54, no. 3, pp. 745–756, 2015.

[2] D. Lovely, "Microbial fuel cells: novel microbial physiologies and engineering approaches," *Current Opinion in Biotechnology*, vol. 17, pp. 327–332, 2006.

[3] D. P. B. T. B. Strik, H. Terlouw, H. V. M. Hamelers, and C. J. N. Buisman, "Renewable sustainable biocatalyzed electricity production in a photosynthetic algal microbial fuel cell (PAMFC)," *Applied Microbiology and Biotechnology*, vol. 81, no. 4, pp. 659–668, 2008.

[4] A. E. Franks and K. P. Nevin, "Microbial fuel cells, a current review," *Energies*, vol. 3, no. 5, pp. 899–919, 2010.

[5] B. C. H. Steele and A. Heinzel, "Materials for fuel-cell technologies," *Nature*, vol. 414, no. 6861, pp. 345–352, 2001.

[6] G. S. Gupta, "Microbial fuel cell technology: a review on electricity generation," *Journal of Cell & Tissue Research*, vol. 11, no. 1, pp. 2631–2654, 2011.

[7] B. E. Logan, B. Hamelers, R. Rozendal et al., "Microbial fuel cells: methodology and technology," *Environmental Science & Technology*, vol. 40, no. 17, pp. 5181–5192, 2006.

[8] J. Choi and Y. Ahn, "Continuous electricity generation in stacked air cathode microbial fuel cell treating domestic wastewater," *Journal of Environmental Management*, vol. 130, pp. 146–152, 2013.

[9] M. Rahimnejad, A. A. Ghoreyshi, G. D. Najafpour, H. Younesi, and M. Shakeri, "A novel microbial fuel cell stack for continuous production of clean energy," *International Journal of Hydrogen Energy*, vol. 37, no. 7, pp. 5992–6000, 2012.

[10] M. E. Elshobary, H. M. Zabed, J. Yun, G. Zhang, and X. Qi, "Recent insights into microalgae-assisted microbial fuel cells for generating sustainable bioelectricity," *International Journal of Hydrogen Energy*, vol. 46, no. 4, pp. 3135–3159, 2021.

[11] W. Apollon, A. Isabel luna, S. Kumar Kamaraj et al., "Progress and recent trends in photosynthetic assisted microbial fuel cells: a review," *Biomass and Bioenergy*, vol. 148, pp. 1–14, Article ID 10828, 2021.

[12] A. A. Yaqoob, M. N. M. Ibrahim, and S. R. Couto, "Development and modification of materials to build cost-effective anodes for microbial fuel cells (MFCs): an overview," *Biochemical Engineering Journal*, vol. 164, pp. 1–14, Article ID 10779, 2020.

[13] G. Palanisamy, H.-Y. Jung, T. Sadhasivam, M. D. Kurkuri, S. C. Kim, and S.-H. Roh, "A comprehensive review on microbial fuel cell technologies: processes, utilization, and advanced developments in electrodes and membranes," *Journal of Cleaner Production*, vol. 221, pp. 598–621, 2019.

[14] G. harshita, A. sahoo, and R. Sethy, "Bioelectricity generation from different biomass feed at anode chamber and to study process parameters in microbial fuel cells," *Biocatalysis and Agricultural Biotechnology*, vol. 20, pp. 1–4, Article ID 101191, 2019.

[15] I. B. Nogueira, D. Montero Rodríguez, and F. Rosildeide, "Bioconversion of agroindustrial waste in the production of bioemulsifier by Stenotrophomonas maltophilia UCP 1601 and application in bioremediation process," *International Journal of Chemical Engineering*, vol. 2020, Article ID 9434059, 9 pages, 2020.

[16] S. Ben-Ali, "Application of raw and modified pomegranate peel for wastewater treatment: a literature overview and analysis," *International Journal of Chemical Engineering*, vol. 2021, Article ID 8840907, 19 pages, 2021.

[17] T. M. Kathawala, K. V. Gayathri, and P. Senthil Kumar, "A performance comparison of anaerobic and an integrated anaerobic-aerobic biological reactor system for the effective treatment of textile wastewater," *International Journal of Chemical Engineering*, vol. 2021, Article ID 8894332, 15 pages, 2021.

[18] U. Schröder, "Anodic electron transfer mechanisms in microbial fuel cells and their energy efficiency," *Physical Chemistry Chemical Physics*, vol. 9, no. 21, pp. 2619–2629, 2007.

[19] P. Aelterman, K. Rabaey, H. T. Pham, N. Boon, and W. Verstraete, "Continuous electricity generation at high voltages and currents using stacked microbial fuel cells," *Environmental Science & Technology*, vol. 40, no. 10, pp. 3388–3394, 2006.

[20] F. J. Hernández-Fernández, A. Pérez de los Ríos, M. J. Salar-García et al., "Recent progress and perspectives in microbial fuel cells for bioenergy generation and wastewater treatment," *Fuel Processing Technology*, vol. 138, pp. 284–297, 2015.

[21] A. D. Tharali, N. Sain, and W. J. Osborne, "Microbial fuel cells in bioelectricity production," *Frontiers in Life Science*, vol. 9, no. 4, pp. 252–266, 2016.

[22] A. Baudler, I. Schmidt, M. Langner, A. grenier, and U. Schroder, "Does it have to be carbon? Metal anodes in microbial fuel cells and related bio-electrochemical systems," *Energy and Environmental Science*, vol. 8, p. 2039, 2015.

[23] N. Haque, D. Cho, and S. Kwon, "Characteristics of electricity production by metallic and nonmetallic anodes immersed in mud sediment using sediment microbial fuel cell," *IOP Conference Series: Materials Science and Engineering*, vol. 88, 2015 7th International Conference on Cooling & Heating Technologies (ICCHT 2014), Article ID 012072.

[24] W.-W. Li, G.-P. Sheng, X.-W. Liu, and H.-Q. Yu, "Recent advances in the separators for microbial fuel cells," *Bioresource Technology*, vol. 102, no. 1, pp. 244–252, 2011.

[25] P. Mckendry, "Energy production from biomass (part 1): overview of biomass," *Bioresource Technology*, vol. 83, no. 1, pp. 37–46, 2002.

[26] G. Zhao, F. Ma, L. Wei, H. Chua, C.-C. Chang, and X.-J. Zhang, "Electricity generation from cattle dung using microbial fuel cell technology during anaerobic acidogenesis and the development of microbial populations," *Waste Management*, vol. 32, no. 9, pp. 1651–1658, 2012.

[27] A. N. Ghadge and M. M. Ghangrekar, "Performance of low cost scalable air-cathode microbial fuel cell made from clayware separator using multiple electrodes," *Bioresource Technology*, vol. 182, pp. 373–377, 2015.

[28] J. Winfield, L. D. Chambers, J. Rossiter, J. Greenman, and I. Ieropoulos, "Towards disposable microbial fuel cells: natural rubber glove membranes," *International Journal of Hydrogen Energy*, vol. 39, no. 36, pp. 21803–21810, 2014.

[29] V. J. Watson and B. E. Logan, "Analysis of polarization methods for elimination of power overshoot in microbial fuel cells," *Electrochemistry Communications*, vol. 13, no. 1, pp. 54–56, 2011.

[30] P. C. Roy, A. Datta, and N. Chakraborty, "Assessment of cow dung as a supplementary fuel in a downdraft biomass gasifier," *Renewable Energy*, vol. 35, no. 2, pp. 379–386, 2010.

[31] K. Inoue, T. Ito, Y. Kawano et al., "Electricity generation from cattle manure slurry by cassette-electrode microbial fuel cells," *Journal of Bioscience and Bioengineering*, vol. 116, no. 5, pp. 610–615, 2013.

[32] K. Rabaey, S. T. Read, P. Clauwaert et al., "Cathodic oxygen reduction catalyzed by bacteria in microbial fuel cells," *The ISME Journal*, vol. 2, no. 5, pp. 519–527, 2008.

[33] Y. Zuo, D. Xing, J. M. Rehan, and B. E. Logan, "Isolation of the exoelectrogenic bacterium Ochrobactrum anthropi YZ-1 by using a U-tube microbial fuel cell," *Applied and Environmental Microbiology*, vol. 74, pp. 3130–3137.

[34] J. Jayapriya and V. Ramamurthy, "Use of non-native phenazines to improve the performance of Pseudomonas aeruginosa MTCC 2474 catalysed fuel cells," *Bioresource Technology*, vol. 124, pp. 23–28, 2012.

[35] X. Chen, D. Cui, X. Wang, X. Wang, and W. Li, "Porous carbon with defined pore size as anode of microbial fuel cell," *Biosensors and Bioelectronics*, vol. 69, pp. 135–41, 2015.

[36] Y. Tao, Q. Liu, J. Chen et al., "Hierarchically three-dimensional nanofiber based textile with high conductivity and biocompatibility as a microbial fuel cell anode," *Environmental Science and Technology*, vol. 50, no. 95, p. 7889, 2016.

[37] Q. Hou, H. Pei, W. Hu, L. Jiang, and Z. Yu, "Mutual facilitations of food waste treatment, microbial fuel cell bioelectricity generation and Chlorella vulgaris lipid production," *Bioresource Technology*, vol. 203, pp. 50–55, 2016.

[38] S. Singh, A. Modi, and N. Verma, "Enhanced power generation using a novel polymer-coated nanoparticles dispersed-carbon micro-nanofibers-based aircathode in a membraneless single chamber microbial fuel cell," *International Journal of Hydrogen Energy*, vol. 41, pp. 1237–1247, 2016.

[39] M. Sindhuja, S. Harinipriya, A. C. Bala, and A. K. Ray, "Environmentally available biowastes as substrate in microbial fuel cell for efficient chromium reduction," *Journal of Hazardous Materials*, vol. 355, pp. 197–205, 2018.

[40] M. F. Lai, C. W. Lou, and J. H. Lin, "Improve 3D electrode materials performance on electricity generation from livestock wastewater in microbial fuel cell," *International Journal of Hydrogen Energy*, vol. 43, pp. 11520–11529, 2018.

[41] M. A. Jokar, M. H. Ahmadi, M. Sharifpur, J. P. Meyer, F. Pourfayaz, and T. Ming, "Thermodynamic evaluation and multi-objective optimization of molten carbonate fuel cell-supercritical CO 2 Brayton cycle hybrid system," *Energy Conversion and Management*, vol. 153, pp. 538–556, 2017.

[42] A. Khatibi, F. Razi Astaraei, and M. H. Ahmadi, "Generation and combination of the solar cells: a current model review," *Energy Science & Engineering*, vol. 7, no. 2, pp. 305–322, 2019.

[43] M. Sadeghzadeh, B. Ghorbani, M. H. Ahmadi, and S. Sharma, "A solar-driven plant to produce power, cooling, freshwater, and hot water for an industrial complex," *Energy Report*, vol. 7, pp. 5344–5358, 2021.

[44] K. K. Sharma, A. Gupta, G. Kaur et al., "Power quality and transient analysis for a utility-tied interfaced distributed hybrid wind-hydro controls renewable energy generation system using generic and multiband power system stabilizers," *Energy Report*, vol. 7, pp. 5034–5044, 2021.

[45] K. K. Sharma, A. Gupta, R. Kumar et al., "Economic evaluation of a hybrid renewable energy system (HRES) using hybrid optimization model for electric renewable (HOMER) software-a case study of rural India," *International Journal of Low-Carbon Technologies*, vol. 16, no. 3, pp. 1–8, 2021.

Hindawi
International Journal of Chemical Engineering
Volume 2021, Article ID 5539048, 9 pages
https://doi.org/10.1155/2021/5539048

Review Article

Advanced Applications of Fuel Cells during the COVID-19 Pandemic

Shammya Afroze,[1] Md Sumon Reza,[1] Quentin Cheok,[1] Shafi Noor Islam,[2] Abdalla M. Abdalla,[3] Juntakan Taweekun,[4] Abul K. Azad,[1] Nima Khalilpoor,[5] and Alibek Issakhov[6]

[1]*Faculty of Integrated Technologies, Universiti Brunei Darussalam, Jalan Tungku Link, Gadong BE1410, Brunei Darussalam*
[2]*Faculty of Arts and Social Sciences, Universiti Brunei Darussalam, Jalan Tungku Link, Gadong BE1410, Brunei Darussalam*
[3]*Mechanical Engineering Department, Faculty of Engineering, Suez Canal University, Ismailia 41522, Egypt*
[4]*Department of Mechanical Engineering, Faculty of Engineering, Prince of Songkla University, Hatyai, Songkhla 90112, Thailand*
[5]*Department of Energy Engineering, Graduate School of the Environment and Energy, Science and Research Branch, Islamic Azad University, Tehran, Iran*
[6]*Faculty of Mechanics and Mathematics, Department of Mathematical and Computer Modelling, Al-Farabi Kazakh National University, Almaty, Kazakhstan*

Correspondence should be addressed to Abul K. Azad; abul.azad@ubd.edu.bn and Nima Khalilpoor; nimakhalilpoor@gmail.com

Received 8 February 2021; Revised 10 March 2021; Accepted 1 June 2021; Published 11 June 2021

Academic Editor: Ho SoonMin

COVID-19 was identified all over the world as a pandemic in December 2019. This novel coronavirus affects the lower respiratory area, which causes pneumonia in the human body and transfers from human to human. Every day, the number of new patients and the number of deaths are increasing immensely, while specific drugs for this virus are still being developed. Hospitals are struggling to accommodate patients, resulting in a large number of temporary hospitals. These makeshift hospitals need an uninterrupted power supply to continuously maintain all the electrical facilities. Fuel cells, especially solid oxide fuel cells, play an essential role in meeting the additional energy needs of humankind during this critical moment. SOFCs are able to supply power to those makeshift hospitals from the main hospital building, as well as supplying electricity to locked-down residential areas to ease the strain on the electrical grid during this pandemic situation. As a result of their extensive applicability and numerous uses, SOFCs can be used to address electrical needs challenges in various sectors.

1. Introduction

The COVID-19 pandemic has caused the deaths of millions of people. There have been relentless undertakings in order to save lives in all parts of the world. In Wuhan, China, the first outbreak of a disease caused by Severe Acute Respiratory Syndrome Coronavirus 2 (SARS-CoV-2) was detected and later it was named "Coronavirus Disease 19 (COVID-19)" [1]. On 17 November 2019, the first patient was diagnosed with COVID-19 with an initial symptom of pneumonia in China [2], and subsequently, several patients were admitted to hospitals with initial symptoms of pneumonia in December 2019 as reported by the World Health Organization (WHO) [3]. Thereafter, the number of patients increased rapidly across China and almost among the whole world [4, 5]. On 11 March 2020, the WHO declared COVID-19 as a pandemic [6]. As of 9 March 2021 (GMT 05:58 am), 117,751,038 cases had been reported globally and the death toll was 2,612,196. In the United States, the cumulative number of COVID-19 cases rose to 29,744,652, exceeding the cases in France (3,909,560), Russia (4,333,029), the UK (4,228,998), Spain (3,160,970), Italy (3,081,368), and China (90,002) as of 9 March 2021 [7]. This new virus has since spread to more countries than the 2003

SARS-CoV [8]. Figure 1 shows the most affected nations in the world due to COVID-19.

The COVID-19 virus is a novel beta RNA coronavirus (size: 60–140 nm diameter with backbone projections) that causes respiratory syndromes. Coronavirus sufferers may additionally have a fever with severe respiratory problems and cough, and some patients had also suffered gastrointestinal complications and symptoms (diarrhoea, vomiting, and stomach pain) [9–11]. Patients who have cancer, excessive blood pressure, cardiac problems, asthma, and diabetes, as well as older people and people with digestive disorders, are at a high chance of being impacted by COVID-19 [12, 13]. With the advent of new strains, several attempts have been made to produce COVID-19 vaccines [14], but certain problems with vaccine development on a large scale in the future and long-term storage stability will arise [15]. Researchers are still trying to develop the drugs for this novel virus [16]. This virus causes severe acute respiratory symptoms that spread by human-to-human contact. Due to its nosogenic nature, self-isolation, wearing sterile face masks, and social distancing are mandatory for preventing the spread of COVID-19 [17]. Each country has introduced quarantine rules (which usually lasts 14 days) to prevent the spread of this disease as much as possible [18].

It has been discovered that the long-term air pollution found in major cities accelerates the rate of infection of COVID-19, and there is a strong correlation between the mortality rate of infected persons and the amount of air pollution [19]. During the pandemic, almost all industries were temporarily closed down, and due to stay-at-home orders by governments, there have been fewer vehicles on the road, leading to lower emissions of CO_2, NO_2, and other toxic elements. It has been found that air pollution was one of the reasons for the high mortality rate due to the coronavirus in the USA [20]. The gaseous pollutant can damage the cellular and immune system by causing respiratory stimulation, cough, throat irritation, and breathing problems to the human body [21]. It was also found that the affected and death rates for COVID-19 were higher in Northern Italy due to the higher levels of air pollution [22].

During the COVID-19 period, the number of new cases abruptly rose globally, and hospitals became incapable of admitting all of the affected patients. Therefore, governments have had to erect mobile hospitals with beds. Each bed had to contain ventilators in order to supply an adequate amount of artificial ventilation for the patient. They also need the external power supply for the ventilators, along with other electrical equipment (including air-conditioners). In addition, due to the work-from-home notices, people have to stay at home, increasing the demand for electricity. This is a critical time to prioritize the supply of electrical energy to meet this additional demand [23]. Efforts are being made to adapt to the rate at which energy demand increases every day. Sustainable renewable energy sources are needed to meet this growing energy demand, and one of the most viable sources of green energy is fuel cells for this purpose. Figure 2 depicts the solid oxide fuel cell (SOFC) power supply chain from hospitals to makeshifts.

These fuel cell technologies for the next-generation hydrogen economy can be utilized with zero combustion [25]. The choice of the fuel cell is key to a successful installation. Fuel cell applications can replace most internal combustion engines, providing static and portable power. Fuel cells are a technological advancement since the twentieth century [26]. The principles of a fuel cell were first developed in 1839 by William Grove, who researched water electrolysis for hydrogen and oxygen production. He discovered that, when switched off, an electrolysis cell constructed with sulfuric acid and platinum catalysts produced a small current. Mond and Langer first composed the appellation "fuel cell," where, in 1889, they developed an electrolyte-supported cell with porous Pt electrodes that operated on H_2 and O_2 [27]. The operating temperature, efficiency, electrolyte content, applications, and ionic transport mechanism are all used to classify fuel cells.

Solid oxide fuel cell (SOFC) offers relatively very high competence among all the types of fuel cells, fuel flexibility (hydrogen, natural gas, biogas from biomass [28–32], and gases made from coal), and low emissions, which led to the use of SOFCs as future power generation technology [33, 34]. It shows high efficiency (>60% efficiency) with clean environment credentials [35]. Hence, SOFCs can be used as one of the most suitable, sustainable energy sources. SOFC can also be used as an extensive power generation system and cogeneration application combined with the micro-CHP system. Portable power generation [36] and easy transportation [37] are other advantages of SOFC. In addition, SOFCs can support patients in hospitals and also supply power to residential areas at the same time. Such heterogeneous use may be available in SOFC [38]. There are several large manufacturers of SOFCs that can meet the electricity needs of people during this pandemic (as seen in Table 1). Each company manufactures different types of SOFCs, depending on each usage scenario.

In the current pandemic situation, the use of SOFC is essential in meeting this enormous energy demand. Thus, SOFC will play an important role by producing sufficient portable energy that is more sustainable than current fossil fuels.

2. Solid Oxide Fuel Cells (SOFCs)

Highly polluting fossil fuels are a concern for both environmental and economic reasons. This has resulted in more attention being paid to fuel cells, which are widely believed to be the future of electricity generation and are an area of extensive research in the scientific field. An electrochemical device known as a solid oxide fuel cell (SOFC) is capable of converting chemical energy to electricity directly [48–50]. An electrolyte composed of ceramic material separates the anode and cathode. The oxidation of fuel occurs at the anode, whereas the reduction of oxygen occurs at the cathode, and the transport of ions occurs throughout the electrolyte [51]. During oxidation at the anode, the electrons are released. The cathode then receives these electrons, and the reduction process occurs. This movement of electrons between the anode and the cathode generates electricity [52]. Thus, the

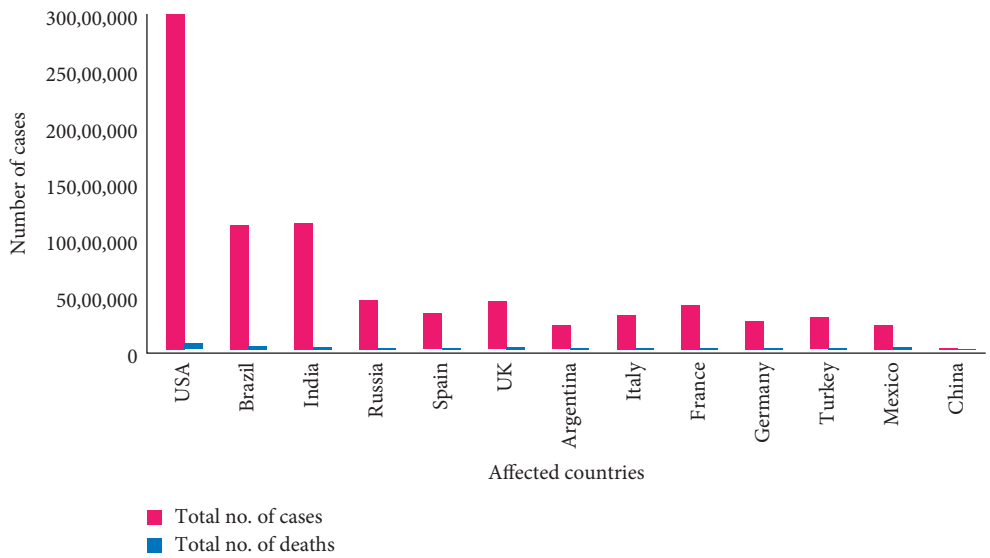

Figure 1: The most affected countries with COVID-19 in the world [7].

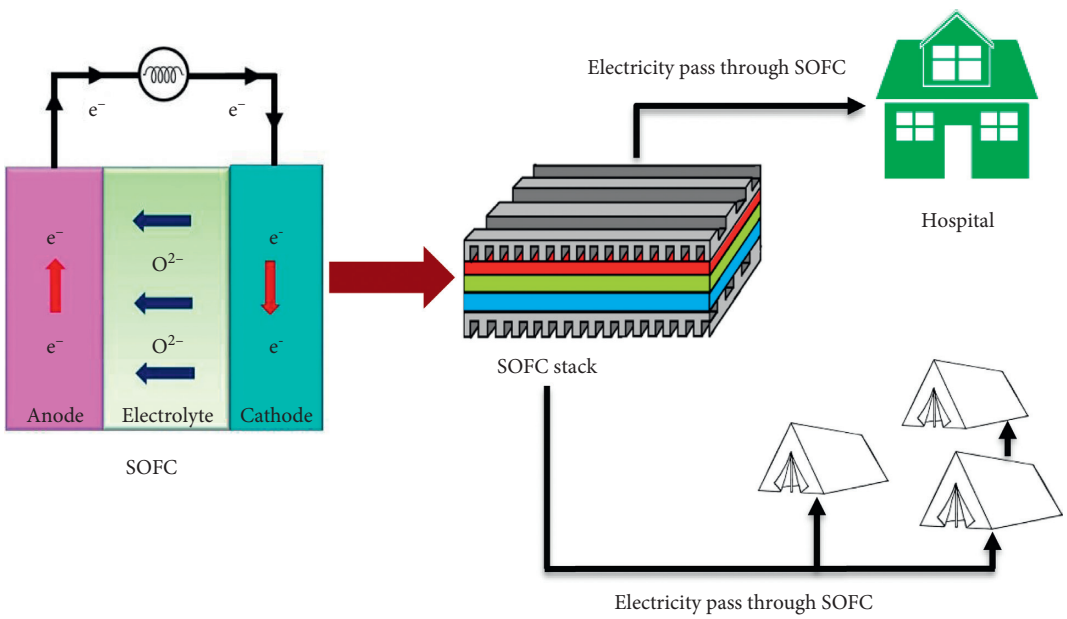

Figure 2: Power supply systems based on solid oxide fuel cells from the main building of the hospital to the temporary hospital extensions [24].

Table 1: List of SOFC companies with applications.

Company name	Applications	Origin	Ref.
Adelan Ltd.	Portable and mobile products	UK	[39]
Bloom Energy Corporation	200 to 300 kilowatts of power operating 24 × 7 with the highest efficiency of power solution used in on-grid and off-grid sections	USA	[40]
Ceres Power Limited	CHP (combined heat and power) for commercial and residential buildings	UK	[41]
Convion Ltd.	50–300 kW range of power output for distributed power generation and industrial self-generation purposes	Finland	[42]
Elcogen AS	High-power range SOFC stack from kilowatt range to megawatt systems used in residential areas, commercial and industrial transportation, and energy storage	Estonia	[43]
FuelCell Energy, Inc.	2.8 MW of ultraclean power to supply directly to the electric grid	USA	[44]
Hexis AG	1000 watts as electrical output for the public grid	Germany	[45]
SOLIDpower S.p.A.	Micro-CHP unit combined with SOFC for residential and small commercial buildings	Germany	[46]
Sunfire GmbH	Off-grid power	Germany	[47]

conventional solid oxide fuel cell (SOFC) can be used for energy generation with zero polluting emissions, with water as its only emission, as shown in Figure 3.

The oxidation takes place at the anode side [54]:

$$H_2 + O^{2-} = H_2O + 2e^- \quad (1)$$

and the reduction occurs at the cathode as

$$\frac{1}{2}O_2 + 2e^- = O^{2-} \quad (2)$$

Therefore, the overall reaction is

$$H_2 + \frac{1}{2}O_2 = H_2O \quad (3)$$

It is noteworthy that the whole efficiency of a SOFC depends on the inputs (H_2 as fuel and O_2) and outputs (electricity, heat, and water). For input parameters, mass and energy balance must be considered to analyze the cell efficiency. For output parameters, energy and mass balances for water, electrical, and heat energy should also be considered. All these terms can be effectively determined via the current and voltage of the whole cell.

An ion-conducting oxide membrane is typically used in solid oxide fuel cells (SOFCs). This oxide ion-conducting SOFC performs between 700°C and 1000°C, which is a very high-temperature range. SOFCs have numerous benefits when operated at high temperature. In essence, expensive platinum (Pt) and ruthenium (Ru) catalysts are not needed [35], and high temperatures prevent sulfur poisoning in fuels [55].

In SOFC, the anodes play a crucial role in providing reactive sites for fuel oxidation to occur in oxide anions delivered by the electrolyte. The anode must be stable at high temperatures in reducing atmospheres consisting of H_2 to gaseous hydrocarbons, depending on the fuel source used. The anode cermet Nickel-YSZ (Ni-YSZ) was a vital discovery for the development of SOFCs [56]. This material meets all the required benchmarks for the anode. The development of a cheap, suitable material for the SOFC anode is an enduring effort [57, 58].

The SOFC electrolyte plays a vital role in conducting ionic species between the electrodes, completing the electrical circuit [59, 60]. The material should have sufficiently high ionic and low electronic conductivity to avoid a short circuit across the cell. Additionally, the material must be stable in oxidizing and reducing atmospheres at the functioning temperature and be capable of forming a thin, dense film. Currently, 8 mol% yttrium doped ZrO_2 is the electrolyte of choice for high-temperature fuel cells because of its ionic conductivity, stability, and compatibility with other cell components. However, YSZ is limited to high-temperature operations due to its poor ionic conductivity at temperatures below 800°C. A target temperature for SOFC operation is 500°C, reducing the requirement for high-temperature materials and lowering the cost [61]. This improves the balance so that the generation of heat may be used for further energy production, therefore maximizing the device's efficiency. These variables have driven the advancement of a few other materials for intermediate- and low-temperature SOFC electrolytes. The development of low-temperature SOFCs has been encouraging, for instance, the fabrication of small portable devices, e.g., laptops, industrial scanners, battery chargers, cell phones, camcorders, and other electronic devices that require extended operating life [62, 63].

Cathode materials for SOFC have been well established over the past 50 years, with extensive work done to optimize conductivity, thermal stability, and facilitating the oxygen reduction reaction. Cathode materials should be chemically compatible with the electrolyte system and have sufficiently high conductivities (typically S/cm) to enhance reactivity. The combination of ionic and electronic conductivity is required to increase the size of the triple-phase boundary (TPB), the reactive sites at the cathode where oxygen is reduced and transferred to the electrolyte. In a purely electronic conducting cathode, such as $La_{0.8}Sr_{0.2}MnO_3$ (LSM), the TPB sites are limited to the interface of cathode-electrolyte [64]. Additionally, the cathode must be chemically stable at different temperature ranges and adequate porosity to efficiently distribute gaseous oxygen through the cathode to the cathode/electrolyte interface [65].

SOFCs offer several advantages compared to other fuel cell devices. Direct utilization of hydrocarbon fuels, which can be used without any pretreatment, is one of the main benefits of SOFCs [66]. High-temperature SOFCs can be operated with different types of fuels, not only relying on pure H_2. This fuel flexibility is derived not only from the facility of direct oxidation at high temperatures but also from the high-temperature internal reforming at the anode, readily converting the natural fuels into available hydrogen or methane. Along with being fuel flexible, a solid, thermally, and mechanically stable electrolyte is another major advantage of SOFCs. Another significant benefit of SOFCs combined with heat and power (CHP) systems is to produce electricity in heating households and residential blocks. Given the fact that residential heating has been recognized as a challenging sector in the fuel cell sector to decarbonize, solid oxide fuel cells, combined with micro-CHP units, can drastically reduce associated emissions [67]. The overall efficiency of SOFC can be up to 90–95% when the heat is utilized. In the UK, the cost of gas is around £4 per kWh. If we convert it to electricity at 60% efficiency, it will cost £6 per kWh to generate electricity in the homes. In contrast, the grid's electricity cost is £14 per kWh, whereas the standard electricity cost was 16.6 p/kWh in the UK in 2019 [68]. In the USA, the electricity cost per kWh using SOFC will be around only 9 cents by the end of 2021 [69], whereas the average standard electricity cost is 13.19 cents per kWh [70]. Therefore, it is handier to use SOFCs for producing electricity from the gas at a decreased price, and the excess electricity produced from SOFC can be handed to the grid.

3. Role of SOFCs during the Pandemic COVID-19

In COVID-19, the healthcare workers are at the highest risk of transmission from the patient. The USA, the most affected

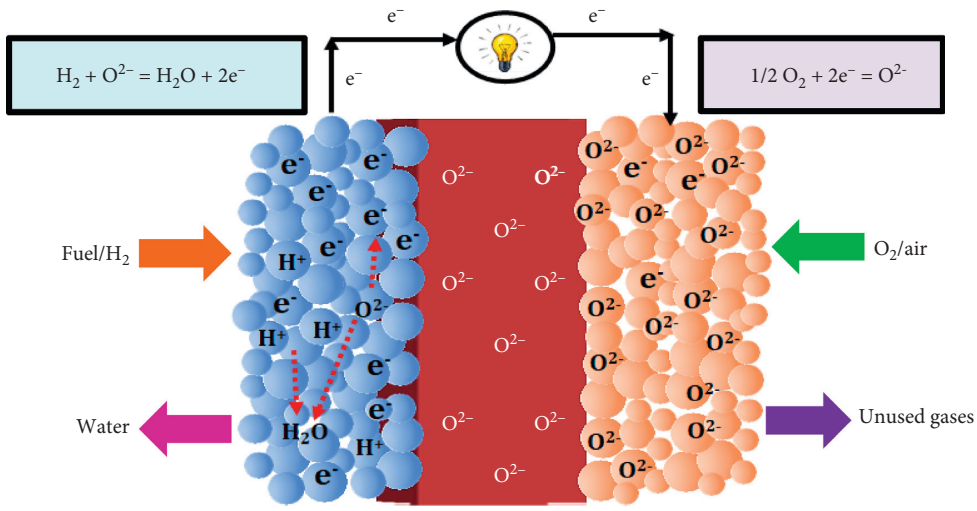

Figure 3: Schematic representation of a solid oxide fuel cell (SOFC) [53].

country as of 9 March 2021, is at the forefront of the highest affected and mortality during this pandemic, where almost 28.6 million cases were found [71]. Around 1,738,812 people were affected only in New York (as of 9 March 2021), where the number of people who died is 48,643 [72]. There are 213 hospitals in New York City [73]. Due to COVID-19, the bed numbers were increasing but still insufficient to meet demand. New York state government has already made temporary hospitals, and the hospital's main branch accommodates and treats all the affected patients. These makeshift tents need a continuous power supply to activate the ventilation systems and operate the other electronic services on time. Fuel cells can overcome these challenges and provide uninterrupted power generation at a low cost.

According to the data from the Institute of Health Matrices and Evaluation, 80,076 beds (and a total of 9,508 ICU beds) were needed to treat COVID-19 patients on 9 March 2021, in the USA, which is a much higher number [74]. College hostels, convention centers, hotels, and stadiums have been turned into hospitals to cope with the stress of COVID-19 patient's overflow, especially for those patients whose symptoms do not require intensive or emergency care. Moreover, these temporary hospitals need a continuous power supply system. The California government has ordered the administration to provide a constant power supply to the additional state-of-the-art hospitals built to deal with this disaster. Bloom Energy, one of the largest SOFC/fuel cell companies globally [75], has made a microgrid using the fuel cell system capable of powering a hospital with its makeshifts to accommodate the patient overflow. Bloom Energy has already installed a 400 kW fuel cell-based microgrid to power a temporary hospital that contains almost 100 beds in California [76]. As the SOFC system involves distributed power generation, it can easily be operated without electricity distribution lines and provided a continuous power supply during any natural or human-made disasters [77]. Therefore, this distributed electricity system, after removing the temporary tents, can be used elsewhere when the pandemic is over.

The amount of electricity bills that have to be paid every year is relatively high. As electricity is costly and vulnerable, a fuel cell-based CHP system can be used to generate electricity as much as we needed without the hassle of billing and putting the extra power on the grid. The fuel cell micro-cogeneration system is a home energy system that provides sustainable and portable energy in residences [53]. Simultaneously, social distancing is a significant issue, and people have to stay home for an extended period during this COVID-19. Countries with cold weather can mitigate their energy demand through SOFC-based micro-CHP systems. SOFC is already being applied to the individual residence with a micro-CHP system [67] in Europe. Italy, UK, Germany, and so many European countries suffer from this COVID-19, severely affected and causing financial loss. These places can expand their home electrification with micro-CHP systems [78] during this lockdown period.

It was observed that countries having hot and humid weather could also curb the death toll at a lower rate reported by Wang et al. [79]. Countries from Asia usually have a sweltering and humid atmosphere. Though the people from these regions are affected mainly due to the novel coronavirus, the death rate is relatively low concerning Europe and North America from the WHO website. Although the death toll in hot climates is low, the number of victims is high. To accommodate such a large number of patients, the hospitals also need an adequate amount of beds with all emergency treating equipment and an uninterrupted power supply. Micro-CCHP and micro-CHP, both systems, can be attractive technology for energy generation in these regions [80, 81]. Figure 4 depicts how SOFCs cogenerated with micro-CHP generate electricity for the residence and pass extra power to the grid. The use of renewable fuel with low-cost materials and the system's operational flexibility will undoubtedly increase the product demand.

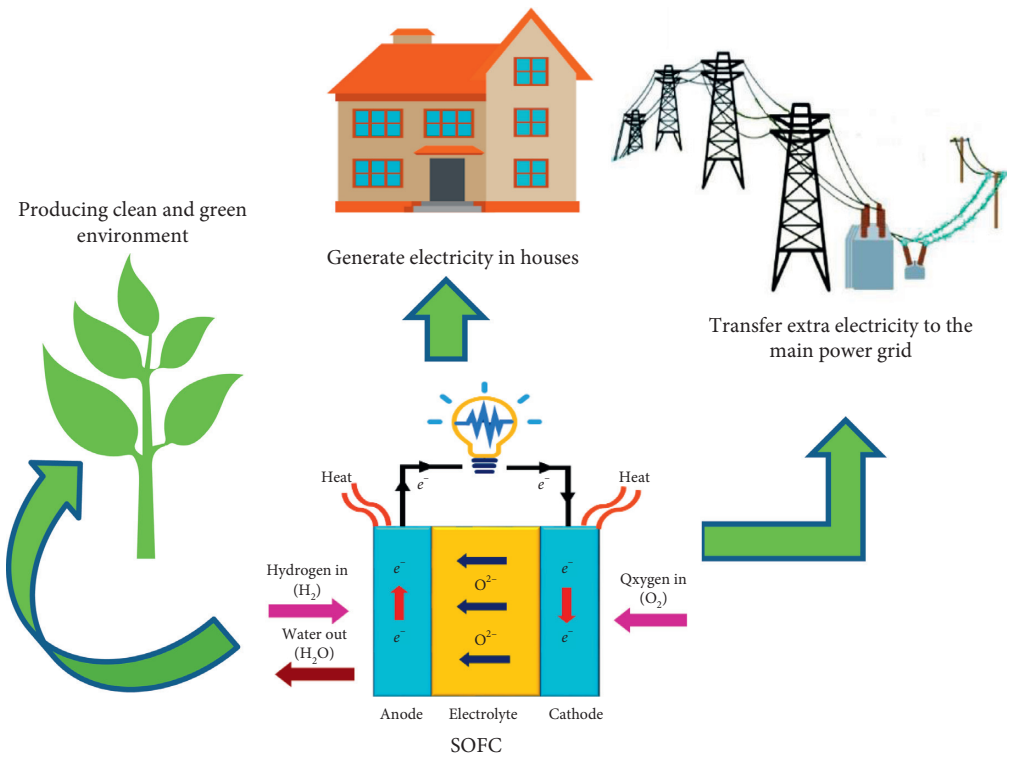

Figure 4: Schematic diagram of generating electricity through SOFC micro-CHP.

SOFC is one of the least expensive options for electricity generation [82–84]. That is why SOFC developers have been able to develop a variety of designs and integrations and market it commercially at a low cost. By changing the cell design, the overall cost of SOFC can be reduced. Therefore, the role and use of SOFC in energy production and sustainability are undeniable if this issue is taken seriously in commercialization. In addition, not just in the time of pandemic COVID-19 or any natural disaster, SOFCs have the potential to help satisfy the rising need for electricity in daily life.

4. Conclusions

At this moment in time, the whole world is struggling because of the COVID-19 pandemic. In order to cope with this pandemic, it is necessary to build public awareness about maintaining social distancing and alleviate the increased energy demand. As doctors and health workers are relentlessly trying to save lives, the role of fuel cells, mainly SOFCs, in meeting the need for extra energy in this challenging time is vital. As SOFCs can provide both on-grid and off-grid energy storage, it can be interconnected to create larger systems capable of supplying energy in an emergency. SOFCs generate an enormous amount of heat as a byproduct during its operation, which can be very useful for hospitals' heating and hot water supply. Even when the pandemic eventually ends and the mobile hospitals will be closed, these SOFC-distributed power arrangements can be used elsewhere to supply continuous electricity. The implementation of SOFCs has the added benefit of being sustainable as well as having zero pollutant emissions.

Data Availability

The data used to support the findings of this study are available from the corresponding author upon request.

Conflicts of Interest

The authors declare that they have no conflicts of interest.

Acknowledgments

The award of UBD Graduate Scholarship (UGS) to Shammya Afroze by Universiti Brunei Darussalam is gratefully acknowledged.

References

[1] A. E. Gorbalenya, "The species severe acute respiratory syndrome-related coronavirus: classifying 2019-nCoV and naming it SARS-CoV-2," *Nature Microbiology*, vol. 5, no. 4, pp. 536–544, 2020.

[2] "Coronavirus: China's First Confirmed Covid-19 Case Traced Back to November 17 | South China Morning Post." https://www.scmp.com/news/china/society/article/3074991/coronavirus-chinas-first-confirmed-covid-19-case-traced-back (accessed May 09, 2020).

[3] World Health Organization (WHO), *Novel Coronavirus (2019-nCoV), Situation Report-1, 21 January 2020*, https://www.who.int/docs/default-source/coronaviruse/situation-reports/20200121-sitrep-1-2019-ncov.pdf, WHO, Geneva, Switzerland, 2020, https://www.who.int/docs/default-source/coronaviruse/situation-reports/20200121-sitrep-1-2019-ncov.pdf.

[4] M. S. Reza, A. K. Hasan, S. Afroze, M. S. A. Bakar, J. Taweekun, and A. K. Azad, "Analysis on preparation, application, and recycling of activated carbon to aid in COVID-19 protection," *International Journal of Integrated Engineering*, vol. 12, no. 5, pp. 233–244, 2020.

[5] S. Afroze, M. S. Reza, Q. Cheok, J. Taweekun, and A. K. Azad, "Solid oxide fuel cell (SOFC); A new approach of energy generation during the pandemic COVID-19," *International Journal of Integrated Engineering*, vol. 12, no. 5, pp. 245–256, 2020.

[6] "WHO Director-General's Opening Remarks at the Media Briefing on COVID-19 - 11 March 2020." https://www.who.int/dg/speeches/detail/who-director-general-s-opening-remarks-at-the-media-briefing-on-covid-19---11-march-2020 (accessed May 09, 2020).

[7] "COVID Live Update-Worldometer." https://www.worldometers.info/coronavirus/(accessed Apr. 24, 2021).

[8] E. Qing and T. Gallagher, "SARS coronavirus redux," *Trends in Immunology*, vol. 41, no. 4, pp. 271–273, 2020.

[9] M. Z. Tay, C. M. Poh, L. Rénia, P. A. MacAry, and L. F. P. Ng, "The trinity of COVID-19: immunity, inflammation and intervention," *Nature Reviews Immunology*, vol. 20, no. 6, pp. 363–374, 2020.

[10] W. J. Guan, Z. Y Ni, Y Hu et al., "Clinical characteristics of coronavirus disease 2019 in China," *The New England Journal of Medicine*, vol. 382, no. 18, pp. 1708–1720, 2020.

[11] Q. Li, X. Guan, P. Wu et al., "Early transmission dynamics in Wuhan, China, of novel coronavirus-infected pneumonia," *New England Journal of Medicine*, vol. 382, no. 13, pp. 1199–1207, 2020.

[12] L. Dong, S. Hu, and J. Gao, "Discovering drugs to treat coronavirus disease 2019 (COVID-19)," *Drug Discoveries & Therapeutics*, vol. 14, no. 1, pp. 58–60, 2020.

[13] F. Zhou, T. Yu, R. Du et al., "Clinical course and risk factors for mortality of adult inpatients with COVID-19 in Wuhan, China: a retrospective cohort study," *The Lancet*, vol. 395, no. 10229, pp. 1054–1062, 2020.

[14] K. Dhama, K. Sharun, R. Tiwari et al., "COVID-19, an emerging coronavirus infection: advances and prospects in designing and developing vaccines, immunotherapeutics, and therapeutics," *Human Vaccines & Immunotherapeutics*, vol. 16, no. 6, pp. 1232–1238, 2020.

[15] M. Bayat, Y. Asemani, and S. Najafi, "Essential considerations during vaccine design against COVID-19 and review of pioneering vaccine candidate platforms," *International Immunopharmacology*, vol. 97, Article ID 107679, 2021.

[16] "Oxford COVID-19 vaccine begins human trial stage—NDM Research Building." https://www.ndmrb.ox.ac.uk/about/news/oxford-covid-19-vaccine-begins-human-trial-stage (accessed May 10, 2020).

[17] A. M. Zaki, S. Van Boheemen, T. M. Bestebroer, A. D. M. E. Osterhaus, and R. A. M. Fouchier, "Isolation of a novel coronavirus from a man with pneumonia in Saudi Arabia," *New England Journal of Medicine*, vol. 367, no. 19, pp. 1814–1820, 2012.

[18] W. E. Parmet and M. S. Sinha, "Covid-19-the law and limits of quarantine," *New England Journal of Medicine*, vol. 382, no. 15, pp. e28–E283, 2020.

[19] N. Ali and F. Islam, "The effects of air pollution on COVID-19 infection and mortality—a review on recent evidence," *Frontiers in Public Health*, vol. 8, Article ID 580057, 2020.

[20] X. Wu, R. C. Nethery, B. M. Sabath, D. Braun, and F. Dominici, "Exposure to air pollution and COVID-19 mortality in the United States," *Science Advances*, vol. 6, no. 45, 2020.

[21] W.-J. Guan, X.-Y. Zheng, K. F. Chung, and N.-S. Zhong, "Impact of air pollution on the burden of chronic respiratory diseases in China: time for urgent action," *The Lancet*, vol. 388, no. 10054, pp. 1939–1951, 2016.

[22] E. Conticini, B. Frediani, and D. Caro, "Can atmospheric pollution be considered a co-factor in extremely high level of SARS-CoV-2 lethality in Northern Italy?" *Environmental Pollution*, vol. 261, Article ID 114465, 2020.

[23] D. Gielen, F. Boshell, D. Saygin, M. D. Bazilian, N. Wagner, and R. Gorini, "The role of renewable energy in the global energy transformation," *Energy Strategy Reviews*, vol. 24, pp. 38–50, 2019.

[24] "Commitment to Fighting COVID-19 | Bloom Energy." https://www.bloomenergy.com/covid19 (accessed May 10, 2020).

[25] V. Cascos, L. Troncoso, J. A. Alonso, and M. T. Fernández-Díaz, "Design of new Ga-doped SrMoO 3 perovskites performing as anode materials in SOFC," *Renewable Energy*, vol. 111, pp. 476–483, 2017.

[26] J. M. Andújar and F. Segura, "Fuel cells: history and updating. A walk along two centuries," *Renewable and Sustainable Energy Reviews*, vol. 13, no. 9, pp. 2309–2322, 2009.

[27] S. M. Haile, "Fuel cell materials and component," *Acta Materialia*, vol. 51, no. 19, pp. 5981–6000, 2003.

[28] M. S. Reza, S. N. Islam, S. Afroze et al., "Evaluation of the bioenergy potential of invasive *Pennisetum purpureum* through pyrolysis and thermogravimetric analysis," *Energy, Ecology and Environment*, vol. 5, no. 2, pp. 118–133, 2020.

[29] M. S. Reza, C. S. Yun, S. Afroze et al., "Preparation of activated carbon from biomass and its' applications in water and gas purification, a review," *Arab Journal of Basic and Applied Sciences*, vol. 27, no. 1, pp. 208–238, 2020.

[30] M. S. Reza, S. Afroze, M. S. A. Bakar et al., "Biochar characterization of invasive *Pennisetum purpureum* grass: effect of pyrolysis temperature," *Biochar*, vol. 2, no. 2, pp. 239–251, 2020.

[31] M. S. Reza, A. Ahmed, W. Caesarendra et al., "*Acacia holosericea*: an invasive species for bio-char, bio-oil, and biogas production," *Bioengineering*, vol. 6, no. 2, p. 33, 2019.

[32] N. Radenahmad, M. S. Reza, M. S. A. Bakar et al., "Evaluation of the bioenergy potential of temer musa: an invasive tree from the African desert," *International Journal of Chemical Engineering*, vol. 2021, Article ID 6693071, 10 pages, 2021.

[33] S. Afroze, N. Torino, M. S. Reza et al., "Structure-conductivity relationship of PrBaMnMoO6-δ through in-situ measurements: a neutron diffraction study," *Ceramics International*, vol. 47, no. 1, pp. 541–546, 2021.

[34] S. Afroze, N. Torino, P. F. Henry, M. Sumon Reza, Q. Cheok, and A. K. Azad, "Insight of novel layered perovskite PrSrMn2O5+δ: a neutron powder diffraction study," *Materials Letters*, vol. 261, Article ID 127126, 2020.

[35] A. B. Stambouli and E. Traversa, "Solid oxide fuel cells (SOFCs): a review of an environmentally clean and efficient source of energy," *Renewable and Sustainable Energy Reviews*, vol. 6, no. 5, pp. 433–455, 2002.

[36] R. Mücke, N. H. Menzler, H. P. Buchkremer, and D. Stöver, "Cofiring of thin zirconia films during SOFC manufacturing," *Journal of the American Ceramic Society*, vol. 92, no. SUPPL. 1, pp. S95–S102, 2009.

[37] J. Garche and L. Jörissen, "Applications of Fuel Cell Technology: Status and Perspectives," 2015. Accessed: Nov. 06, 2019. [Online]. Available: http://www.electrochem.org.

[38] A. Choudhury, H. Chandra, and A. Arora, "Application of solid oxide fuel cell technology for power generation-A review," *Renewable and Sustainable Energy Reviews*, vol. 20, pp. 430–442, 2013.
[39] "Adelan Solid Oxide Fuel Cell Company | SOFC Applications for Industry." https://adelan.co.uk/(accessed May 11, 2020).
[40] "Home | Bloom Energy." https://www.bloomenergy.com/ (accessed May 11, 2020).
[41] "Welcome to ceres-pioneers of unique technology." https://www.ceres.tech/ (accessed May 11, 2020).
[42] "Fuel cell systems for distributed power generation markets - Convion." http://convion.fi/ (accessed May 11, 2020).
[43] "Elcogen-solid oxide cells and stacks." https://elcogen.com/ (accessed May 11, 2020).
[44] "FUELCELL ENERGY | Ultra-Clean, efficient, reliable power." https://www.fuelcellenergy.com (accessed May 11, 2020).
[45] "Hexis A. G." http://www.hexis.com/en (accessed May 11, 2020).
[46] "Home-SOLIDpower." https://www.solidpower.com/en/ (accessed May 11, 2020).
[47] "Sunfire–Energy Everywhere-Sunfire." https://www.sunfire.de/en/ (accessed May 11, 2020).
[48] S. Afroze, A. Karim, Q. Cheok, S. Eriksson, and A. K. Azad, "Latest development of double perovskite electrode materials for solid oxide fuel cells: a review," *Frontiers in Energy*, vol. 13, no. 4, pp. 770–797, 2019.
[49] S. Afroze, A. M. Abdalla, N. Radenahmad, Q. C. Hoon Nam, and A. K. Azad, "Synthesis, structural and thermal properties of double perovskite NdSrMn2O6 as potential anode materials for solid oxide fuel cells," in *Proceedings of 7th Brunei International Conference on Engineering and Technology 2018 (BICET 2018)*Bandar Seri Begawan, Brunei, November 2018.
[50] S. Afroze, N. Torino, P. F. Henry, M. S. Reza, Q. Cheok, and A. K. Azad, "Neutron and X-ray powder diffraction data to determine the structural properties of novel layered perovskite PrSrMn2O5+δ," *Data in Brief*, vol. 29, Article ID 105173, 2020.
[51] N. Jaiswal, K. Tanwar, R. Suman, D. Kumar, S. Upadhyay, and O. Parkash, "A brief review on ceria based solid electrolytes for solid oxide fuel cells," *Journal of Alloys and Compounds*, vol. 781, pp. 984–1005, 2019.
[52] S. P. S. Shaikh, A. Muchtar, and M. R. Somalu, "A review on the selection of anode materials for solid-oxide fuel cells," *Renewable and Sustainable Energy Reviews*, vol. 51, pp. 1–8, 2015.
[53] N. Radenahmad, A. T. Azad, M. Saghir et al., "A review on biomass derived syngas for SOFC based combined heat and power application," *Renewable and Sustainable Energy Reviews*, vol. 119, Article ID 109560, 2020.
[54] L. van Biert, T. Woudstra, M. Godjevac, K. Visser, and P. V. Aravind, "A thermodynamic comparison of solid oxide fuel cell-combined cycles," *Journal of Power Sources*, vol. 397, pp. 382–396, 2018.
[55] M. Gong, X. Liu, J. Trembly, and C. Johnson, "Sulfur-tolerant anode materials for solid oxide fuel cell application," *Journal of Power Sources*, vol. 168, no. 2, pp. 289–298, 2007.
[56] P. Gasper, Y. Lu, S. N. Basu, S. Gopalan, and U. B. Pal, "Effect of anodic current density on the spreading of infiltrated nickel nanoparticles in nickel-yttria stabilized zirconia cermet anodes," *Journal of Power Sources*, vol. 410-411, pp. 196–203, 2019.
[57] E. M. Brodnikovskii, "Solid oxide fuel cell anode materials," *Powder Metallurgy and Metal Ceramics*, vol. 54, no. 3-4, pp. 166–174, 2015.
[58] S. Afroze, D. Yilmaz, M. S. Reza et al., "Investigation of structural and thermal evolution in novel layered perovskite NdSrMn2O5+δ via neutron powder diffraction and thermogravimetric analysis," *International Journal of Chemical Engineering*, vol. 2020, Article ID 6642187, 7 pages, 2020.
[59] T. Yang, H. Zhao, M. Fang, K. Świerczek, J. Wang, and Z. Du, "A new family of Cu-doped lanthanum silicate apatites as electrolyte materials for SOFCs: synthesis, structural and electrical properties," *Journal of the European Ceramic Society*, vol. 39, no. 2-3, pp. 424–431, 2019.
[60] S. Afroze, H. Q. H. H. Absah, M. S. Reza et al., "Structural and electrochemical properties of lanthanum silicate apatites La10Si6−x−0.2AlxZn0.2O27−δ for solid oxide fuel cells (SOFCs)," *International Journal of Chemical Engineering*, vol. 2021, Article ID 6621373, 10 pages, 2021.
[61] K. H. Ng, H. A. Rahman, and M. R. Somalu, "Review: enhancement of composite anode materials for low-temperature solid oxide fuels," *International Journal of Hydrogen Energy*, vol. 44, no. 58, pp. 30692–30704, 2019.
[62] I. Sreedhar, B. Agarwal, P. Goyal, and S. A. Singh, "Recent advances in material and performance aspects of solid oxide fuel cells," *Journal of Electroanalytical Chemistry*, vol. 848, Article ID 113315, 2019.
[63] A. Bieberle-Hütter, D. Beckel, A. Infortuna et al., "A micro-solid oxide fuel cell system as battery replacement," *Journal of Power Sources*, vol. 177, no. 1, pp. 123–130, 2008.
[64] J. Sacanell, J. Hernández Sánchez, A. E. Rubio López et al., "Oxygen reduction mechanisms in nanostructured La0.8Sr0.2MnO3 cathodes for solid oxide fuel cells," *The Journal of Physical Chemistry C*, vol. 121, no. 12, pp. 6533–6539, 2017.
[65] Y. Chen, W. Zhou, D. Ding et al., "Advances in cathode materials for solid oxide fuel cells: complex oxides without alkaline earth metal elements," *Advanced Energy Materials*, vol. 5, no. 18, Article ID 1500537, 2015.
[66] S. Park, J. M. Vohs, and R. J. Gorte, "Direct oxidation of hydrocarbons in a solid-oxide fuel cell," *Nature*, vol. 404, no. 6775, pp. 265–267, 2000.
[67] J. Kupecki, "Off-design analysis of a micro-CHP unit with solid oxide fuel cells fed by DME," *International Journal of Hydrogen Energy*, vol. 40, no. 35, pp. 12009–12022, 2015.
[68] "Energy Per kWh-Compare Gas and Electric Prices." https://www.gocompare.com/gas-and-electricity/guide/energy-per-kwh/# (accessed Mar. 09, 2021).
[69] "Bloom Energy Charts a Future in Hydrogen Fuel Cells, Electrolysis and Carbon Capture | Greentech Media." https://www.greentechmedia.com/articles/read/bloom-energy-sees-future-in-hydrogen-fuel-cells-electrolysis-and-carbon-capture (accessed Mar. 09, 2021).
[70] "Electricity Rates by State (February 2021) – Electric Choice." https://www.electricchoice.com/electricity-prices-by-state/(accessed Mar. 09, 2021).
[71] "Coronavirus (COVID-19) in the U.S.-Statistics & Facts | Statista." https://www.statista.com/topics/6084/coronavirus-covid-19-in-the-us/(accessed May 10, 2020).
[72] "Cuomo Rolls Out New Regulations for Nursing Homes: Live Updates-the New York Times." https://www.nytimes.com/2020/05/10/nyregion/coronavirus-new-york-update.html (accessed May 11, 2020).
[73] "Hospital: Bed Types." https://profiles.health.ny.gov/hospital/bed_type/Total+Beds (accessed May 11, 2020).

[74] "COVID-19." https://covid19.healthdata.org/united-states-of-america (accessed May 12, 2020).
[75] I. Staffell, D. Scamman, A. Velazquez Abad et al., "The role of hydrogen and fuel cells in the global energy system," *Energy & Environmental Science*, vol. 12, no. 2, pp. 463–491, 2019.
[76] "Powering Field Hospitals to Save Lives during the COVID-19 Outbreak | Bloom Energy." https://www.bloomenergy.com/blog/powering-field-hospitals-save-lives-during-covid-19-outbreak (accessed May 12, 2020).
[77] S. Kang and K.-Y. Ahn, "Dynamic modeling of solid oxide fuel cell and engine hybrid system for distributed power generation," *Applied Energy*, vol. 195, pp. 1086–1099, 2017.
[78] A. D. Hawkes, P. Aguiar, B. Croxford, M. A. Leach, C. S. Adjiman, and N. P. Brandon, "Solid oxide fuel cell micro combined heat and power system operating strategy: options for provision of residential space and water heating," *Journal of Power Sources*, vol. 164, no. 1, pp. 260–271, 2007.
[79] J. Wang, K. Tang, K. Feng et al., "Impact of temperature and relative humidity on the transmission of COVID-19: a modelling study in China and the United States," *BMJ Open*, vol. 11, no. 2, Article ID e043863, 2021.
[80] J. Y. Wu, J. L. Wang, S. Li, and R. Z. Wang, "Experimental and simulative investigation of a micro-CCHP (micro combined cooling, heating and power) system with thermal management controller," *Energy*, vol. 68, pp. 444–453, 2014.
[81] W. Yang, Y. Zhao, V. Liso, and N. Brandon, "Optimal design and operation of a syngas-fuelled SOFC micro-CHP system for residential applications in different climate zones in China," *Energy and Buildings*, vol. 80, pp. 613–622, 2014.
[82] K. Alanne, A. Salo, A. Saari, and S.-I. Gustafsson, "Multi-criteria evaluation of residential energy supply systems," *Energy and Buildings*, vol. 39, no. 12, pp. 1218–1226, 2007.
[83] D. Zhang, S. Evangelisti, P. Lettieri, and L. G. Papageorgiou, "Optimal design of CHP-based microgrids: multiobjective optimisation and life cycle assessment," *Energy*, vol. 85, pp. 181–193, 2015.
[84] J. Sadhukhan, "Distributed and micro-generation from biogas and agricultural application of sewage sludge: comparative environmental performance analysis using life cycle approaches," *Applied Energy*, vol. 122, pp. 196–206, 2014.

Hindawi
International Journal of Chemical Engineering
Volume 2021, Article ID 8894768, 8 pages
https://doi.org/10.1155/2021/8894768

Research Article

Electrochemical Performance Improvement of the Catalyst of the Methanol Microfuel Cell Using Carbon Nanotubes

Mohammad Kazemi Nasrabadi,[1] **Amir Ebrahimi-Moghadam**,[2] **Ravinder Kumar**,[3] **and Narjes Nabipour**[4]

[1]*Aerospace Engineering Department, Shahid Sattari Aeronautical University of Science and Technology, Tehran, Iran*
[2]*Faculty of Mechanical Engineering, Shahrood University of Technology, Shahrood, Iran*
[3]*Department of Mechanical Engineering, Lovely Professional University, Phagwara, Punjab 14411, India*
[4]*Institute of Research and Development, Duy Tan University, Da Nang 550000, Vietnam*

Correspondence should be addressed to Mohammad Kazemi Nasrabadi; kazemi@ssau.ac.ir

Received 17 August 2020; Accepted 20 May 2021; Published 28 May 2021

Academic Editor: Nicole Vorhauer-Huget

In this research, the electrocatalytic activity of platinum-ruthenium nanoparticles on carbon nanotubes and carbon black in methanol oxidation reaction has been investigated. Moreover, the electrochemical performance of a single passive direct methanol fuel cell run by these two different electrocatalysts has been reported. Physical characterization and electrochemical tests reveal the superiority of PtRu on carbon nanotubes. Based on the voltammetry outcomes, it was found that methanol oxidation reaction kinetics has been improved on the nanotube-supported catalyst. The current density of oxidation reaction has increased up to 62% in nanotube sample compared to carbon black-supported one. The electrochemical test results have shown that the carbon nanotubes increase the performance of the microfuel cell by 37% at maximum power density, compared to the carbon black. Moreover, the resistance of the samples supported by carbon nanotubes to poisonous intermediate species has been found 3% more than carbon black-supported one. According to the chronoamperometry test results, it was concluded that the performance and sustainability of the carbon nanotube electrocatalyst show a remarkable improvement compared to carbon black electrocatalyst in the long term.

1. Introduction

Different clean energy technologies have been evaluated in recent years to replace the current energy systems, which use fossil fuels [1]. Among different power generation technologies with lower greenhouse gas emissions in comparison with the conventional fossil fuel-based systems, fuel cells have some advantages [2]. The fuel cells convert the chemical energy of the fuel directly into heat and power through a set of electrochemical reactions. The main part of the fuel cell structure is the membrane electrode assembly (MEA), which specifies the type and the function of the cell [3]. High efficiency, environmental compatibility, simple maintenance, zero noise pollution, and ability to employ different fuels such as hydrogen, methanol, and ethanol, are some of the benefits of the fuel cells [4]. Direct methanol fuel cells (DMFCs) are a subcategory of polymer-exchange membrane fuel cells in which methanol is consumed as fuel. The utilization of liquid fuel facilitates the safer use of this technology for a wider range of applications, from portable electronic devices to electric vehicles [5].

Even though much research has been conducted on methanol fuel cells during the recent two decades, there are still challenges that should be addressed. One of these challenges is the high ratio of Pt in the catalyst layer [5]. Improving the properties of the catalyst substrate can lead to higher efficiency and reduce the consumption of the expensive Pt. Due to high specific surface area, high electrical conductivity, and low price, carbon black (CB) is commonly used as the electrocatalyst support in DMFCs. On the other

hand, CB tends to corrode rapidly and suffers from low efficiency in metal catalyst utilization [6]. Efforts are focused on superseding new materials with extraordinary physical and electrical properties such as carbon nanotube (CNT) [7].

Graphite nanofiber has been investigated as the Pt support in proton exchange membrane fuel cell. The outcomes showed that the support corrosion was reduced by one-half, and catalyst stability was improved compared to Pt/CB [8]. Three-dimensional graphene-supported PtAu composite has been characterized for the methanol oxidation reaction. The outcomes indicated high specific surface area and higher electrocatalytic activity compared with commercially used Pt/CB [9]. The electrochemical characterization of ultrasonically treated multiwalled carbon nanotubes as the PtRu support illustrated the superiority of catalyst in electrochemically active surface area and activity in the methanol oxidation reaction [10]. By comparing MWCNT/Pt, DWCNT/Pt, and SWCNT/Pt, Dongmulati and Baikeri [11] concluded that using MWCNT/Pt as a catalyst in fuel cells is better than two other ones due to its high specific surface area.

Noncarbon catalyst supports such as mesoporous silicas and metal oxide-based materials have attracted attention in recent years. Yu et al. [12] used Pt-Ru-$NiTiO_3$ nanoparticles and found that it has higher catalytic activity than PtRu/C, and the onset potential became 60 mV more negative. Bilondi et al. [13] coated PtRu nanoparticles with cerium oxide (CeO_2) which increased the oxidation reaction activity of methanol compared to bare PtRu electrocatalyst, and the power density increased 1% per each cm^2.

Since there are few studies focused on the passive DMFCs, the current research has concentrated on the comparison of the electrochemical performance of PtRu/CNT and PtRu/CB. In the next step, the authors have fabricated MEAs comprised of PtRu/CNT and PtRu/CB on the anode side and Pt/CNT and Pt/CB on the cathode side to investigate the electrocatalytic performance under the operating condition of a single passive DMFC.

2. Materials and Methods

2.1. Electrocatalyst Synthesis. Carbon black, multiwalled carbon nanotubes, hexachloroplatinic acid ($H_2PtCl_6.6H_2O$), ruthenium chloride ($RuCl.3H_2O$), 2-propanol, sodium borohydride ($NaBH_4$), sodium hydroxide (NaOH), acetone, and deionized water have been used to synthesize and prepare the catalyst samples. In this study, the impregnation reduction method has been employed for the synthesis of electrocatalyst PtRu with a 1 : 1 atomic ratio, using sodium borohydride as a reducing agent and isopropanol as the solvent. 100 mg of CB or MWCNT has been dispersed homogeneously in 100 mL of a solvent consisting of isopropyl alcohol (IPA) and deionized water in the ratio of 2 : 1 in the ultrasonic probe device for 1 hour. After that, the required amount of platinum and ruthenium solution (20% of PtRu catalyst by weight) is added to the suspension and is put on the stirrer at the ambient temperature for one more hour. In the next step, the pH of the solution has been set to 10 using 0.5 M of NaOH solution. Then, the required amount of 0.1 M $NaBH_4$ solution in deionized water as the reducing agent was added drop by drop to the suspension on the magnetic mixer at 60°C for 2 to 3 hours. The synthesis process is continued for 12 hours at ambient temperature to complete the reduction reaction. Finally, the electrocatalyst has been washed and centrifuged several times and dried at 60°C in a vacuumed oven for 12 hours [2].

2.2. Physical Measurements. The crystallite structure has been studied by X-ray diffraction (XRD) technique using X'Pert Philips (PW3040) diffractometer with Cu-Kα ($\lambda = 1.5406$ Å) source at 40 kV and 40 mA. The surface morphology of the electrocatalysts was determined by scanning electron microscopy (SEM, Nova NanoSEM 450) and transmission electron microscopy (TEM, Philips EM208S) at 100 kV. To investigate the presence and percentage of key elements, energy-dispersive X-ray spectroscopy (EDX) was employed by the Bruker XFlash module.

2.3. Electrochemical Measurements. Voltammetry is the main tool to gain important information about the performance of the catalyst and some of its crucial properties including active surface area, activity, and durability in MOR. In this research, a three-electrode cell connected to a potentiostat (NANO RNF) has been utilized to determine the electrochemical performance of electrocatalysts. It is comprised of a glassy carbon electrode (GCE) with a diameter of 2 mm as the working electrode, the platinum plate electrode as the counterelectrode, and a half-cell of Ag/AgCl as the reference electrode.

To prepare catalyst ink, 1 mg of PtRu/C electrocatalyst has been dispersed in 300 μL of deionized water and isopropanol in a ratio of 1 : 5. Then, 20 μL of 5% Nafion solution was added as an ionomer to facilitate the exchange of the ions produced in the oxidation reaction. An ultrasonic bath for 30 min has been employed to disperse catalyst ink uniformly. After this step, 10 μL of catalyst ink has been coated on the GCE surface under infrared light. The amount of loaded PtRu on electrode surface area is calculated as 0.2 mg/cm^2.

Voltammetry measurements including cyclic voltammetry (CV) and chronoamperometry have been performed at room temperature in 0.5 M H_2SO_4 containing 1 M methanol solution as an electrolyte in an oxygen-free condition [7].

The schematic diagram of the methodology process has been illustrated in Figure 1.

3. Results and Discussion

3.1. Microscopic Analysis. The surface morphology and nanostructure of the electrocatalysts have been investigated by SEM and TEM analyses. Figures 2(a) and 2(b) present the SEM images of CB and CNT, respectively. As can be observed, there is a distinct structural difference between CB and CNT. CB primary particles are spherical with a diameter of 50 nm and form aggregated clusters, while the twisted seaweed structure of CNT has formed a porous network.

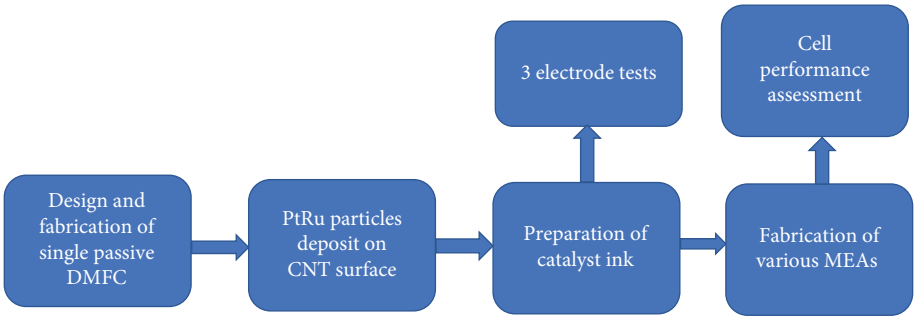

Figure 1: Schematic view of the methodology.

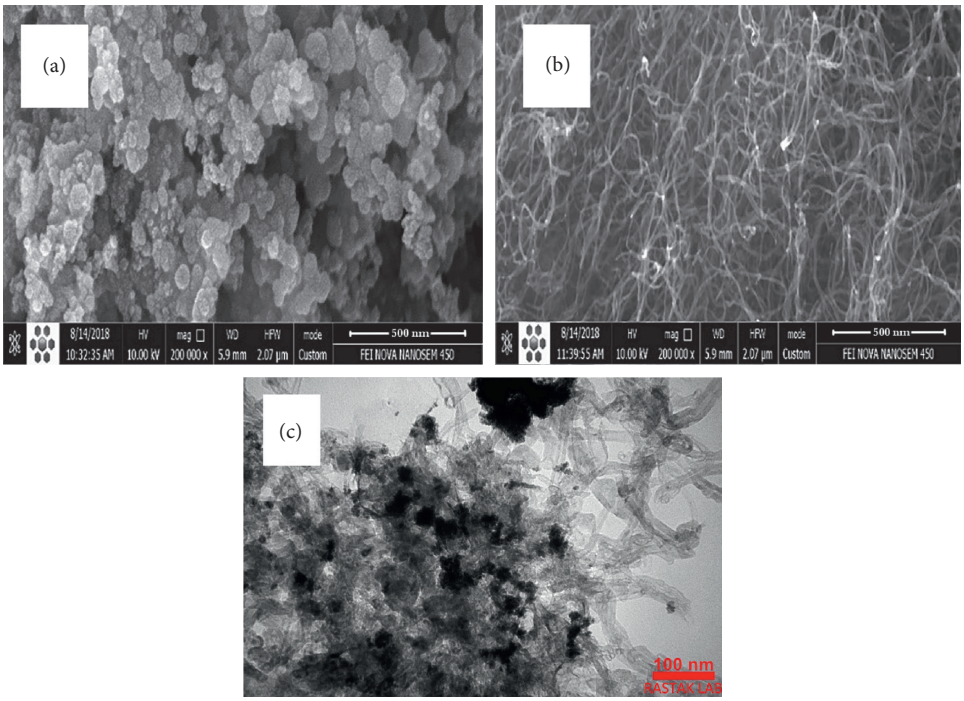

Figure 2: SEM images of CB (a) and CNT (b). TEM image of PtRu/CNT (c).

Moreover, the TEM image of the synthesized PtRu bimetallic electrocatalyst on CNTs at the scale of 100 nm is presented in Figure 2(c). It is obvious that the agglomerated metal nanoparticles are very well distributed on the CNT surface. The large surface area of CNTs has the potential to absorb metal nanoclusters more efficiently than that of CB [14].

The composition of chemical elements in synthesized samples is determined using the EDX test (Figure 3). According to the EDX analysis results, the real weight percentage of PtRu is 22% (atomic percentage of Pt, Ru, and CB is 1.2%, 1%, and 97.8%, respectively) and the real weight percentage of Pt is 21% (atomic percentage of Pt is 1.6%) which indicates that the synthesis of metal catalyst on the carbon support is well done [15]. The real amount of Pt and PtRu in all of the samples is about the same as the theoretical value of 20%.

3.2. Spectroscopic Analysis. Figure 4 shows the XRD results of PtRu/CB and PtRu/CNT samples. The first diffraction peak appeared at the angle of 26° and 27° corresponds to the graphite C (002) base plane. The XRD patterns of both electrocatalysts display four diffraction peaks related to the face-centered cubic crystal structure of Pt, corresponding to the (111), (200), (220), and (311) planes, while the Ru atoms are replaced in the Pt crystal structure.

From Figure 4, some crucial data on the PtRu catalysts can be calculated. Table 1 illustrates the calculated parameters. The lower lattice parameter of the electrocatalysts compared with pure Pt ($l_{Pt/C} = 0.392$ nm) indicates that Ru has entered into the Pt lattice and an alloy of Pt and Ru was formed. The average crystal size and surface area of PtRu/CNT catalyst are 3.6 nm and 86 m^2/g, respectively. However, the corresponding data for the PtRu/CB catalyst are 4.56 nm and 69 m^2/g, respectively. It can be observed from the above

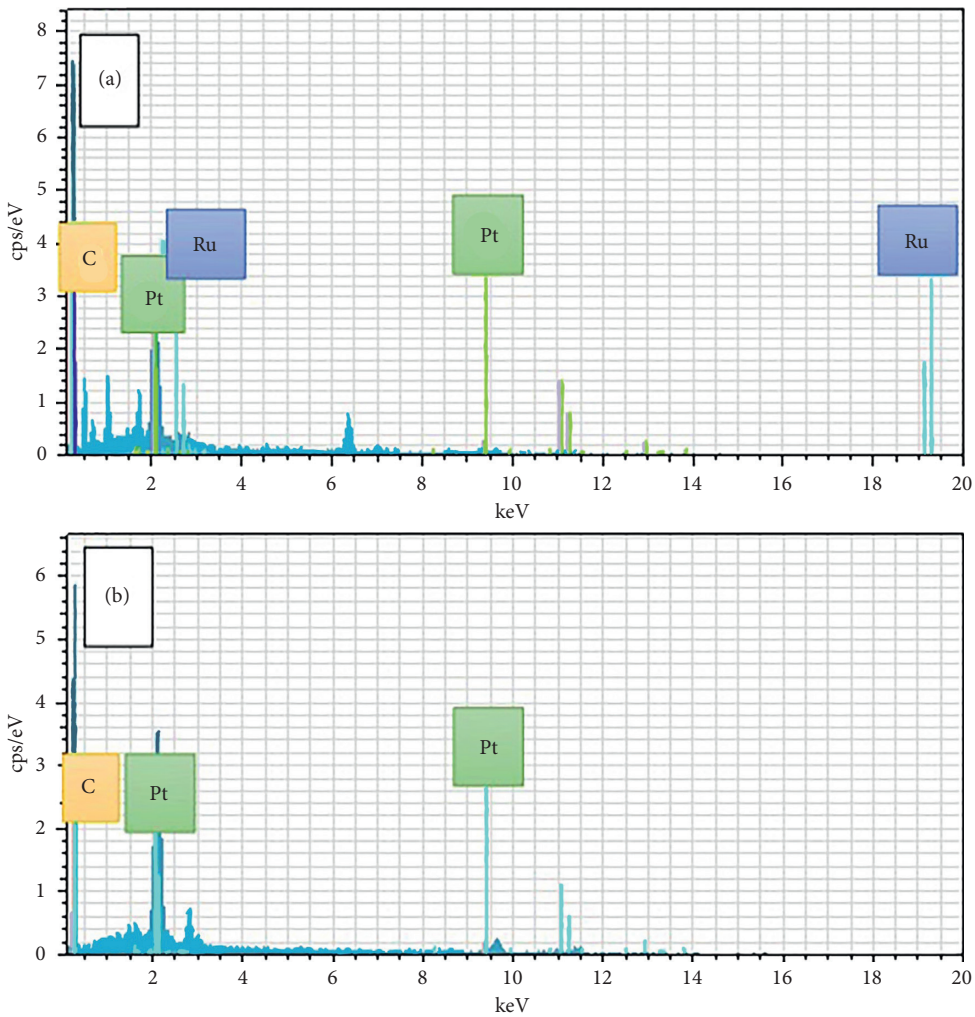

Figure 3: EDX image of (a) PtRu loaded on the anode and (b) Pt loaded on the cathode.

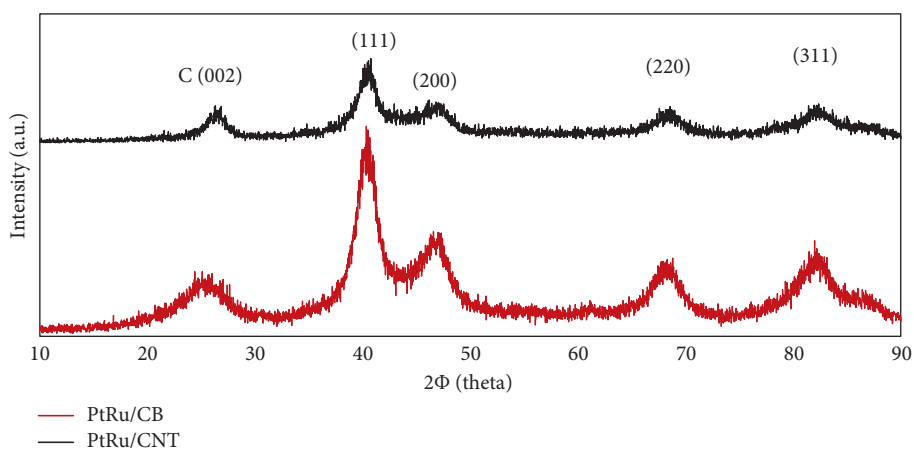

Figure 4: The XRD patterns of the synthesized samples for the anodes.

data that although the Ru atomic fraction is approximately the same, the CNT surface provides stronger active sites for the nucleation and stabilization of metal nanoparticles. The interaction between PtR nanoparticles and CNT surface resulted in a 25% increase in crystal surface area.

3.3. Electrochemical Analysis. Cyclic voltammetry in a 0.5 M solution of sulfuric acid is an effective method to measure the active electrochemical surface area of different synthesized catalysts. Figure 5 shows the voltammetry graph obtained for PtRu/CB and PtRu/CNT. It is obvious that, by

Table 1: Parameters calculated based on the XRD test.

Catalysts	Crystallite size (nm)	Lattice parameter (Å)	Ru atomic fraction	Metal surface area (m^2/g)
PtRu/CB	4.56	3.884	0.25	69
PtRu/CNT	3.6	3.887	0.22	86

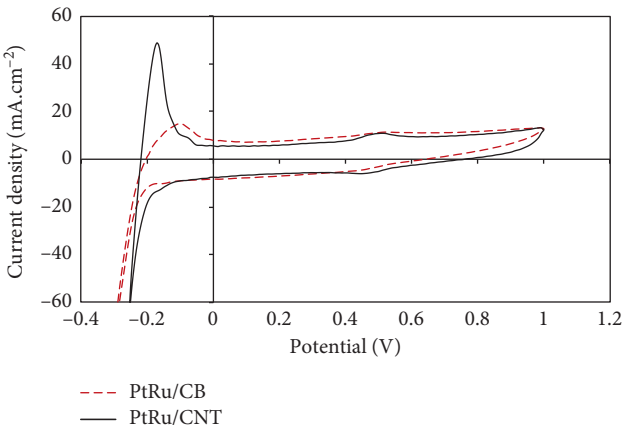

Figure 5: Cyclic voltammetry test of synthesized samples.

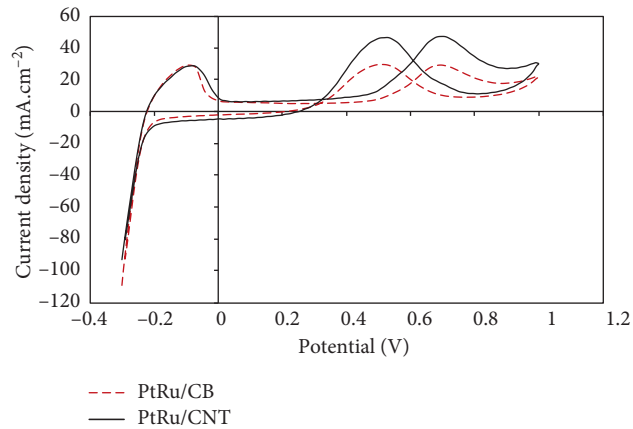

Figure 6: Cyclic voltammetry test of synthesized samples.

increasing the voltage in the forward scan, a current peak has occurred at −0.19 V which shows desorption of hydrogen on the electrocatalyst surface. On the other hand, the current drop in the reverse scan is attributed to the adsorption of hydrogen on the electrocatalyst surface. The electrochemically active surface area (ECSA) can be calculated from Figure 5. Using double-layer region correction, the amount of ECSA for PtRu/CNT was calculated at 52.3 m^2/g which was much higher than that of PtRu/CB catalyst (27.6 m^2/g) [16]. The higher ECSA of the CNT-supported catalyst was attributed to the smaller particle size of the PtRu which provided more accessible active sites in the PtRu/CNT catalyst.

The catalyst performance in methanol oxidation reaction (MOR) is investigated by the CV technique in 0.5 M sulfuric acid and 1 M methanol solution at room temperature. As Figure 6 shows, the first peak at 0.7 V in the forward scan (I_f) is related to the MOR activity. The second peak at 0.52 V in the reverse scan (I_r) is related to oxidation of intermediate species created during MOR. I_f/I_r ratio is used to specify the resistance poisonous intermediate species [17].

PtRu/CNT has shown much higher electrochemical activity compared with PtRu/CB catalyst. The maximum MOR current density of 47.2 mA/cm^2 is obtained for PtRu/CNT, which is 1.6 times higher than that for PtRu/CB catalyst. Considering the larger ECSA of the PtRu/CNT compared to the PtRu/CB catalyst, the MOR results were predictable. Moreover, I_f/I_r ratio shows that PtRu/CNT catalyst is more resistant to CO. To express the results of this analysis more clearly, Table 2 shows the information obtained.

The durability improvement of the electrocatalyst is one of the important research interests in the area of the fuel cell. The long-term electrocatalytic activity and stability of the samples were tested and examined using chronoamperometry analysis (Figure 7). In this test, a constant potential of 0.7 V is applied to the electrodes for 1000 s, in an N_2 saturated solution containing 0.5 M H_2SO_4 and 1 M methanol. The current density is plotted as a function of the time.

Table 2: Comparison of the electrocatalytic activity, current density, and catalytic resistance.

Samples	I_f (mA cm^{-2})	V_f (V)	I_r (mA cm^{-2})	V_r (V)	I_f/I_r
PtRu/CB	29.22	0.695	29.58	0.51	0.98
PtRu/CNT	47.2	0.7	46.51	0.525	1.014

The current density drops rapidly at first which is due to the production and accumulation of the intermediate species. Because of the higher resistance of PtRu/CNT to poisoning species, it has less initial current drop compared to PtRu/CB, and after 1000 s, the current density reaches 21.1 mA/cm^2. On contrary, PtRu/CB sample shows less resistance to the intermediate species, the highest current drop is observed at first seconds and finally reaches 8.3 mA/cm^2, abound one-third of the CNT-supported PtRu [18].

Finally, after that, the fabricated passive methanol microfuel cell was built (Figure 8), and it was tested using two different sets of MEAs including CNT-based MEA (Pt/CNT (cathode) and PtRu/CNT (anode)) and CB-based MEA (Pt/CB (cathode) and PtRu/CB (anode)). The analysis was conducted in a 3 M methanol solution, and the polarization curves are shown in Figures 9 and 10.

By comparing the current-voltage curves of the two MEAs, at lower current densities (0–10 mA/cm^2)—which is the region related to losses of activation energy and methanol crossover—a sharp decrease in the voltage is observed. At medium current densities (up to 70 mA/cm^2), the activity improvement of the catalyst leads to a more stable voltage. At high current densities (more than 70 mA/

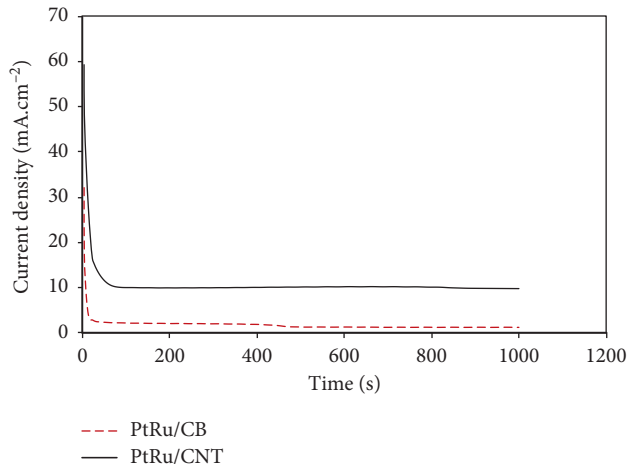

Figure 7: Chronoamperometry test of synthesized samples.

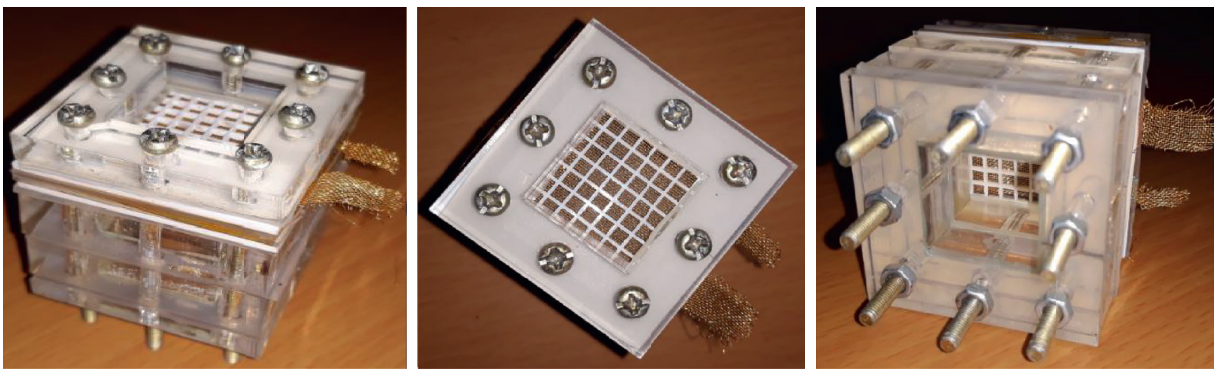

Figure 8: Schematic view of the fabricated methanol microfuel cell.

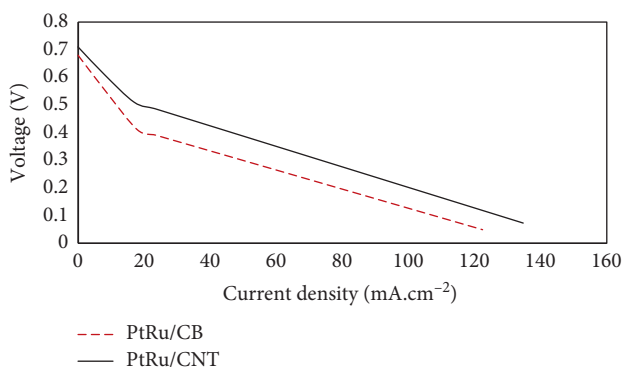

Figure 9: Polarization curves of the two sets of MEAs under the cell operation.

cm^2), due to an increase in the chemical reaction rate, fuel consumption is increased. Hence, less porosity of CB structure compared to the MWCNT results in weaker fueling and sharper voltage drop. Therefore, it can be concluded that using PtRu/CNT can lead to a decrease in losses due to facilitating the mass transfer [19].

Because of the efficient dispersion and distribution of the catalyst particles on CNT, a significant increase in the power production capacity of the fuel cell is observed. Table 3 summarizes the results of the fuel cell tests. Based on the outcomes, by using CNT-supported electrocatalysts, the performance of the fuel cell has been increased about 37.1%

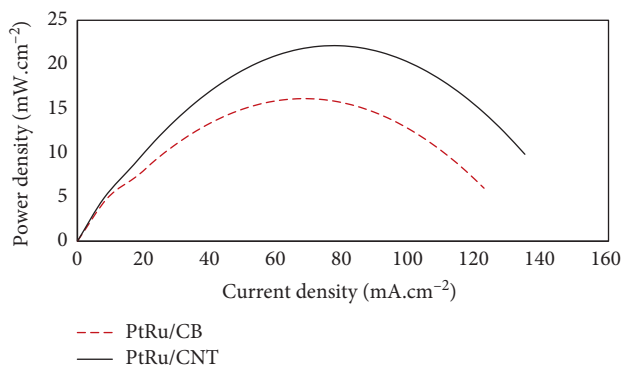

Figure 10: Power curves of the two sets of MEAs under the cell operation.

Table 3: Comparison of results of fuel cell maximum output power for different catalysts.

Test temperature (°C)	Cathode catalysts	Anode catalysts	Maximum power density (mW cm^{-2})	Supported catalyst
60	Pt	PtRu	16/133	CB
60	Pt	PtRu	22/12	MWCNT

at maximum power density. The utilization of CNT instead of CB has increased fuel cell power and improves catalytic activity.

4. Conclusions

In this study, MWCNTs were employed to support PtRu particles as the electrocatalyst for DMFC, and the performance was compared with that of commercially used carbon black. Based on the tests and analysis conducted in this study, the following results have been obtained.

The EDX, SEM, and TEM analyses have confirmed the deposition of PtRu nanoclusters on the surface of carbon material and determined the weight percentage of elements. The XRD patterns have indicated the smaller metal particles and the higher surface area of electrocatalyst on the CNT compared to CB, which stems from stronger interaction between CNT and metal catalyst.

Based on the cyclic voltammetry test in acid solution, the active electrochemical surface area for PtRu/CNT was calculated as 52.3 m^2/g which is 1.9 times higher than that of PtRu/CB (27.6 m^2/g). The CV test also showed superior activity of PtRu/CNT in methanol oxidation reaction (with 47.2 mA/cm^2 and 61.5% increase compared to PtRu/CB) and higher I_f/I_r ratio, which means more tolerance to poisonous species. The chronoamperometry test showed that CNT-supported electrocatalysts are more durable and have a higher current density in the long term. Cell test revealed that maximum power density for PtRu/CNT and PtRu/CB was 22.12 mW/cm^2 and 16.133 mW/cm^2, respectively. Methanol oxidation onset potential which is a criterion for kinetic improvement of the MOR CNT has dropped from 5.3 V for PtRu/CB to 4.4 V for PtRu/CNT. In conclusion, based on the extracted outcomes from this research, deploying CNTs in supporting PtRu nanoparticles remarkably improves the activity of electrocatalysts and consequently increases the output power of the fuel cell.

Abbreviations

CB: Carbon black
CNT: Carbon nanotube
CV: Cyclic voltammetry
DMFC: Direct methanol fuel cell
ECSA: Electrochemically active surface area
EDX: Energy-dispersive X-ray spectroscopy
GCE: Glassy carbon electrode
MEA: Membrane electrode assembly
MOR: Methanol oxidation reaction
MWCNT: Multiwalled carbon nanotubes
SEM: Scanning electron microscopy
TEM: Transmission electron microscopy
XRD: X-ray diffraction.

Data Availability

The experimental data used to support the findings of this study are included within the article.

Conflicts of Interest

The authors declare that they have no conflicts of interest.

References

[1] M. Ghalandari, H. Forootan Fard, A. Komeili Birjandi, and I. Mahariq, "Energy-related carbon dioxide emission forecasting of four European countries by employing data-driven methods," *Journal of Thermal Analysis and Calorimetry*, 2020, inpress.

[2] M. Khodaverdi, F. Pourfayaz, and M. Mehrpooya, "Nitrogen-doped graphene prepared by low-temperature thermal treatment as an electrocatalyst support for methanol oxidation," *Fuel Cells*, inpress, 2021.

[3] M. Farooque and H. C. Maru, "Fuel cells-the clean and efficient power generators," *Proceedings of IEEE*, vol. 89, no. 12, pp. 1819–1829, 2001.

[4] J. Lidderdale and T. J. P. Day, "Fuel cell CHP for buildings," in *Proceedings of CIBSE Annual Conference*, London, UK, November 2006.

[5] L. Wei, X. Yuan, and F. Jiang, "A three-dimensional non-isothermal model for a membraneless direct methanol redox fuel cell," *Journal of Power Sources*, vol. 385, pp. 130–140, 2018.

[6] S. Samad, K. S. Loh, W. Y. Wong et al., "Carbon and non-carbon support materials for platinum-based catalysts in fuel cells," *International Journal of Hydrogen Energy*, vol. 43, no. 16, pp. 7823–7854, 2018.

[7] H. Forootan Fard, M. Khodaverdi, F. Pourfayaz, and M. H. Ahmadi, "Application of N-doped carbon nanotube-supported Pt-Ru as electrocatalyst layer in passive direct methanol fuel cell," *International Journal of Hydrogen Energy*, vol. 45, no. 46, pp. 25307–25316, 2020.

[8] L. Lu, H. Xu, R. Ren, and H. Zhao, "Graphite nanofibers as catalyst support for proton exchange membrane fuel cells at 80°C," in *Proceedings of 2010 Asia-Pacific Power Energy Engineering Conference*, pp. 1–4, IEEE, Chengudu, China, March 2010.

[9] H. D. Jang, S. K. Kim, H. Chang et al., "Three-dimensional crumpled graphene-based platinum-gold alloy nanoparticle composites as superior electrocatalysts for direct methanol fuel cells," *Carbon*, vol. 93, pp. 869–877, 2015.

[10] C. Yang, X. Hu, D. Wang et al., "Ultrasonically treated multi-walled carbon nanotubes (MWCNTs) as PtRu catalyst supports for methanol electrooxidation," *Journal of Power Sources*, vol. 160, no. 1, pp. 187–193, 2006.

[11] N. Dongmulati and S. Baikeri, "Comparison of different types of polypyrimidine/CNTs/Pt hybrids in fuel cell catalysis," *Journal of Nanoparticle Research*, vol. 20, no. 8, 2018.

[12] X. Yu, Q. Zhang, Y. Ling, Z. Yang, and H. Cheng, "Promoted stability and electrocatalytic activity of PtRu electrocatalyst derived from coating by cerium oxide with high oxygen storage capacity," *Applied Surface Science*, vol. 455, pp. 815–820, 2018.

[13] A. M. Bilondi, M. Abdollahzadeh, M. J. Kermani, H. Heidary, and P. Havaej, "Numerical study of anode side CO contamination effects on PEM fuel cell performance; and mitigation methods," *Energy Convers Manag*, vol. 177, pp. 519–534, 2018.

[14] R. Praats, M. Käärik, A. Kikas et al., "Electrocatalytic oxygen reduction reaction on iron phthalocyanine-modified carbide-derived carbon/carbon nanotube composite electrocatalysts," *Electrochimica Acta*, vol. 334, Article ID 135575, 2020.

[15] M. Kesava and K. Dinakaran, "SnO2 nanoparticles dispersed carboxylated Poly(arylene ether sulfones) nanocomposites for proton exchange membrane fuel cell (PEMFC) applications," *International Journal of Hydrogen Energy*, vol. 46, no. 1, pp. 1121–1132, 2021.

[16] A. K. Choudhary and H. Pramanik, "Addition of rhenium (Re) to Pt-Ru/f-MWCNT anode electrocatalysts for enhancement of ethanol electrooxidation in half cell and single direct ethanol fuel cell," *International Journal of Hydrogen Energy*, vol. 45, no. 24, pp. 13300–13321, 2020.

[17] H. Kuang, Y. Cheng, C. Q. Cui, and S. P. Jiang, "Carbon nanotubes-supported Pt electrocatalysts for O2 reduction reaction-effect of number of nanotube walls," *Journal of Nanoscience and Nanotechnology*, vol. 20, no. 5, pp. 2736–2745, 2020.

[18] K. Miecznikowski, "WO3 decorated carbon nanotube supported PtSn nanoparticles with enhanced activity towards electrochemical oxidation of ethylene glycol in direct alcohol fuel cells," *Arabian Journal of Chemistry*, vol. 13, no. 1, pp. 1020–1031, 2020.

[19] X. Ren, Q. Lv, L. Liu, A. Liu, B. Liu, and Y. Wang, "Facile synthesis of alloyed PtNi/CNTs electrocatalyst with enhanced catalytic activity and stability for methanol oxidation," *Inorganic Chemistry Communications*, vol. 120, Article ID 108130, 2020.

Hindawi
International Journal of Chemical Engineering
Volume 2021, Article ID 6621373, 10 pages
https://doi.org/10.1155/2021/6621373

Research Article

Structural and Electrochemical Properties of Lanthanum Silicate Apatites $La_{10}Si_{6-x-0.2}Al_xZn_{0.2}O_{27-\delta}$ for Solid Oxide Fuel Cells (SOFCs)

Shammya Afroze,[1] Hidayatul Qayyimah Hj Hairul Absah,[2] Md Sumon Reza,[1] Mahendra Rao Somalu,[3] Jun-Young Park,[4] Saeed Nekoonam,[5] Alibek Issakhov,[6] and Abul Kalam Azad[1]

[1]*Faculty of Integrated Technologies, Universiti Brunei Darussalam, Jalan Tungku Link, Gadong, Bandar Seri Begawan, BE 1410, Brunei Darussalam*
[2]*Faculty of Science, Universiti, Brunei Darussalam Jalan Tungku Link, Gadong, BE 1410, Bandar Seri Begawan, Brunei Darussalam*
[3]*Faculty of Science, Universiti Kebangsaan Malaysia, X 43600 Bangi, Selangor, Malaysia*
[4]*Department of Nanoscience and Advanced Materials Engineering, Sejong University, HMC, 209 Neungdong-ro, Gunja-dong, Gwangjin-gu, Seoul 05006, Republic of Korea*
[5]*Department of Renewable Energies and Environment, Faculty of New Sciences and Technologies, University of Tehran, Tehran, Iran*
[6]*Faculty of Mechanics and Mathematics, Department of Mathematical and Computer Modelling, Al-Farabi Kazakh National University, Almaty, Kazakhstan*

Correspondence should be addressed to Saeed Nekoonam; saeednekoonam@gmail.com and Abul Kalam Azad; abul.azad@ubd.edu.bn

Received 25 October 2020; Revised 18 December 2020; Accepted 6 January 2021; Published 19 January 2021

Academic Editor: Mohammad Hossein Ahmadi

An excellent oxide ion conductivity with high oxygen transportation of lanthanum silicate apatite at the solid oxide fuel cell (SOFC) can be achieved through the solid-state reaction method. The doped $La_{10}Si_{6-x-0.2}Al_xZn_{0.2}O_{27-\delta}$ ($x = 0.2$ and 0.4) materials sintered at 1600°C accomplished crystallinity and crystal structure of apatite-type. The structural and electrochemical characterizations of $La_{10}Si_{6-x-0.2}Al_xZn_{0.2}O_{27-\delta}$ ($x = 0.2$ and 0.4) were executed using X-ray diffraction (XRD), scanning electron microscopy (SEM), energy dispersive X-ray spectroscopy (EDX), and electrochemical impedance spectroscopy (EIS) measurements. The total oxide ion conductivities of $La_{10}Si_{6-x-0.2}Al_xZn_{0.2}O_{27-\delta}$ ($x = 0.2$ and 0.4) were measured from low to intermediate operating temperature range (450 to 800°C) using electrochemical impedance spectroscopy. Room temperature XRD patterns of $La_{10}Si_{6-x-0.2}Al_xZn_{0.2}O_{27-\delta}$ ($x = 0.2$ and 0.4) exhibited $La_{10}Si_6O_{27}$ apatite phase with space group $P6_3/m$ as the main phase with the minor appearance of La_2SiO_5 as an impurity phase. The highest total oxide ion conductivity of 3.24×10^{-3} Scm^{-1} and corresponding activation energy of 0.30 eV at 800°C were obtained for $La_{10}Si_{5.6}Al_{0.2}Zn_{0.2}O_{26.7}$ which contains a low concentration of Al^{3+} dopant.

1. Introduction

Solid oxide fuel cells (SOFCs) are now especially popular with everyone for producing renewable or clean energy gadgets for electricity generation [1, 2]. SOFC provides promising features, such as high performance, environmentally clean power generation, and versatile fuel flexibility (hydrogen, hydrocarbons such as methane, or natural gas [3–8]), as a renewable energy system [9]. One of the most extensively used fuels of SOFC is syngas, produced from the

thermochemical conversion of biomass [10–13]. This electrochemical device is made of dense solid oxide electrolyte located between two perforated electrodes [14–18]. Many researchers have developed new electrolytes that provide stability and high oxide ion or proton conductivity at low to moderate operating temperatures (400 to 700°C) [19–23]. SOFC displays beneficial characteristics at these temperatures, such as a wide variety of materials, longer life and reliability, and low cost. Proton-conducting electrolytes are being tried to substitute yttria-stabilized zirconia (YSZ) [24–27]. One of the recent electrolytes with solid oxide ion conductivity relative to other kinds of materials is lanthanum silicate apatite ($La_{10}Si_6O_{27}$) [27–31]. The conductivity of $La_{10}Si_6O_{27}$ offers oxygen transference numbers near unity over a wide oxygen partial pressure range and stable electrochemical performance under various gas feedstocks [32–36]. The key challenges affecting the stability and electrochemical efficiency of lanthanum silicate materials have low sinterability and the formation of secondary La_2SiO_5 phase [37–39].

Studies on various dopants that can improve the oxide ion conductivity and the interstitial oxide ion concentrations of $La_{10}Si_6O_{27}$ have been carried out [40–42]. The study shows that doping cations on the Si-site have increased the overall oxide ion conductivity of $La_{10}Si_6O_{27}$ than doping on the La-site [34]. Previous researches have also demonstrated that cation vacancies or excess oxygen have increased the oxide ion conductivity of the lanthanum silicate materials [35, 40, 41, 43–46]. Thus, a wide range of cations doping on both La- and Si-sites can enhance the oxide ion conductivity of $La_{10}Si_6O_{27}$ [47].

Recently, the single-chamber solid oxide fuel cell (SC-SOFC) over the conventional SOFC has attracted researchers due to its numerous advantages. SC-SOFC can be operated using a mixture of fuel (where hydrocarbon fuel can be used directly) without sealing [48]. Electrolyte with a porous microstructure can be used in single-chamber SOFC where the snugness of gas is not essential. In SC-SOFC, the catalytic activity occurs only between the electrodes, the partial oxidation of fuel occurs at the anode, and the oxygen reduction occurs at the cathode. Therefore, due to the uniform gas composition, the electromotive force is generated only between the two electrodes and enhances the cell performance due to the use of a mixture of air and hydrocarbon fuel. In Figure 1, methane and oxygen are separated by a porous membrane. The electrochemical reaction occurs with oxygen ions by producing carbon monoxide (CO) and hydrogen (H_2) due to the partial oxidation [48, 49].

The gas transportation through the porous electrolyte can be derived mathematically by viscous flow (Π_v) and Knudsen diffusion (Π_k) [50]:

$$\Pi = \Pi_v + \Pi_k = \frac{\varepsilon r^2}{8\eta\tau RTL} Pm + \frac{2\varepsilon\tau}{3\tau\theta_k L}\sqrt{\frac{8}{\pi RMT}}, \quad (1)$$

where ε is the porosity, r is the radius of the pore, η is the gas viscosity, τ is the tortuosity factor, R is the gas constant per mole, T is the temperature, L is the thickness of the porous medium, Pm is the mean pressure, M is the molar mass of the gas, and θ_k is the parameter coefficient of "hardness" of the walls.

In recent research, transition metal dopant such as Zn^{2+} has been found in $La_{10}Si_6O_{27}$ and improved the oxide ion conductivity of $La_{10}Si_6O_{27}$ as reported by Setsoafia et al. [40]. Other research has found that Al^{3+} dopant can also enhance the oxide ion conductivity of $La_{10}Si_6O_{27}$ as investigated by Yoshioka [41] and even by Cao and Jiang [36]. Hence, in this work, a series of new and novel doped $La_{10}Si_6O_{27}$ materials were prepared by codoping of Al^{3+} and Zn^{2+} on the Si- site through solid-state reaction which observed the correlation between sintering temperature and electrical properties. Prepared lanthanum apatite can be used in single-chamber SOFC effectively as a porous electrolyte. Noteworthy, low-cost and low-temperature cell fabrication is possible with these porous electrolytes. Thus, the lanthanum apatite structures could be a novel approach to use in a porous SC-SOFC system that consisted of a porous electrolyte, anode, and cathode as lanthanum apatite has high oxide ion conduction over a wide range of partial pressure of oxygen from 1 to 10^{-21} atm which may accelerate oxide ion conduction with low activation energy. The purpose of this study is to inspect the effects of codoping, varying concentrations of Al^{3+} with a constant concentration of Zn^{2+} on the structure to reduce the energy consumption and the oxide ion conductivity of the lanthanum silicate materials in SOFC (450 to 800°C).

2. Experimental

2.1. Sample Preparation. Lanthanum silicate of $La_{10}Si_{6-x-0.2}Al_xZn_{0.2}O_{27-\delta}$ ($x = 0.2$ and 0.4) samples were synthesized as apatite structure through the solid-state synthesis method [18, 51–56]. Initially, a total of 10 g of appropriate amount of La_2O_3, SiO, Al_2O_3, and ZnO powders were ball milled with 200 g of zirconia balls and 150 ml of ethanol at a rational speed of 250 rpm for 24 hours. After ball milling, the mixtures were then dried completely in an oven at 80°C. The powders were ground and then calcined at 1300°C for 10 hours at 5°C/min heating and cooling rates to get rid of the organics. After calcination, 2.5 g of the powders were pressed uniaxially in a mold at a constant pressure of 50 MPa and a hold-up time of 60 seconds. The produced pellets were sintered at 1600°C for 8 hours at 5°C/min heating and cooling rates.

2.2. Characterization. Structural characterizations of $La_{10}Si_{6-x-0.2}Al_xZn_{0.2}O_{27-\delta}$ ($x = 0.2$ and 0.4) were studied using XRD and SEM, weight %, and atomic % of the elements in the $La_{10}Si_{6-x-0.2}Al_xZn_{0.2}O_{27-\delta}$ ($x = 0.2$ and 0.4) compounds which were measured using EDX. Finally, the electrochemical performances of the electrolytes were investigated using EIS.

Room temperature XRD patterns of the electrolytes were obtained using Cu-K$\propto$1 radiation (wavelength, $\lambda = 1.5406$ Å) with a speed of scan of 2 degrees per minute. Microstructures of the electrolytes were obtained on JEOL

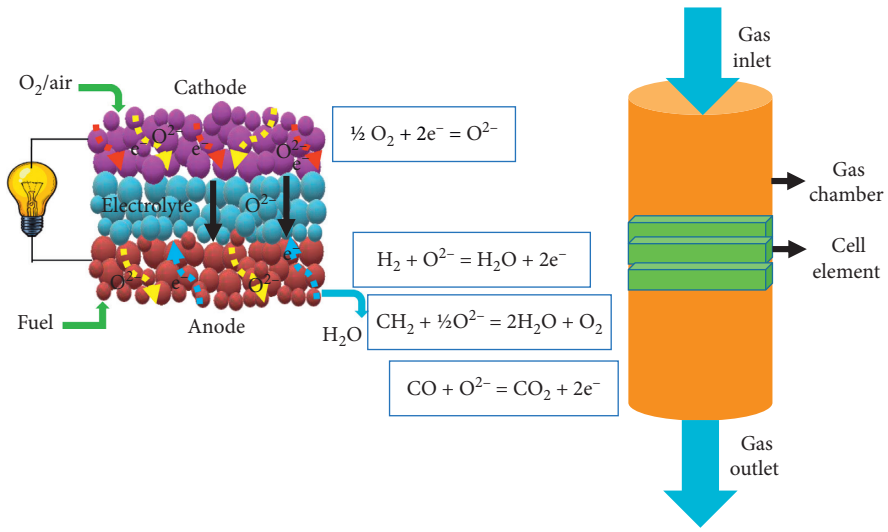

Figure 1: Schematic illustration of the all porous single-chamber SOFC. Methane (CH_4) is nourished at the anode side, while air (O_2) is introduced at the cathode and conveyed by the permeable electrolyte to the catalytic anode.

JSM-7610F scanning electron microscopy [57]. EDX is connected to the SEM device to get the weight % and atomic % of the elements in the $La_{10}Si_{6-x-0.2}Al_xZn_{0.2}O_{27-\delta}$ ($x = 0.2$ and 0.4) compounds.

Oxide ion conductivity measurements were performed using a furnace with platinum wires as current collectors. Symmetrical cells with platinum paste coating on the top and bottom surfaces of the pellet were made. A.C. impedance measurements were collected in 50°C steps in the air between 450 and 800°C using a Solartron impedance analyzer system combined with electrochemical interface controlled by Zplot electrochemical impedance software. Total resistance (sum of the bulk and grain boundary resistances) at a certain temperature was obtained from fitting the impedance plot at that temperature. The total oxide ion conductivity σ_{total} was evaluated using the following equation:

$$\sigma_{\text{total}} = \frac{t}{SR}, \tag{2}$$

where t is the thickness of the pellet, S is the surface area of the conducting paste on the pellet, and R is the total resistance. Activation energy was obtained from Arrhenius plot using the following Arrhenius equation:

$$\sigma T = \sigma_o \exp\left(-\frac{E_a}{kT}\right), \tag{3}$$

where σ, σ_o, E_a, k, T are the conductivity (Scm^{-1}), pre-exponential factor, activation energy (eV), Boltzmann constant (8.62×10^{-5} eV/K), and temperature (K), respectively. Equation (3) can be arranged as

$$\log(\sigma T) = -\frac{E_a}{k} \cdot \frac{1}{T} + \log(\sigma_o). \tag{4}$$

3. Results and Discussions

To analyze the apatite structure which was sintered at 1600°C for 8 hours in the air, the X-ray diffraction (XRD) technique was used and represented in Figure 2. The room temperature XRD patterns of the powder samples confirmed that $La_{10}Si_{6-x-0.2}Al_xZn_{0.2}O_{27-\delta}$ ($x = 0.2$ and 0.4) belongs to an apatite phase of composition $La_{10}Si_6O_{27}$ with space group $P6_3/m$. A small percentage of an impurity phase of La_2SiO_5 was detected from XRD data from the appearance of some additional peaks along with the parent apatite phase. The impurity is difficult to remove once formed even if its appearance in the phase assembly was not thermodynamically favoured [39] and this is the kind of adversity that occurs when a material is made in a solid-state method [58]. The La_2SiO_5 impurity occurred when a secondary phase La_2O_3 formed by decarburization reaction during the calcination reacted with silicate apatite in $La_{10}Si_{6-x-0.2}Al_xZn_{0.2}O_{27-\delta}$ ($x = 0.2$ and 0.4) during the sintering process [29]. La_2SiO_5 crystallizes in the monoclinic symmetry in the $P2_1/c$ space group [59]. The impurity phase is less than 5% which has no significant effect on ionic conduction. The lattice parameters of $La_{10}Si_{5.6}Al_{0.2}Zn_{0.2}O_{26.7}$ were found to be $a = b = 9.71$ Å and $c = 7.21$ Å and the lattice parameters of $La_{10}Si_{5.4}Al_{0.4}Zn_{0.2}O_{26.6}$ were found to be $a = b = 9.73$ Å and $c = 7.21$ Å. The materials have almost similar lattice parameters due to their similar chemical composition and symmetry.

SEM is a powerful technique to understand the density, grain boundaries, and phase purity [60]. Figure 3 shows the morphological structure of the lanthanum silicate apatite of $La_{10}Si_{6-x-0.2}Al_xZn_{0.2}O_{27-\delta}$ ($x = 0.2$ and 0.4) porous electrolytes. It shows that the particles of $La_{10}Si_{6-x-0.2}Al_xZn_{0.2}O_{27-\delta}$ are well connected and form open channels in the electrolyte, which allow gas infiltration through the electrolyte. The cross-section SEM analysis of apatite crystals for the abovementioned compositions showed significant dense solid materials and visible grain size with obvious grain boundaries, which accelerates the exchange of ions indicating electrolytes (Figure 3) [61, 62]. Grain sizes for the samples were approximately 1 μm. Nonuniform grains of $La_{10}Si_{6-x-0.2}Al_xZn_{0.2}O_{27-\delta}$ ($x = 0.2$ and 0.4) indicated that

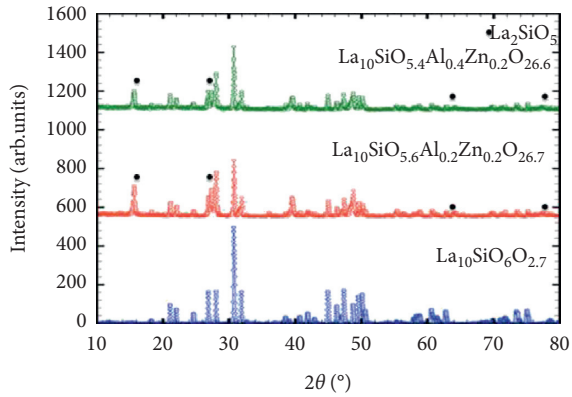

Figure 2: Room temperature XRD patterns of $La_{10}Si_{5.6}Al_{0.2}Zn_{0.2}O_{26.7}$ and $La_{10}Si_{5.4}Al_{0.4}Zn_{0.2}O_{26.6}$ sintered at 1600°C for 8 hours in air compared to room temperature XRD pattern of $La_{10}Si_6O_{27}$ sintered at 1500°C for 10 hours in air obtained.

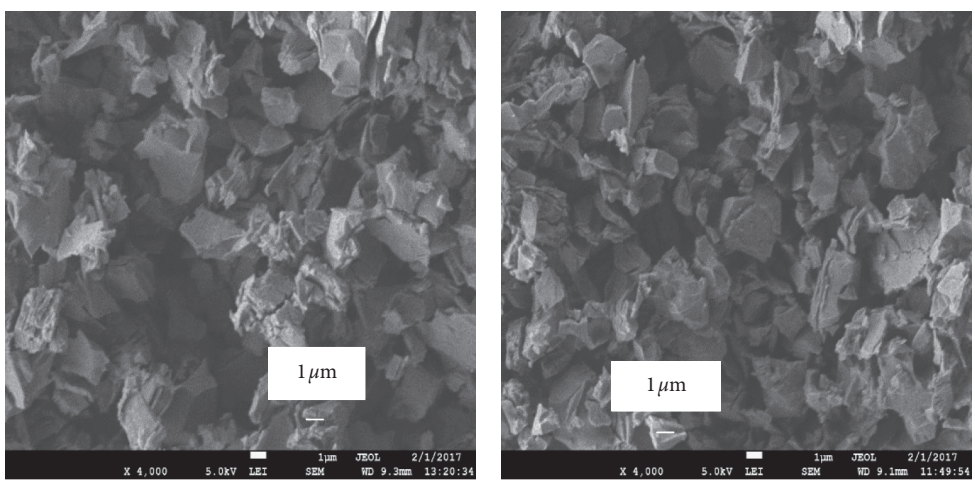

(a) (b)

Figure 3: SEM images (cross-sectional) of $La_{10}Si_{5.6}Al_{0.2}Zn_{0.2}O_{26.7}$ (left) and $La_{10}Si_{5.4}Al_{0.4}Zn_{0.2}O_{26.6}$ (right) powders sintered at 1600°C for 8 hours in air.

the milling process had reduced most of the grains into particles of closely related size to each other. This in turn aids in the formation of the apatite structure. Zn and Al codoping at the Si-site increases the density as well as the grain size which increases the ionic conductivity.

At the same time, while running SEM, the energy dispersive X-ray (EDX) analysis was performed with an utterly vacuum atmosphere. The EDX spectra (Figure 4) clearly describes that in addition to a small amount of Al and Zn components, the material contains La, Si, Al, Zn, and O. The particle sizes of $La_{10}Si_{6-x-0.2}Al_xZn_{0.2}O_{27-\delta}$ ($x = 0.2$ and 0.4) were about 1μm. Weight % and atomic % of the sintered powders obtained from EDX spectroscopy are listed in Table 1. Greater weight % of aluminium in $La_{10}Si_{5.4}Al_{0.4}Zn_{0.2}O_{26.6}$ is when the theoretical aluminium content of the $La_{10}Si_{5.4}Al_{0.4}Zn_{0.2}O_{26.6}$ compound is greater than $La_{10}Si_{5.6}Al_{0.2}Zn_{0.2}O_{26.7}$, whereas the weight % of silicon and oxygen are greater in $La_{10}Si_{5.6}Al_{0.2}Zn_{0.2}O_{26.7}$ when the theoretical silicon and oxygen contents of the $La_{10}Si_{5.6}Al_{0.2}Zn_{0.2}O_{26.7}$ compound are greater than the $La_{10}Si_{5.4}Al_{0.4}Zn_{0.2}O_{26.6}$ compound. The weight % of lanthanum and zinc in $La_{10}Si_{6-x-0.2}Al_xZn_{0.2}O_{27-\delta}$ ($x = 0.2$ and 0.4) are closely related values to each other as the theoretical compositions of lanthanum and zinc in $La_{10}Si_{6-x-0.2}Al_xZn_{0.2}O_{27-\delta}$ ($x = 0.2$ and 0.4) compounds are the same. The results show an approximate match between the weight % of elements in a compound and the theoretical composition of the elements in the compound [63].

Figure 5 compares the EIS plots of $La_{10}Si_{6-x-0.2}Al_xZn_{0.2}O_{27-\delta}$ ($x = 0.2$ and 0.4) pellets at 800°C with corresponding equivalent circuit used for fitting the Nyquist plots. The two semicircles of the Nyquist plots represent the grain conductivity and the grain boundary conductivity. The high frequency regime belongs to the grain contribution to the conductivity and the medium range frequency belongs to the grain boundary contribution to the conductivity of $La_{10}Si_{6-x-0.2}Al_xZn_{0.2}O_{27-\delta}$ ($x = 0.2$ and 0.4) [38,64]. The total oxide ion conductivity of $La_{10}Si_{6-x-0.2}Al_xZn_{0.2}O_{27-\delta}$ ($x = 0.2$ and 0.4) at a certain operating temperature was calculated using equation (2) where the total resistance was obtained by fitting

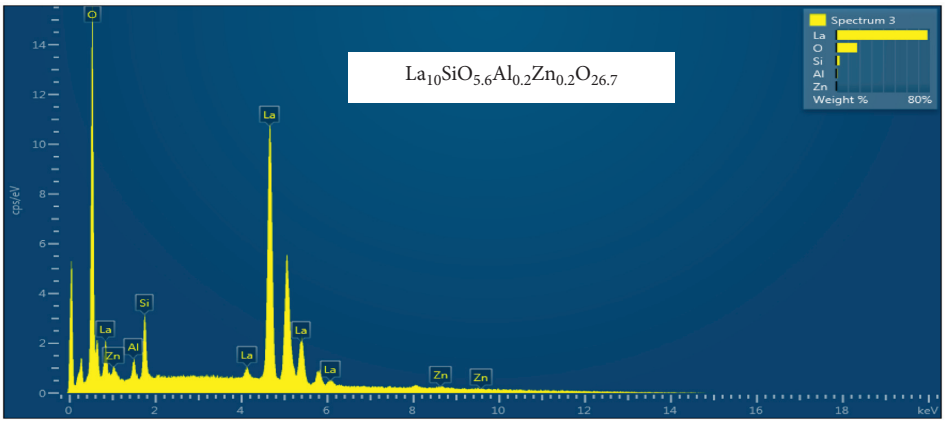

(a)

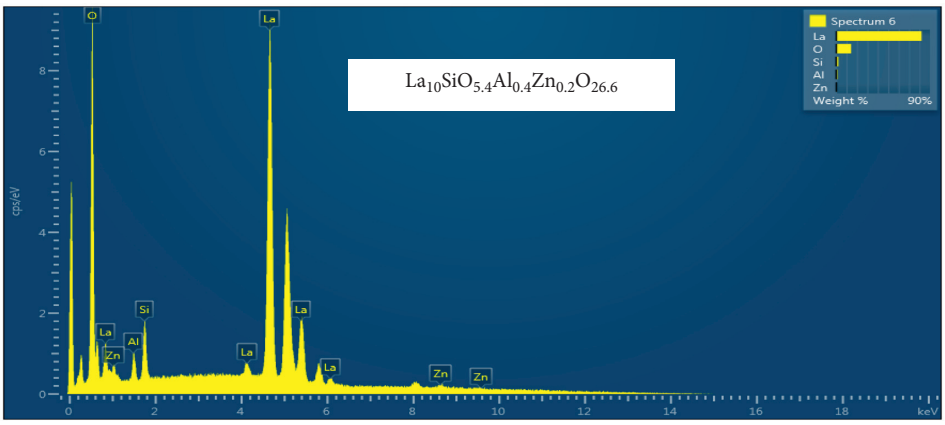

(b)

Figure 4: EDX spectra of $La_{10}Si_{5.6}Al_{0.2}Zn_{0.2}O_{26.7}$ (top) and $La_{10}Si_{5.4}Al_{0.4}Zn_{0.2}O_{26.6}$ (bottom) powders sintered at 1600°C for 8 hours in air.

Table 1: Elemental distribution of $La_{10}Si_{6-x-0.2}Al_xZn_{0.2}O_{27-\delta}$ ($x = 0.2$ and 0.4) through EDX.

Element symbol	Composition	$x = 0.2$		$x = 0.4$	
		F %	EDX %	F %	EDX %
La	10	77.88	30.73	81.99	36.62
Si	5.6	2.96	5.78	2.16	4.77
Al	0.2	0.98	2	1.17	2.7
Zn	0.2	0.31	0.26	0.35	0.33
O	26.7	17.87	61.24	14.33	55.58

the impedance plot with equivalent circuit model shown as an inset in Figure 5. Total conductivity of different compositions reported in this work and in the literature from 500 to 800°C are listed in Table 2. Overall, it can be stated that the total oxide ion conductivity of $La_{10}Si_{6-x-0.2}Al_xZn_{0.2}O_{27-\delta}$ ($x = 0.2$ and 0.4) pellets gradually increases with increasing temperature as shown in Table 2, which demonstrates that the ionic diffusion process is thermally activated [41]. $La_{10}Si_{5.6}Al_{0.2}Zn_{0.2}O_{26.7}$ obtains the highest total oxide ion conductivity of 3.24×10^{-3} Scm^{-1} at 800°C than $La_{10}Si_{5.4}Al_{0.4}Zn_{0.2}O_{26.6}$ of 2.08 x 10^{-3} Scm^{-1}. The addition of small weight % of aluminium and sintering temperature of 1600°C for 8 hours in air resulted in a good conductivity achieved at the intermediate operating temperature of 800°C. Unfortunately, total oxide ion conductivity measurements of fully sintered $La_{10}Si_{6-x-0.2}Al_xZn_{0.2}O_{27-\delta}$ ($x = 0.2$ and 0.4) pellets could not be obtained because the pellets are not fully sintered even after heating at the maximum temperature (1600°C) of the furnace, whilst the samples have porous electrolyte nature, but the grain growth is obviously aging at elevated temperature which can be correlated with the conductivity results [66]. Normally, Zn doping in oxides increases the sintering behavior and density of the materials [67]. A wet chemical method using azeotropic distillation was used to densify lanthanum silicate. The particle size was about 10 mm which helps to densify the material [68]. Figure 6 presents the Arrhenius plots of $La_{10}Si_{6-x-0.2}Al_xZn_{0.2}O_{27-\delta}$ ($x = 0.2$ and 0.4) pellets. Straight lines can be drawn from the Arrhenius plots that are well fitted to the

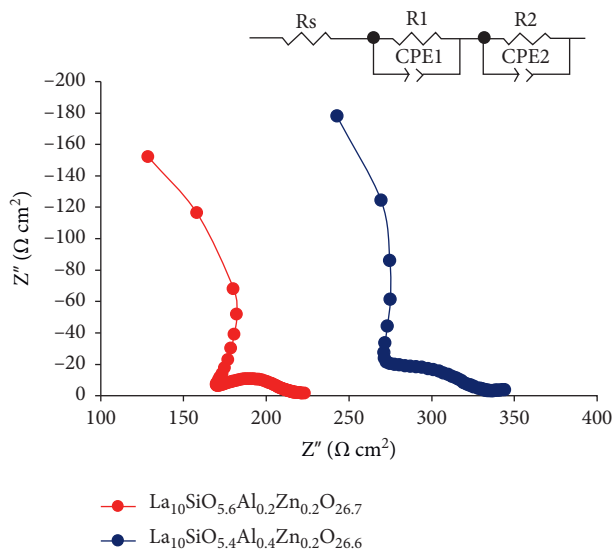

Figure 5: A.C. impedance plots of $La_{10}Si_{5.6}Al_{0.2}Zn_{0.2}O_{26.7}$ (left) and $La_{10}Si_{5.4}Al_{0.4}Zn_{0.2}O_{26.6}$ (right) at intermediate operating temperature of 800°C and the equivalent circuit.

Table 2: Total conductivity of different compositions reported in this work and in the literature.

Sample compositions	500°C (Scm^{-1})	600°C (Scm^{-1})	700°C (Scm^{-1})	800°C (Scm^{-1})	Ref.
$La_{10}Si_{5.4}Al_{0.4}Zn_{0.2}O_{26.6}$	1.35×10^{-4}	5.67×10^{-4}	1.38×10^{-3}	2.08×10^{-3}	This work
$La_{10}Si_{5.6}Al_{0.2}Zn_{0.2}O_{26.7}$	1.61×10^{-4}	7.23×10^{-4}	1.76×10^{-3}	3.24×10^{-3}	This work
$La_{9.67}Si_6O_{26.5}$	0.40×10^{-3}	—	—	7.10×10^{-3}	[41]
$La_{9.533}(Si_{5.4}Al_{0.6})O_{26}$	0.60×10^{-3}	—	—	7.80×10^{-3}	[41]
$La_{9.8}Si_{5.7}Mg_{0.3}O_{26.4}$	—	—	—	7.40×10^{-2}	[45]
$La_{10}Si_{5.8}Mg_{0.2}O_{26.8}$	—	—	—	8.8×10^{-2}	[45]
$La_9BaSi_6O_{26.5}$	—	—	—	11.4×10^{-3}	[43]
$La_9SrSi_6O_{26.5}$	—	—	—	8.7×10^{-3}	[43]
$La_{9.67}Si_5AlO_{26}$	—	—	—	7.9×10^{-3}	[65]

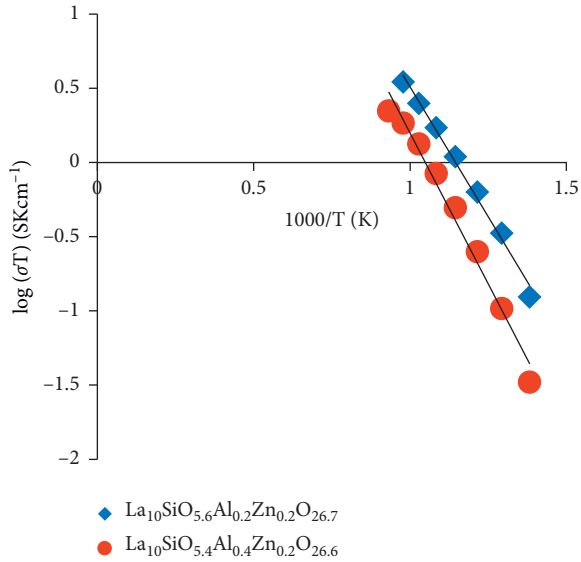

Figure 6: Arrhenius plots of total oxide ion conductivity of $La_{10}Si_{6-x-0.2}Al_xZn_{0.2}O_{27-\delta}$ ($x = 0.2$ and 0.4).

Table 3: Comparison of activation energy E_a and preexponential factor k of $La_{10}Si_{6-x-0.2}Al_xZn_{0.2}O_{27-\delta}$ ($x = 0.2$ and 0.4) with literatures.

	$La_{10}Si_{5.4}Al_{0.4}Zn_{0.2}O_{26.6}$ (this work)	$La_{10}Si_{5.6}Al_{0.2}Zn_{0.2}O_{26.7}$ (this work)	$La_{9.6}Si_{5.7}Mg_{0.3}O_{26.1}$ [44]	$La_{10}(SiO_4)_6O_3$ [39]	$La_{10}Si_6O_{27}$ [70]	$La_{9.50}Si_6O_{26.25}$ [70]
Activation energy, E_a (eV)	0.35	0.30	0.43	0.65 ± 0.1	0.67	0.35
Preexponential factor, k ($Skcm^{-1}$)	18281	10216	—	—	—	—

Arrhenius equation. The fitted lines indicate that the diffusion process of oxide ions is thermally activated [45].

The activation energy described by Arrhenius in 1889 is the minimum amount of energy required to conduct a chemical reaction [69], i.e., as less energy is used, the lower the cost. According to the Meyer–Neldel rule, activation energy is related to the preexponential factor, i.e., with the decrease in activation energy, the preexponential factor will increase and the ionic conductivity is affected by temperature significantly compared to the activation energy. From the slope and the intercept of the linear fit in the Arrhenius plots, the activation energy E_a and preexponential factor k of the materials can be obtained using equation (3). The values of activation energy E_a and preexponential factor k of $La_{10}Si_{6-x-0.2}Al_xZn_{0.2}O_{27-\delta}$ ($x = 0.2$ and 0.4) pellets are compared with another apatite structure in Table 3. $La_{10}Si_{6-x-0.2}Al_xZn_{0.2}O_{27-\delta}$ ($x = 0.2$ and 0.4) apatite materials resulted in a significant improvement on the total oxide ion conductivity at the operating temperature of 800°C. It is noteworthy in this work that we got a large value of preexponential factor which may be explicated a higher coordination number between lanthanum (La) and oxygen (O) [71]. Hence, $La_{10}Si_{6-x-0.2}Al_xZn_{0.2}O_{27-\delta}$ ($x = 0.2$ and 0.4) apatite materials maybe useful as electrolyte materials of SOFCs [65]. Recently, lanthanum silicate-based materials were used to measure power density at intermediate temperature [72, 73].

4. Conclusion

In summary, the apatite-type hexagonal $La_{10}Si_{6-x-0.2}Al_xZn_{0.2}O_{27-\delta}$ ($x = 0.2$ and 0.4) crystals were examined as promising electrolytes for SOFCs. Nonetheless, the operational challenges associated with its high sintering temperature. XRD patterns of the sintered $La_{10}Si_{6-x-0.2}Al_xZn_{0.2}O_{27-\delta}$ ($x = 0.2$ and 0.4) materials revealed the apatite phase with $P6_3/m$ space group with a small amount of impurity. The milling process has reduced most of the large grains into microsize grains closely related to each other, which aids in the formation of the hexagonal apatite structure. $La_{10}Si_{5.6}Al_{0.2}Zn_{0.2}O_{26.7}$ gives the highest total oxide ion conductivity of 3.24×10^{-3} Scm^{-1} at the intermediate operating temperature of 800°C. The activation energy was decreasing with increasing the preexponential factor and the lowest activation energy was 0.30 eV for $La_{10}Si_{5.6}Al_{0.2}Zn_{0.2}O_{26.7}$ which was one of the lowest activation energies among the lanthanum silicate-ion conductors. Thus, the apatite-type $La_{10}Si_{6-x-0.2}Al_xZn_{0.2}O_{27-\delta}$ can be used in SC-SOFCs due to its porous microstructure.

Data Availability

The data used in this study are available on request.

Conflicts of Interest

The authors declare that there are no financial or personal conflicts of interest for this publication.

Acknowledgments

The authors would like to thank the Faculty of Integrated Technologies, Faculty of Science, and Centre for Advanced Material and Energy Sciences at Universiti Brunei Darussalam.

References

[1] M. Beigzadeh, F. Pourfayaz, and M. H. Ahmadi, "Modeling and improvement of solid oxide fuel cell-single effect absorption chiller hybrid system by using nanofluids as heat transporters," *Applied Thermal Engineering*, vol. 166, 2020.

[2] M. Beigzadeh, F. Pourfayaz, M. Ghazvini, and M. H. Ahmadi, "Energy and exergy analyses of solid oxide fuel cell-gas turbine hybrid systems fed by different renewable biofuels: a comparative study," *Journal of Cleaner Production*, vol. 280, 2021.

[3] Z. Wu, P. Zhu, J. Yao et al., "Dynamic modeling and operation strategy of natural gas fueled SOFC-engine hybrid power system with hydrogen addition by metal hydride for vehicle applications," *eTransportation*, vol. 5, 2020.

[4] X. Su, F. Zhang, Y. Yin, B. Tu, and M. Cheng, "Thermodynamic analysis and fuel processing strategies for propane-fueled solid oxide fuel cell," *Energy Conversion and Management*, vol. 204, 2020.

[5] A. M. Abdalla, S. Hossain, O. B. Nisfindy, A. T. Azad, M. Dawood, and A. K. Azad, "Hydrogen production, storage, transportation and key challenges with applications: a review," *Energy Conversion and Management*, vol. 165, pp. 602–627, 2018.

[6] S. Hossain, A. M. Abdalla, S. N. B. Jamain, J. H. Zaini, and A. K. Azad, "A review on proton conducting electrolytes for clean energy and intermediate temperature-solid oxide fuel cells," *Renewable and Sustainable Energy Reviews*, vol. 79, pp. 750–764, 2017.

[7] M. Ahmadi, M. Sadaghiani, F. Pourfayaz et al., "Energy and exergy analyses of a solid oxide fuel cell-gas turbine-organic rankine cycle power plant with liquefied natural gas as heat sink," *Entropy*, vol. 20, no. 7, p. 484, 2018.

[8] M. Beigzadeh, F. Pourfayaz, M. H. Ahmadi, S. M. Pourkiaei, and M. Beigzadeh, "A simplificative approach-based modeling of SOFC power systems fed by natural gas," *Fuel Cells*, vol. 17, no. 6, pp. 843–853, 2017.

[9] N. Mahato, A. Banerjee, A. Gupta, S. Omar, and K. Balani, "Progress in material selection for solid oxide fuel cell technology: a review," *Progress in Materials Science*, vol. 72, pp. 141–337, 2015.

[10] M. S. Reza, A. Ahmed, W. Caesarendra et al., "Acacia holosericea: an invasive species for bio-char, bio-oil, and biogas production," *Bioengineering*, vol. 6, no. 2, p. 33, 2019.

[11] M. S. Reza, S. N. Islam, S. Afroze et al., "Evaluation of the bioenergy potential of invasive *Pennisetum purpureum* through pyrolysis and thermogravimetric analysis," *Energy, Ecology and Environment*, vol. 5, no. 2, pp. 118–133, 2019.

[12] M. S. Reza, C. S. Yun, S. Afroze et al., "Preparation of activated carbon from biomass and its' applications in water and gas purification, a review," *Arab Journal of Basic and Applied Sciences*, vol. 27, no. 1, pp. 208–238, 2020.

[13] M. S. Reza, S. Afroze, M. S. A. Bakar et al., "Biochar characterization of invasive *Pennisetum purpureum* grass: effect of pyrolysis temperature," *Biochar*, vol. 2, no. 2, pp. 239–251, 2020.

[14] J. Hanna, W. Y. Lee, Y. Shi, and A. F. Ghoniem, "Fundamentals of electro- and thermochemistry in the anode of solid-oxide fuel cells with hydrocarbon and syngas fuels," *Progress in Energy and Combustion Science*, vol. 40, no. 1, pp. 74–111, 2014.

[15] S. Afroze, A. Karim, Q. Cheok, S. Eriksson, and A. K. Azad, "Latest development of double perovskite electrode materials for solid oxide fuel cells: a review," *Frontiers in Energy*, vol. 13, no. 4, pp. 770–797, 2019.

[16] H. Q. H. H. Absah, M. S. A. Bakar, J. H. Zaini, A. Azad, and L. C. Ming, "$Bi_2O_3$and $La_{10}Si_6O_{27}$composite electrolyte for enhanced performance in solid oxide fuel cells," *IOP Conference Series: Materials Science and Engineering*, vol. 121, no. 1, 2016.

[17] S. Afroze, M. S. Reza, Q. Cheok, J. Taweekun, and A. K. Azad, "Solid oxide fuel cell (SOFC); A new approach of energy generation during the pandemic COVID-19," *International Journal of Integrated Engineering*, vol. 12, no. 5, pp. 245–256, 2020.

[18] A. K. Azad, A. Kruth, and J. T. S. Irvine, "Influence of atmosphere on redox structure of $BaCe_{0.9}Y_{0.1}O_{2.95}$ - insight from neutron diffraction study," *International Journal of Hydrogen Energy*, vol. 39, no. 24, pp. 12804–12811, 2014.

[19] Z. Zakaria, S. H. Abu Hassan, N. Shaari, A. Z. Yahaya, and Y. Boon Kar, "A review on recent status and challenges of yttria stabilized zirconia modification to lowering the temperature of solid oxide fuel cells operation," *International Journal of Energy Research*, vol. 44, no. 2, pp. 631–650, 2020.

[20] H. Shi, C. Su, R. Ran, J. Cao, and Z. Shao, "Electrolyte materials for intermediate-temperature solid oxide fuel cells," *Progress in Natural Science: Materials International*, vol. 30, no. 6, pp. 764–774, 2020.

[21] A. M. Abdalla, S. Hossain, J. Zhou, P. M. I. Petra, and A. K. Azad, "Synthesis, structural and thermal properties of layered perovskites SmBaMn," *Materials Science Forum*, vol. 889, pp. 195–200, 2017.

[22] S. Hossain, A. M. Abdalla, J. H. Zaini, C. D. Savaniu, J. T. S. Irvine, and A. K. Azad, "Highly dense and novel proton conducting materials for SOFC electrolyte," *International Journal of Hydrogen Energy*, vol. 42, no. 44, pp. 27308–27322, 2017.

[23] A. Afif, J. Zaini, S. M. H. Rahman, S. Eriksson, M. A. Islam, and A. K. Azad, "Scheelite type $Sr_{1-x}Ba_xWO_4$ ($x = 0.1, 0.2, 0.3$) for possible application in solid oxide fuel cell electrolytes," *Scientific Reports*, vol. 9, no. 1, pp. 1–10, 2019.

[24] N. Radenahmad, A. Afif, M. I. Petra, S. M. H. Rahman, S. Eriksson, and A. K. Azad, "High conductivity and high density proton conducting $Ba_{1-x}Sr_xCe_{0.5}Zr_{0.35}Y_{0.1}Sm_{0.05}O_{3-\delta}$ ($x = 0.5, 0.7, 0.9, 1.0$) perovskites for IT-SOFC," *International Journal of Hydrogen Energy*, vol. 41, no. 27, pp. 11832–11841, 2016.

[25] A. Afif, N. Radenahmad, C. M. Lim et al., "Structural study and proton conductivity in $BaCe_{0.7}Zr_{0.25-x}Y_xZn_{0.05}O_3$($x$ = 0.05, 0.1, 0.15, 0.2 & 0.25)," *International Journal of Hydrogen Energy*, vol. 41, no. 27, pp. 11823–11831, 2016.

[26] M. Naeem Khan, A. K. Azad, C. D. Savaniu, P. Hing, and J. T. S. Irvine, "Robust doped $BaCeO_{3-\delta}$ electrolyte for IT-SOFCs," *Ionics (Kiel)*, vol. 23, no. 9, pp. 2387–2396, 2017.

[27] N. Radenahmad, A. Afif, A. M. Abdalla et al., "A new high-performance proton-conducting electrolyte for next-generation solid oxide fuel cells," *Energy Technology*, vol. 8, no. 9, 2020.

[28] S. Nakayama, Y. Higuchi, M. Sugawara, A. Makiya, K. Uematsu, and M. Sakamoto, "Fabrication of c-axis-oriented apatite-type polycrystalline $La_{10}Si_6O_{27}$ ceramic and its anisotropic oxide ionic conductivity," *Ceramics International*, vol. 40, no. 1, pp. 1221–1224, 2014.

[29] W. Liu, S. Yamaguchi, T. Tsuchiya, S. Miyoshi, K. Kobayashi, and W. Pan, "Sol-gel synthesis and ionic conductivity of oxyapatite-type $La_{9.33+x}Si_6O_{26+1.5x}$," *Journal of Power Sources*, vol. 235, pp. 62–66, 2013.

[30] E. Rodríguez-Reyna, A. F. Fuentes, M. MacZka, J. Hanuza, K. Boulahya, and U. Amador, "Facile synthesis, characterization and electrical properties of apatite-type lanthanum germanates," *Solid State Sciences*, vol. 8, no. 2, pp. 168–177, 2006.

[31] J. M. Porras-Vázquez, E. R. Losilla, M. A. G. Aranda, and I. Santacruz, "Oxy-apatite reaction sintering of colloidal and classic ceramic processed powders," *Ceramics International*, vol. 38, no. 3, pp. 1851–1858, 2012.

[32] A. L. Shaula, V. V. Kharton, and F. M. B. Marques, "Oxygen ionic and electronic transport in apatite-type $La_{10-x}(Si,Al)_6O_{26\pm\delta}$," *Journal of Solid State Chemistry*, vol. 178, no. 6, pp. 2050–2061, 2005.

[33] R. Hu, R. Ding, J. Chen, J. Hu, and Y. Zhang, "Preparation and catalytic activities of the novel double perovskite-type oxide La_2CuNiO_6 for methane combustion," *Catalysis Communications*, vol. 21, pp. 38–41, 2012.

[34] D. Marrero-López, M. C. Martín-Sedeño, J. Peña-Martínez et al., "Evaluation of apatite silicates as solid oxide fuel cell electrolytes," *Journal of Power Sources*, vol. 195, no. 9, pp. 2496–2506, 2010.

[35] T. Nakao, A. Mineshige, M. Kobune, T. Yazawa, and H. Yoshioka, "Chemical stability of $La_{10}Si_6O_{27}$ and its application to electrolytes for solid oxide fuel cells," *Solid State Ionics*, vol. 179, no. 27-32, pp. 1567–1569, 2008.

[36] X. G. Cao and S. P. Jiang, "Sinterability and conductivity of barium doped aluminium lanthanum oxyapatite $La_{9.5}Ba_{0.5}Si_{5.5}Al_{0.5}O_{26.5}$ electrolyte of solid oxide fuel cells," *Journal of Alloys and Compounds*, vol. 523, pp. 127–133, 2012.

[37] H. Q. H. H. Absah, A. H. Karim, M. S. Abu Bakar, L. C. Ming, and A. K. Azad, "Synthesis of $La_{10}Si_{6-2x}Bi_{2x}O_{27-x}$ as possible electrolyte materials for solid oxide fuel cells," *Materials Science Forum*, vol. 889, pp. 173–177, 2017.

[38] S. P. Jiang, L. Zhang, H. Q. He, R. K. Yap, and Y. Xiang, "Synthesis and characterization of lanthanum silicate apatite by gel-casting route as electrolytes for solid oxide fuel cells," *Journal of Power Sources*, vol. 189, no. 2, pp. 972–981, 2009.

[39] S. Tao and J. T. S. Irvine, "Preparation and characterisation of apatite-type lanthanum silicates by a sol-gel process," *Materials Research Bulletin*, vol. 36, no. 7-8, pp. 1245–1258, 2001.

[40] D. D. Y. Setsoafia, P. Hing, S. C. Jung, A. K. Azad, and C. M. Lim, "Sol-gel synthesis and characterization of Zn^{2+} and Mg^{2+} doped $La_{10}Si_6O_{27}$ electrolytes for solid oxide fuel cells," *Solid State Sciences*, vol. 48, pp. 163–170, 2015.

[41] H. Yoshioka, "Enhancement of ionic conductivity of apatite-type lanthanum silicates doped with cations," *Journal of the American Ceramic Society*, vol. 90, no. 10, pp. 3099–3105, 2007.

[42] S. Beaudet-Savignat, A. Vincent, S. Lambert, and F. Gervais, "Oxide ion conduction in Ba, Ca and Sr doped apatite-type lanthanum silicates," *Journal of Materials Chemistry*, vol. 17, no. 20, pp. 2078–2087, 2007.

[43] A. Vincent, S. B. Savignat, and F. Gervais, "Elaboration and ionic conduction of apatite-type lanthanum silicates doped with Ba, $La_{10-x}Ba_x(SiO_4)_6O_{3-x/2}$ with x=0.25–2," *Journal of the European Ceramic Society*, vol. 27, no. 2-3, pp. 1187–1192, 2007.

[44] H. Yoshioka and S. Tanase, "Magnesium doped lanthanum silicate with apatite-type structure as an electrolyte for intermediate temperature solid oxide fuel cells," *Solid State Ionics*, vol. 176, no. 31-34, pp. 2395–2398, 2005.

[45] H. Yoshioka, Y. Nojiri, and S. Tanase, "Ionic conductivity and fuel cell properties of apatite-type lanthanum silicates doped with Mg and containing excess oxide ions," *Solid State Ionics*, vol. 179, no. 38, pp. 2165–2169, 2008.

[46] J. E. H. Sansom, E. Kendrick, J. R. Tolchard, M. S. Islam, and P. R. Slater, "A comparison of the effect of rare earth vs. Si site doping on the conductivities of apatite-type rare earth silicates," *Journal of Solid State Electrochemistry*, vol. 10, no. 8, pp. 562–568, 2006.

[47] L. Malavasi, C. A. J. Fisher, and M. S. Islam, "Oxide-ion and proton conducting electrolyte materials for clean energy applications: structural and mechanistic features," *Chemical Society Reviews*, vol. 39, no. 11, pp. 4370–4387, 2010.

[48] M. Kuhn and T. Napporn, "Single-chamber solid oxide fuel cell technology-from its origins to today's state of the art," *Energies*, vol. 3, no. 1, pp. 57–134, 2010.

[49] M. Yano, A. Tomita, M. Sano, and T. Hibino, "Recent advances in single-chamber solid oxide fuel cells: a review," *Solid State Ionics*, vol. 177, no. 39-40, pp. 3351–3359, 2007.

[50] P. P. Mardilovich, Y. She, Y. H. Ma, and M.-H. Rei, "Defect-free palladium membranes on porous stainless-steel support," *AIChE Journal*, vol. 44, no. 2, pp. 310–322, 1998.

[51] S. Afroze, N. Torino, P. F. Henry, M. Sumon Reza, Q. Cheok, and A. K. Azad, "Insight of novel layered perovskite $PrSrMn_2O_{5+\delta}$: a neutron powder diffraction study," *Materials Letters*, vol. 261, 2020.

[52] S. Afroze, N. Torino, P. F. Henry, M. S. Reza, Q. Cheok, and A. K. Azad, "Neutron and X-ray powder diffraction data to determine the structural properties of novel layered perovskite $PrSrMn_2O_{5+\delta}$," *Data in Brief*, vol. 29, 2020.

[53] S. Afroze, N. Torino, M. S. Reza et al., "Structure-conductivity relationship of $PrBaMnMoO_{6-\delta}$ through in-situ measurements: a neutron diffraction study," *Ceramics International*, vol. 47, no. 1, p. 541, 2020.

[54] X. Xu, Y. Xie, S. Ni, A. K. Azad, and T. Cao, "Photocatalytic H_2 production from spinels $ZnGa_2$-CrO_4 ($0 \le x \le 2$) solid solutions," *Journal of Solid State Chemistry*, vol. 230, pp. 95–101, 2015.

[55] A. K. M. Zakaria, M. A. Asgar, S.-G. Eriksson et al., "Preparation of Zn substituted Ni-Fe-Cr ferrites and study of the crystal structure by neutron diffraction," *Materials Letters*, vol. 57, no. 26-27, pp. 4243–4250, 2003.

[56] S. Afroze, D. Yilmaz, M. S. Reza et al., "Investigation of structural and thermal evolution in novel layered perovskite $NdSrMn_2O_{5+\delta}$ via neutron powder diffraction and thermogravimetric analysis," *International Journal of Chemical Engineering*, vol. 2020, Article ID 6642187, 7 pages, 2020.

[57] JEOL Ltd, A Guide to Scanning Microscope Observation published by, JEOL Ltd., Akishima, Tokyo, Japan, https://www.jeol.co.jp/en/applications/pdf/sm/844_en.pdf.

[58] Y. Zhao, L. Dai, Z. He, L. Wang, and J. Cao, "Synthesis and characterization of Ba^{2+} and W^{6+} co-doped apatite-type lanthanum silicate electrolytes," *Ceramics International*, vol. 46, no. 4, pp. 5420–5429, 2020.

[59] K. Fukuda, T. Iwata, and E. Champion, "Crystal structure of lanthanum oxyorthosilicate, La_2SiO_5," *Powder Diffraction*, vol. 21, no. 4, pp. 300–303, 2006.

[60] Y. Zhang, Z. Su, A. K. Azad, W. Zhou, and J. T. S. Irvine, "Directly imaging interstitial oxygen in silicate apatite," *Advanced Energy Materials*, vol. 2, no. 3, pp. 316–321, 2012.

[61] T. Yang, H. Zhao, M. Fang, K. Świerczek, J. Wang, and Z. Du, "A new family of Cu-doped lanthanum silicate apatites as electrolyte materials for SOFCs: synthesis, structural and electrical properties," *Journal of the European Ceramic Society*, vol. 39, no. 2-3, pp. 424–431, 2018.

[62] M. Irshad, Q. u. Ain, K. Siraj et al., "Evaluation of $BaZr_{0.8}X_{0.2}$ (X= Y, Gd, Sm) proton conducting electrolytes sintered at low temperature for IT-SOFC synthesized by cost effective combustion method," *Journal of Alloys and Compounds*, vol. 815, p. 152389, 2020.

[63] S. Afroze, A. M. Abdalla, N. Radenahmad, Q. C. Hoon Nam, and A. K. Azad, "Synthesis, structural and thermal properties of double perovskite $NdSrMn_2O_6$ as potential anode materials for solid oxide fuel cells," in *Proceedings of the 7th Brunei International Conference on Engineering and Technology 2018 (BICET 2018)*, vol. 2018, Bandar Seri Begawan, Brunei, November 2018.

[64] I. Yasuda, Y. Matsuzaki, T. Yamakawa, and T. Koyama, "Electrical conductivity and mechanical properties of alumina-dispersed doped lanthanum gallates," *Solid State Ionics*, vol. 135, no. 1-4, pp. 381–388, 2000.

[65] H. Li, S. Zhang, S. Zhou, and X. Cao, "Chemical bond characteristics, thermal expansion property and compressibility of AR_2O_4 (A=Ca, Sr, Ba; R=rare earths)," *Materials Chemistry and Physics*, vol. 114, no. 1, pp. 451–455, 2009.

[66] X. Ding, G. Hua, D. Ding, W. Zhu, and H. Wang, "Enhanced ionic conductivity of apatite-type lanthanum silicate electrolyte for IT-SOFCs through copper doping," *Journal of Power Sources*, vol. 306, pp. 630–635, 2016.

[67] A. Azad and J. Irvine, "High density and low temperature sintered proton conductor $BaCe_{0.5}Zr_{0.35}Sc_{0.1}Zn_{0.05}O_{3-\delta}$," *Solid State Ionics*, vol. 179, no. 19-20, pp. 678–682, 2008.

[68] H.-C. Yao, J.-S. Wang, D.-G. Hu, J.-F. Li, X.-R. Lu, and Z.-J. Li, "New approach to develop dense lanthanum silicate oxyapatite sintered ceramics with high conductivity," *Solid State Ionics*, vol. 181, no. 1-2, pp. 41–47, 2010.

[69] N. S. Khan, Z. Shah, M. Shutaywi, P. Kumam, and P. Thounthong, "A comprehensive study to the assessment of Arrhenius activation energy and binary chemical reaction in swirling flow," *Scientific Reports*, vol. 10, no. 1, p. 7868, 2020.

[70] J. Chen, J. Huang, X. Li et al., "Plasma-sprayed coating of an apatite-type lanthanum silicate electrolyte for intermediate temperature solid oxide fuel cells (IT-SOFCs)," *Plasma Science and Technology*, vol. 15, no. 7, pp. 673–676, 2013.

[71] N. Takeda, Y. Itagaki, and Y. Sadaoka, "Relationship between pre-exponential factor and activation energy of conductivity in sintered $ln_{9.33+x/3}Si_{6-x}M_xO_{26}$ (Ln=La, Nd, Sm, M=Al, Gd) with apatite-like structure," *Journal of the Ceramic Society of Japan*, vol. 115, no. 1346, pp. 643–647, 2007.

[72] A. Mineshige, A. Saito, M. Kobayashi et al., "Lanthanum silicate-based layered electrolyte for intermediate-temperature fuel cell application," *Journal of Power Sources*, vol. 475, p. 228543, 2020.

[73] J. R. Tolchard, J. E. H. Sansom, M. S. Islam, and P. R. Slater, "Structural studies of apatite-type oxide ion conductors doped with cobalt," *Dalton Transactions*, vol. 20, no. 7, pp. 1273–1280, 2005.

Hindawi
International Journal of Chemical Engineering
Volume 2020, Article ID 6642187, 7 pages
https://doi.org/10.1155/2020/6642187

Research Article

Investigation of Structural and Thermal Evolution in Novel Layered Perovskite $NdSrMn_2O_{5+\delta}$ via Neutron Powder Diffraction and Thermogravimetric Analysis

Shammya Afroze,[1,2] Duygu Yilmaz,[2] Md Sumon Reza,[1] Paul F. Henry,[3,4] Quentin Cheok,[1] Juliana H Zaini,[1] Abul K. Azad,[1] Alibek Issakhov,[5] and Milad Sadeghzadeh[6]

[1]*Faculty of Integrated Technologies, Universiti Brunei Darussalam, Jalan Tungku Link, Gadong, BE 1410, Bandar Seri Begawan, Brunei Darussalam*
[2]*Department of Chemistry and Chemical Engineering, Chalmers University of Technology, SE 412 96, Gothenburg, Sweden*
[3]*ISIS Pulsed Neutron & Muon Facility, Rutherford Appleton Laboratory, Harwell Campus, OX11 0QX, Didcot, UK*
[4]*Department of Chemistry–Ångström Laboratory Inorganic Chemistry, Uppsala University, 751 21 Uppsala, Sweden*
[5]*Faculty of Mechanics and Mathematics, Department of Mathematical and Computer Modelling, Al-Farabi Kazakh National University, Almaty, Kazakhstan*
[6]*Department of Renewable Energy and Environmental Engineering, University of Tehran, Tehran, Iran*

Correspondence should be addressed to Abul K. Azad; abul.azad@ubd.edu.bn and Milad Sadeghzadeh; milad.sadeghzadeh@gmail.com

Received 17 October 2020; Revised 28 October 2020; Accepted 16 November 2020; Published 29 November 2020

Academic Editor: Mohammad Hossein Ahmadi

Neutron diffraction is one of the best methods for structural analysis of a complex, layered perovskite material with low symmetry by accurately detecting the oxygen positions through octahedral tilting. In this research, the crystal structure of $NdSrMn_2O_{5+\delta}$ was identified through X-ray diffraction (XRD) and neutron powder diffraction (NPD) at room temperature (RT), which indicated the formation of a layered structure in orthorhombic symmetry in the *Pmmm* (no. 47) space group. Rietveld refinement of the neutron diffraction data has confirmed the orthorhombic symmetry with unit cell parameters ($a = 3.8367$ (1) Å, $b = 3.8643$ (2) Å, and $c = 7.7126$ (1) Å), atomic positions, and oxygen occupancy. Thermogravimetric analysis revealed the total weight loss of about 0.10% for 20–950°C temperature, which occurred mainly to create oxygen vacancies at high temperatures. Rietveld analyses concurred with the XRD and neutron data allowing correlation of occupancy factors of the oxygen sites.

1. Introduction

The perovskite materials are used widely in solid oxide fuel cells (SOFCs) due to its diversity in chemical compositions. Ideal cubic symmetrical perovskite oxides have the general formula ABO_3 [1], where A and B indicate A-site and B-site cations and O is the anion [2]. Perovskite oxides containing excess oxygen due to interstitial oxygen atoms are unstable thermodynamically [3, 4]. Since oxygen has a high electronegativity, it will always attract electrons from heated-site and B-site cations and make them mixed-valence state for stability. As a result, research is being concentrated on perovskite oxides which have oxygen deficiency, and this deficiency can be created by manipulating the cationic and anionic stoichiometry of ABO_3 [5]. In recent times, the layered perovskites have attracted researchers because of their promising properties in energy sectors [6–8]. Rare-earth perovskites, such as $PrBaMn_2O_5$ and $NdBaMn_2O_5$, exhibited excellent redox stability (this implies that more easily reduced perovskite exhibits higher catalytic activity) and tolerance to coking and sulfur contamination from fuels [9]. Besides, some manganese-based layered perovskite can

be used as oxygen storage materials in solid oxide fuel cells (SOFCs) [10] and solid oxide electrolyzer cells (SOECs) due to their electron-conductive nature [11–13]. Some layered-type perovskites used as electrodes in SOFCs [14–18] fueled through hydrogen or other syngas [19–22] have also shown promising results.

The structural distortion is our core consideration as it affects the physical and electrochemical properties of the perovskite-type oxides [23–25]. Neutron diffraction is a robust technique that can determine complex crystal structure, oxygen stoichiometry, and oxygen vacancy ordering. It is noteworthy that the neutron is scattered from the nuclei of the atoms allowing for the formation of different isotopes of the same atom and could detect light atoms masked by the heavy atoms [26]. The Bragg reflections of the powder pattern with a long Q-range can easily be detected. Many efforts have been dedicated to enriching the performance of layered perovskite by substituting various cations, especially Mn-doped rare-earth perovskite. As an anode for SOFCs, $(PrBa)_{0.95}(Fe_{0.9}Mo_{0.1})_2O_{5+\delta}$ (PBFM) demonstrated a high power density of 1.72 W·cm^{-2} at 800°C (as reported in [27]), whereas the composition $SmBaCo_{0.5}Mn_{1.5}O_{5+\delta}$ demonstrated a power density of 377 mW/cm^2 and $SmBaMn_2O_{5+\delta}$ exhibited high power density of 782 mW·cm^{-2} at 900°C as an electrode [16, 28].

The synthesis of a novel material was elaborately discussed, and the results of high-resolution neutron powder diffraction (NPD) studies were observed on the crystallized sample in this work. We report the complete structural data of these materials and describe the thermal properties from thermogravimetric analysis.

2. Materials and Methods

The solid-state synthesis technique [18, 29–33] was applied to developing $NdSrMn_2O_{5+\delta}$. Oxide powders of Nd_2O_3 (≥99.90%, Sigma-Aldrich), $SrCO_3$ (≥99.90%, Aldrich), and MnO (≥99.50%, Aldrich) were weighed according to their stoichiometric ratios and ground with the aid of a mortar and pestle using ethanol as a reagent [34]. The powders were calcined at 1000°C for 10 hours after drying. The powders were pressed into pellets and sintered at 1200°C for 12 hours with 5°C·min^{-1} heating and cooling rate with intermediate grinding. Subsequently, the pellets were reground and resintered at 1400°C for another 12 hours. The whole synthesis process was operated under an Argon (Ar) atmosphere with a gas flow rate of 40 ml·min^{-1}. X-ray powder diffraction (XRD) and neutron powder diffraction (NPD) were used to analyze the crystal structure of $NdSrMn_2O_{5+\delta}$ material.

The phase structure was first determined by XRD using a Bruker axs-D8 Advance diffractometer. Data were collected in the 2θ range from 10° to 79.995° with increments of 0.02° per second. The Rietveld refinement procedure was used to analyze the XRD data [35] using the Fullprof software [36]. A polynomial function (6-coefficient) was set for the background, and the pseudo-Voigt function was used to model the peak shapes.

Neutron powder diffraction data were collected at room temperature (RT) with the Polaris diffractometer (medium-resolution powder diffractometer at a high intensity) at the ISIS Neutron & Muon Source, UK [37, 38]. The time-of-flight (TOF) powder diffraction data were analyzed using GSAS-II [39] software. This material is debuted under the *Pmmm* space group through the Rietveld analysis of the high-resolution NPD data; a layered perovskite structure was formed. The Rietveld analysis used standard parameters for the refinement: a shifted Chebyshev series as background as instigated in GSAS software, zero shift, scale factor, profile parameters (type 3 in GSAS), cell parameters, atomic coordinates, site-occupancy factor (SOF), and atomic displacement factors (ADP).

To perform thermogravimetric analysis (TGA), a Netzsch-Gerätebau GmbH-STA 409 PC Luxx Simultaneous Thermal Analyzer was used to perceive the weight change with increasing temperature under flowing nitrogen. 99.51 mg of $NdSrMn_2O_{5+\delta}$ powder was placed in a ceramic crucible (Al_2O_3 DSC/TG pan) and heated from 20 to 950°C at a rate of 5°C·min^{-1} under 20 ml·min^{-1} of N_2 flow. An isothermal hold for 1 hour removed absorbed species before cooling. The process was then repeated to ensure complete desorption of any contaminants. Upon complete desorption, N_2 flow was substituted for airflow, and the mass change were recorded until equilibrium was reached.

3. Results and Discussion

Solid-state reaction methods have been used to prepare the layered perovskite $NdSrMn_2O_{5+\delta}$. This layered perovskite is challenging to develop in a pure form, but the single-phase was obtained. Our synthesis method was also different from the method used to obtain $NdBaMn_2O_{5+\delta}$ [40] but similar to the synthesis process for $PrSrMn_2O_{5+\delta}$ [30]. Figure 1 shows the XRD pattern for $NdSrMn_2O_{5+\delta}$ sintered at 1400°C under Ar atmosphere. Some extra small peaks could not be indexed with the basic unit cell pattern. But, most of the peaks in Figure 1 can be indexed to an orthorhombic unit cell. The crystalline structure of this material was determined as ceramic through the XRD pattern. The XRD for the sample was measured at room temperature.

Fundamental understanding of the structure of the $NdSrMn_2O_{5+\delta}$ sample was investigated by neutron powder diffraction at room temperature. Oxygen vacancies are created in the material, which can balance the total charge. The single-phase orthorhombic structure was obtained from neutron diffraction with the space group, *Pmmm*. Rietveld refinement of room-temperature NPD data (Figure 2) revealed that $NdSrMn_2O_{5+\delta}$ achieved cell parameters $a = 3.8367$ (1) Å, $b = 3.8643$ (2) Å, and $c = 7.7126$ (1) Å with dimensions $a_p \times a_p \times 2a_p$ as observed in $NdBaCo_{2-x}Mn_xO_{5+\delta}$ [12]. Bank 2 (up to 7 Å) NPD data were analyzed via Rietveld refinement. The space groups, refinement factors (R-factors), and cell parameters are listed in Table 1, and atomic positions, Wyckoff positions, and isotropic temperature factors are listed Table 2, respectively. In Table 1, the other layered perovskite structures were compared with the present work.

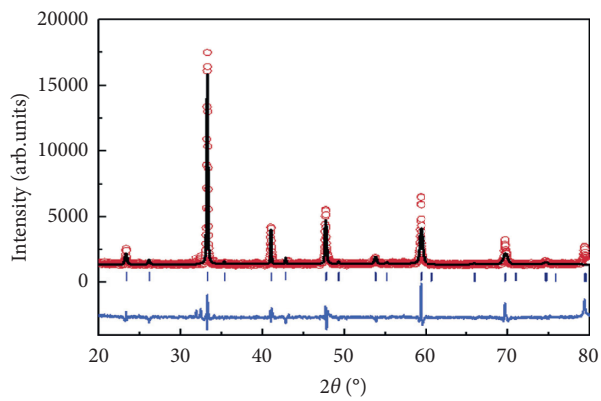

Figure 1: Rietveld refinement pattern of $NdSrMn_2O_{5+\delta}$ for XRD.

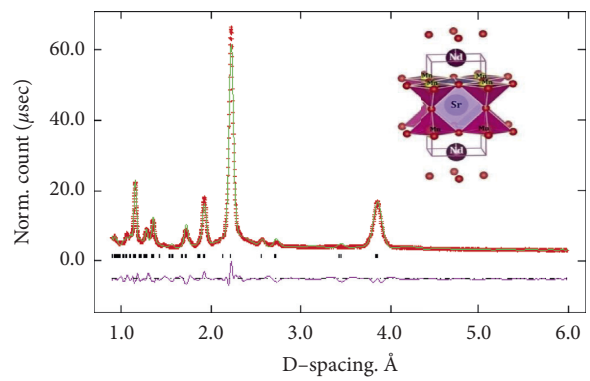

Figure 2: Rietveld refinement profile of $NdSrMn_2O_{5+\delta}$ at room temperature with 3D polyhedral representation. The red line depicts the original data, the continuous green line depicts the calculated profile data, and the purple bottom line depicts the difference.

Table 1: Comparison of the results obtained from the Rietveld analysis of NPD data for $NdSrMn_2O_{5+\delta}$ at RT (space group, *Pmmm*) with other data from the literature.

Parameters	$NdSrMn_2O_{5+\delta}$ at RT	$NdBaMn_2O_{5+\delta}$ at 25°C*	$YBaMn_2O_5$ at 25°C**	$PrSrMn_2O_{5+\delta}$ at RT***
Structure model	Orthorhombic	Tetragonal	Tetragonal	Orthorhombic
Space group	*Pmmm*	*P4/nmm*	P4/mmm	*Pmmm*
Volume (Å^3)	416.8110	—	—	480.9290
R-factors				
R_f (%)	5.50	—	—	—
R_p (%)	4.87	2.21	—	—
R_{wp} (%)	6.86	—	6.00	—
Cell parameters				
a (Å)	3.8367 (1)	5.6140 (1)	3.9186 (2)	3.8906 (1)
b (Å)	3.8643 (2)	5.6140 (1)	3.9186 (2)	3.8227 (1)
c (Å)	7.7126 (1)	7.7430 (2)	7.6540 (5)	7.6846 (2)

*$NdBaMn_2O_{5+\delta}$ [41], **$YBaMn_2O_5$ [42], ***$PrSrMn_2O_{5+\delta}$ [30].

The oxygen occupation was fixed at 1 at three oxygen sites for the space group *Pmmm*, O1, O2, and O3, repectively. These three sites remained locked in the Rietveld model refinement to detect the significant eccentricity from unity. No significant changes were found for three sites. U_{iso} as the thermal vibration parameters for Nd, Sr, and Mn were refined isotropically. These sites were set isotropically to get a standard deviation. Atomic displacement parameters (ADP) and the site-occupancy factors (SOF) correlated with each other. As a result, they were unable to be refined simultaneously. DIFA (a small correction in GSAS software to allow a reflection in the expected time-of-flight peak shifts due to sampling absorption), absorption, and scaling parameters were constrained in this case. The isotropic thermal

Table 2: List of Wyckoff positions, atomic positions, and isotropic temperature factors for $NdSrMn_2O_{5+\delta}$ (space group, *Pmmm*) from neutron diffraction data at RT.

Atoms	Wyckoff positions	x	y	z	U_{iso}
Nd	1f	0.5000	0.5000	0.0000	0.0231 (1)
Sr	1h	0.5000	0.5000	0.5000	0.0172 (1)
Mn	2q	0.0000	0.0000	0.7556	0.0025 (2)
O1	2r	0.0000	0.5000	0.2438	0.0417 (1)
O2	2s	0.5000	0.0000	0.2478	0.0350 (3)
O3	1c	0.0000	0.0000	0.5000	0.0166 (1)

vibration parameters (U_{iso}) also remained constrained in each phase. The average B-O bond lengths at room temperature can be compared to the calculated ionic radii by Shannon [43], where <Mn-O> is 1.9218 (6) Å (calc. 2.08 Å). Main bond distances and their average distances are tabulated in Table 3.

The surface morphology exhibits well-connected, large grains showing visible grain growth with an orthorhombic form. There were no secondary phases found at the grain boundary region in the $NdSrMn_2O_{5+\delta}$ sample. The grains were approximately 10 μm in size for the sample. The porous morphology (Figure 3) depicted that this material can be used as an electrode for fuel cells, the pores will assist the conduction of electrons, as well as allow fuel to pass easily through the structure [44].

An inert atmosphere is needed during the thermogravimetric experiment to prevent oxidation of the sample during thermal treatment. A vacuum environment was created inside the TGA-differential scanning calorimetry (DSC) chamber to ensure an utterly anoxic environment for the analysis. A small amount of the sample $NdSrMn_2O_{5+\delta}$ was taken for thermogravimetric analysis- (TGA-) differential scanning calorimetry (DSC) under a nitrogen environment. TGA showed that oxidation occurred at 200°C while heating in a single gradation (Figure 3) including weight loss with 1 oxygen atom in the formula unit. A small amount of weight loss was observed from 20°C to 950°C in the TGA-DSC curve in N_2 atmosphere. But, there no phase transition occurred which is seen in the DSC curve as there is no exo- or endothermic peaks observed in Figure 3 [45]. The weight loss occurred due to evaporation of the moisture [46], formation of oxygen vacancy, and valence state of cations [3]. In the first step (200°C–500°C), the weight loss was high due to the moisture evaporation [47], and the decline in this region was about 0.084%. Above 500°C, the weight loss was less because all the organic compounds and all other elements end up in this step and the sample behaves as a thermally stable material [48–53]; from 500°C to 950°C, the weight loss was approximately 0.016%. The total weight loss observed was about 0.10% for a temperature range between 20 and 950°C which is comparable with other perovskite materials; $SmBaMn_2O_{5+\delta}$ (0.036%) [54] and $PrSrMn_2O_{5+\delta}$ [30]. The oxygen content of the equilibrium stage decreases with temperature leading to oxygen vacancy formation during TGA-DSC. Table 4 shows that the calculated oxygen occupancy values from TGA are very close to the calculated values from Rietveld refinement. From Table 4, we can see

Table 3: Leading bond distances (Å) ($d \leq 6$ Å) for orthorhombic $NdSrMn_2O_{5+\delta}$ determined from NPD data at room temperature (RT).

Parameters	Bond length (Å)
Nd-O1 (×4)	2.6943 (4)
Nd-O2 (×4)	2.7044 (4)
<Nd-O>	2.6993 (5)
Sr-O1 (×4)	2.7614 (5)
Sr-O2 (×4)	2.7322 (4)
Sr-O3 (×4)	2.7233 (4)
<Sr-O>	2.7389 (6)
Mn-O1 (×4)	1.9200 (4)
Mn-O2 (×4)	1.9325 (4)
Mn-O3 (×4)	1.9131 (5)
<Mn-O>	1.9218 (6)

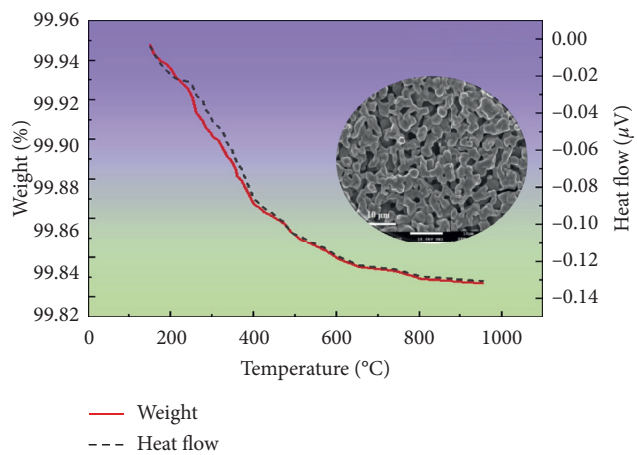

Figure 3: TGA plot of $NdSrMn_2O_{5+\delta}$ on heating from 20°C to 950°C. Single-phase SEM morphology of $NdSrMn_2O_{5+\delta}$ inserted.

that due to the fewer changes in oxygen occupancy in the $NdSrMn_2O_{5+\delta}$ crystal powder, a minimal weight loss has been observed which is close to or less than other layered structures from the literature that are comparable.

The crystal structure of $NdSrMn_2O_{5+\delta}$ is an example of layered orthorhombic symmetry, where both B-cations occupy the perovskite-like corner-shared octahedral (MnO_1 and MnO_2) sites. In this study, we evaluated the structural and thermal characteristics. According to these characterizations, we obtained a good result due to its high porosity, stable structure, and sufficient oxygen deficiency in comparison to similar types of layered perovskites. For $NdSrMn_2O_{5+\delta}$, the Rietveld analysis indicates that all oxygen vacancies occur in the O1 and O2 sites. The volume of this $NdSrMn_2O_{5+\delta}$ material is not so large without any long-range ordering in B-site which indicates an oxygen-deficient layered perovskite oxide. During TGA-DSC, when the heating starts, the weight loss was mainly observed from 200 to 950°C on account of increasing oxygen deficiency and thermally stable [55] due to its minimal amount of weight loss. Also, similar rare-earth layered perovskite has already given a promising result with the same space group for IT-

Table 4: Comparison of TGA results for $NdSrMn_2O_{5+\delta}$ and perovskite structures in the literature.

Compositions	Temperature (°C)	Oxygen occupancy from Rietveld refinement	Weight change (% TG)	Calculated oxygen occupancy from TGA	Ref.
$NdSrMn_2O_{5+\delta}$	20–950	5.3829	0.1005	5.3994	This study
$SmBaMn_2O_{5+\delta}$	Up to 1000	—	0.0220	—	[54]
$PrBaMn_2O_{5+\delta}$	25–800	—	—	—	[25]
$PrSrMn_2O_{5+\delta}$	20–1000	—	0.3600		[30]

SOFC [56]. These types of layered perovskites have recently gained a great deal of attention for SOFC anode materials because of their unusually high oxygen transport kinetics rate [57, 58]. It is established that the layered perovskite performs well for fuel cells reported by Abdalla et al. [40, 54].

4. Conclusions

Terminally, the solid-state synthesis method was used to prepare this single-phase novel, layered perovskite $NdSrMn_2O_{5+\delta}$. XRD, NPD, and TGA-DSC analyses were used to determine structural and thermal properties. Both XRD and NPD data confirmed that the sample crystallizes in orthorhombic symmetry with the space group, *Pmmm* via Rietveld analysis. The structural features of this orthorhombic structure were measured by the action of flowing nitrogen (N_2) with temperature and time, evidenced by a minimal weight loss (0.1%), which may be the weight loss attributed to the oxygen vacancy formation or a decrease in oxygen content. The minimal weight loss occurred in the TGA-DSC results, mainly for the fewer variations in oxygen occupancy in the $NdSrMn_2O_{5+\delta}$ crystal, whose value is closer to the results of oxygen occupancy in neutron refinement analysis. The development of layered perovskite remains an appealing research topic, and promising technology has emerged to improve SOFCs with further electrochemical experiments.

Nomenclature

δ:	Oxygen nonstoichiometry
U_{iso}:	Thermal vibrational parameters
R_p, R_{wp}, and R_f:	Residual factors or *R*-factors
SOFC:	Solid oxide fuel cell
SOEC:	Solid oxide electrolyzer cell
XRD:	X-ray powder diffraction
NPD:	Neutron powder diffraction
RT:	Room temperature
TOF:	Time of flight
SOF:	Site-occupancy factor
ADP:	Atomic displacement factors
TGA:	Thermogravimetric analysis
DSC:	Differential scanning calorimetry.

Data Availability

The data used to support the findings of this study are included within the article.

Conflicts of Interest

The authors declare that they do not have any conflicts of interest.

Acknowledgments

The author Shammya Afroze is grateful to Universiti Brunei Darussalam for awarding her by UBD Graduate Scholarship (UGS). The author is especially indebted to late Professor Sten G. Eriksson from Chalmers University of Technology, Sweden. The ISIS Neutron and Muon Facility, UK, is greatly acknowledged for its scheduled beam-time (RB1810638, DOI: https://doi.org/10.5286/ISIS.E.RB1810638).

References

[1] N. Tien Thao and L. T. Son, "Production of cobalt-copper from partial reduction of La(Co, Cu)O_3 perovskites for CO hydrogenation," *Journal of Science: Advanced Materials and Devices*, vol. 1, no. 3, pp. 337–342, 2016.

[2] S. Feraru, P. Samoila, A. I. Borhan, M. Ignat, A. R. Iordan, and M. N. Palamaru, "Synthesis, characterization of double perovskite Ca_2MSbO_6 (M=Dy, Fe, Cr, Al) materials via sol-gel auto-combustion and their catalytic properties," *Materials Characterization*, vol. 84, pp. 112–119, 2013.

[3] M. A. Peña and J. L. G. Fierro, "Chemical structures and performance of perovskite oxides," *Chemical Reviews*, vol. 101, no. 7, pp. 1981–2018, 2001.

[4] A. V. Kovalevsky, S. Populoh, S. G. Patrício et al., "Design of $SrTiO_3$-based thermoelectrics by tungsten substitution," *The Journal of Physical Chemistry C*, vol. 119, no. 9, pp. 4466–4478, 2015.

[5] Q. Ji, L. Bi, J. Zhang, H. Cao, and X. S. Zhao, "The role of oxygen vacancies of ABO_3 perovskite oxides in the oxygen reduction reaction," *Energy & Environmental Science*, vol. 13, no. 5, pp. 1408–1428, 2020.

[6] J.-H. Kim, L. Mogni, F. Prado, A. Caneiro, J. A. Alonso, and A. Manthiram, "High temperature crystal chemistry and oxygen permeation properties of the mixed ionic-electronic conductors LnBaCo[sub 2]O[sub 5+δ] (Ln=Lanthanide)," *Journal of The Electrochemical Society*, vol. 156, no. 12, p. B1376, 2009.

[7] R. A. Cox-Galhotra, A. Huq, J. P. Hodges et al., "Visualizing oxygen anion transport pathways in $NdBaCo_2O_{5+\delta}$ by in situ neutron diffraction," *Journal of Materials Chemistry A*, vol. 1, no. 9, pp. 3091–3100, 2013.

[8] S. Afroze, A. Karim, Q. Cheok, S. Eriksson, and A. K. Azad, "Latest development of double perovskite electrode materials for solid oxide fuel cells: a review," *Frontiers in Energy*, vol. 13, no. 4, pp. 770–797, 2019.

[9] S. Sengodan, S. Choi, A. Jun et al., "Layered oxygen-deficient double perovskite as an efficient and stable anode for direct hydrocarbon solid oxide fuel cells," *Nature Materials*, vol. 14, no. 2, pp. 205–209, 2015.

[10] M. J. Akhtar and R. T. A. Khan, "Structural studies of $SrFeO_3$ and $SrFe_{0.5}Nb_{0.5}O_3$ by employing XRD and XANES spectroscopic techniques," *Materials Characterization*, vol. 62, no. 10, pp. 1016–1020, 2011.

[11] S. Kumar, G. D. Dwivedi, A. G. Joshi, S. Chatterjee, and A. K. Ghosh, "Study of structural, dielectric, optical properties and electronic structure of Cr-doped $LaInO_3$ perovskite nanoparticles," *Materials Characterization*, vol. 131, pp. 108–115, 2017.

[12] T. Broux, M. Bahout, J. M. Hanlon et al., "High temperature structural stability, electrical properties and chemical reactivity of $NdBaCo_{2-x}Mn_xO_{5+\delta}$ ($0 \le x \le 2$) for use as cathodes in solid oxide fuel cells," *Journal of Materials Chemistry A*, vol. 2, no. 40, pp. 17015–17023, 2014.

[13] M. Bahout, S. S. Pramana, J. M. Hanlon et al., "Stability of $NdBaCo_{2-x}Mn_xO_{5+\delta}$ (x = 0, 0.5) layered perovskites under humid conditions investigated by high-temperature in situ neutron powder diffraction," *Journal of Materials Chemistry A*, vol. 3, no. 30, pp. 15420–15431, 2015.

[14] G. Kim, S. Wang, A. J. Jacobson, L. Reimus, P. Brodersen, and C. A. Mims, "Rapid oxygen ion diffusion and surface exchange kinetics in $PrBaCo_2O_{5+x}$ with a perovskite related structure and ordered A cations," *Journal of Materials Chemistry*, vol. 17, no. 24, p. 2500, 2007.

[15] C. Lim, A. Jun, H. Jo et al., "Influence of Ca-doping in layered perovskite $PrBaCo_2O_{5+\delta}$ on the phase transition and cathodic performance of a solid oxide fuel cell," *Journal of Materials Chemistry A*, vol. 4, no. 17, pp. 6479–6486, 2016.

[16] Y. Zhang, H. Zhao, Z. Du, K. Świerczek, and Y. Li, "High-performance $SmBaMn_2O_{5+\delta}$ electrode for symmetrical solid oxide fuel cell," *Chemistry of Materials*, vol. 31, no. 10, pp. 3784–3793, 2019.

[17] S. Afroze, M. S. Reza, Q. Cheok, J. Taweekun, and A. K. Azad, "Solid oxide fuel cell (SOFC); A new approach of energy generation during the pandemic COVID-19," *International Journal of Integrated Engineering*, vol. 12, no. 5, pp. 245–256, 2020.

[18] T.-H. Lee, K.-Y. Park, N.-I. Kim et al., "Robust $NdBa_{0.5}Sr_{0.5}Co_{1.5}Fe_{0.5}O_{5+\delta}$ cathode material and its degradation prevention operating logic for intermediate temperature-solid oxide fuel cells," *Journal of Power Sources*, vol. 331, pp. 495–506, 2016.

[19] M. S. Reza, A. Ahmed, W. Caesarendra et al., "Acacia holosericea: an invasive species for bio-char, bio-oil, and biogas production," *Bioengineering*, vol. 6, no. 2, p. 33, 2019.

[20] M. S. Reza, S. N. Islam, S. Afroze et al., "Evaluation of the bioenergy potential of invasive Pennisetum purpureum through pyrolysis and thermogravimetric analysis," *Energy, Ecology and Environment*, vol. 5, no. 2, pp. 118–133, 2020.

[21] M. S. Reza, S. Afroze, M. S. A. Bakar et al., "Biochar characterization of invasive Pennisetum purpureum grass: effect of pyrolysis temperature," *Biochar*, vol. 2, no. 2, pp. 239–251, 2020.

[22] "Full article: preparation of activated carbon from biomass and its' applications in water and gas purification, a review," 2020, https://www.tandfonline.com/doi/full/10.1080/25765299.2020.1766799.

[23] F. Tonus, M. Bahout, V. Dorcet et al., "A-site order-disorder in the $NdBaMn_2O_{5+\delta}$ SOFC electrode material monitored in situ by neutron diffraction under hydrogen flow," *Journal of Materials Chemistry A*, vol. 5, no. 22, pp. 11078–11085, 2017.

[24] A. C. Tomkiewicz, M. A. Tamimi, A. Huq, and S. McIntosh, "Structural analysis of $PrBaMn_2O_{5+\delta}$ under SOFC anode conditions by in-situ neutron powder diffraction," *Journal of Power Sources*, vol. 330, pp. 240–245, 2016.

[25] A. K. Azad, J. H. Kim, and J. T. S. Irvine, "Structural, electrochemical and magnetic characterization of the layered-type $PrBa_{0.5}Sr_{0.5}Co_2O_{5+\delta}$ perovskite," *Journal of Solid State Chemistry*, vol. 213, pp. 268–274, 2014.

[26] J. A. Alonso, M. J. Martínez-Lope, A. Aguadero, and L. Daza, "Neutron powder diffraction as a characterization tool of solid oxide fuel cell materials," *Progress in Solid State Chemistry*, vol. 36, no. 1-2, pp. 134–150, 2008.

[27] H. Ding, Z. Tao, S. Liu, and J. Zhang, "A high-performing sulfur-tolerant and redox-stable layered perovskite anode for direct hydrocarbon solid oxide fuel cells," *Scientific Reports*, vol. 5, no. 1, Article ID 18129, 2015.

[28] A. Olszewska, Y. Zhang, Z. Du et al., "Mn-rich $SmBaCo_{0.5}Mn_{1.5}O_{5+\delta}$ double perovskite cathode material for SOFCs," *International Journal of Hydrogen Energy*, vol. 44, no. 50, pp. 27587–27599, 2019.

[29] S. Afroze, N. Torino, P. F. Henry, M. S. Reza, Q. Cheok, and A. K. Azad, "Neutron and X-ray powder diffraction data to determine the structural properties of novel layered perovskite $PrSrMn_2O_{5+\delta}$," *Data in Brief*, vol. 29, Article ID 105173, 2020.

[30] S. Afroze, N. Torino, P. F. Henry, M. Sumon Reza, Q. Cheok, and A. K. Azad, "Insight of novel layered perovskite $PrSrMn_2O_{5+\delta}$: a neutron powder diffraction study," *Materials Letters*, vol. 261, Article ID 127126, 2020.

[31] A. K. M. Zakaria, M. A. Asgar, S.-G. Eriksson et al., "Preparation of Zn substituted Ni-Fe-Cr ferrites and study of the crystal structure by neutron diffraction," *Materials Letters*, vol. 57, no. 26-27, pp. 4243–4250, 2003.

[32] A. K. Azad, A. Kruth, and J. T. S. Irvine, "Influence of atmosphere on redox structure of BaCe 0.9 Y 0.1 O 2.95 - insight from neutron diffraction study," *International Journal of Hydrogen Energy*, vol. 39, no. 24, pp. 12804–12811, 2014.

[33] X. Xu, Y. Xie, S. Ni, A. K. Azad, and T. Cao, "Photocatalytic H_2 production from spinels $ZnGa_2$–Cr O_4 ($0 \le x \le 2$) solid solutions," *Journal of Solid State Chemistry*, vol. 230, pp. 95–101, 2015.

[34] S. Afroze, N. Torino, M. S. Reza et al., "Structure-conductivity relationship of $PrBaMnMoO_{6-\delta}$ through in-situ measurements: a neutron diffraction study," *Ceramics International*, vol. 47, no. 1, p. 541, 2021.

[35] R. C. Nederland, "A profile refinement method for nuclear and magnetic structures," *Journal of Applied Crystallography*, vol. 2, pp. 65–71, 1969.

[36] "FullProf Suite Homepage," 2019, https://www.ill.eu/sites/fullprof/.

[37] S. Hull, R. I. Smith, W. I. F. David, A. C. Hannon, J. Mayers, and R. Cywinski, "The Polaris powder diffractometer at ISIS," *Physica B: Condensed Matter*, vol. 180-181, pp. 1000–1002, 1992.

[38] R. I. Smith, S. Hull, M. G. Tucker et al., "The upgraded Polaris powder diffractometer at the ISIS neutron source," *Review of Scientific Instruments*, vol. 90, no. 11, pp. 115101–115113, 2019.

[39] B. H. Toby and R. B. Von Dreele, "GSAS-II: the genesis of a modern open-source all purpose crystallography software package," *Journal of Applied Crystallography*, vol. 46, no. 2, pp. 544–549, 2013.

[40] A. M. Abdalla, S. Hossain, J. Zhou et al., "$NdBaMn_2O_{5+\delta}$ layered perovskite as an active cathode material for solid oxide fuel cells," *Ceramics International*, vol. 43, no. 17, pp. 15932–15938, 2017.

[41] F. Tonus, M. Bahout, V. Dorcet et al., "Redox behavior of the SOFC electrode candidate $NdBaMn_2O_{5+\delta}$ investigated by high-temperature in situ neutron diffraction: first characterisation in real time of an $LnBaMn_2O_{5.5}$ intermediate phase," *Journal of Materials Chemistry A*, vol. 4, no. 30, pp. 11635–11647, 2016.

[42] J. A. Mcallister and J. P. Attfield, "A variable temperature neutron diffraction study of the layered perovskite $YBaMn_2O_5$," *Journal of Materials Chemistry*, vol. 8, no. 5, pp. 1291–1294, 1998.

[43] R. D. Shannon, "Revised effective ionic radii and systematic studies of interatomic distances in halides and chalcogenides," *Acta Crystallographica Section A*, vol. 32, no. 5, pp. 751–767, 1976.

[44] A. Sciazko, Y. Komatsu, T. Shimura, and N. Shikazono, "Multiscale microstructural evolutions of nickel-gadolinium doped ceria in solid oxide fuel cell anode," *Journal of Power Sources*, vol. 478, Article ID 228710, 2020.

[45] J. Wang, F. Meng, T. Xia et al., "Superior electrochemical performance and oxygen reduction kinetics of layered perovskite $PrBa_xCo_2O_{5+\delta}$ ($x = 0.90$–1.0) oxides as cathode materials for intermediate-temperature solid oxide fuel cells," *International Journal of Hydrogen Energy*, vol. 39, no. 32, pp. 18392–18404, 2014.

[46] F. M. Aquino, D. M. A. Melo, R. C. Santiago et al., "Thermal decomposition kinetics of $PrMO_3$ (M = Ni or Co) ceramic materials via thermogravimetry," *Journal of Thermal Analysis and Calorimetry*, vol. 104, no. 2, pp. 701–705, 2011.

[47] F. Jin, H. Xu, W. Long, Y. Shen, and T. He, "Characterization and evaluation of double perovskites $LnBaCoFeO_{5+\delta}$ (Ln = Pr and Nd) as intermediate-temperature solid oxide fuel cell cathodes," *Journal of Power Sources*, vol. 243, pp. 10–18, 2013.

[48] R. Kannan, K. Singh, S. Gill, T. Fürstenhaupt, and V. Thangadurai, "Chemically stable proton conducting doped $BaCeO_3$ -No more fear to SOFC wastes," *Scientific Reports*, vol. 3, no. 1, pp. 1–5, 2013.

[49] A. A. Ansari, S. F. Adil, M. Alam et al., "Catalytic performance of the Ce-doped $LaCoO_3$ perovskite nanoparticles," *Scientific Reports*, vol. 10, no. 1, pp. 1–13, 2020.

[50] Z. Sun, W. Fan, Z. Liu, Y. Bai, Y. Geng, and J. Wang, "Improvement of dielectric performance of solid/gas composite insulation with YSZ/ZTA coatings," *Scientific Reports*, vol. 9, no. 1, pp. 1–12, 2019.

[51] J. Y. Huh, J. Lee, S. Z. A. Bukhari, J.-H. Ha, and I.-H. Song, "Development of TiO_2-coated YSZ/silica nanofiber membranes with excellent photocatalytic degradation ability for water purification," *Scientific Reports*, vol. 10, no. 1, pp. 1–12, 2020.

[52] X. Wang, H. Wang, and J. Shi, "Synthesis, characterization, and ceramic conversion of a liquid polymeric precursor to SiBCN ceramic via borazine-modified polymethylsilane," *Journal of Materials Science*, vol. 53, no. 16, pp. 11242–11252, 2018.

[53] S. Meyvel, P. Sathya, and G. Velraj, "Thermal characterization of archaeological pot sherds recently excavated in Nedunkur, Tamilnadu, India," *Cerâmica*, vol. 58, no. 347, pp. 338–341, 2012.

[54] A. M. Abdalla, S. Hossain, P. M. I. Petra, C. D. Savaniu, J. T. S. Irvine, and A. K. Azad, "Novel layered perovskite $SmBaMn_2O_{5+\delta}$ for SOFCs anode material," *Materials Letters*, vol. 204, pp. 129–132, 2017.

[55] X. Xu, J. Zhao, M. Li et al., "Sc and Ta-doped $SrCoO_{3-\delta}$ perovskite as a high-performance cathode for solid oxide fuel cells," *Composites Part B: Engineering*, vol. 178, p. 107491, 2019.

[56] J. H. Kim, Y. Kim, P. A. Connor, J. T. S. Irvine, J. Bae, and W. Zhou, "Structural, thermal and electrochemical properties of layered perovskite $SmBaCo_2O_{5+d}$, a potential cathode material for intermediate-temperature solid oxide fuel cells," *Journal of Power Sources*, vol. 194, no. 2, pp. 704–711, 2009.

[57] A. Tarancón, A. Morata, G. Dezanneau et al., "$GdBaCo_2O_{5+x}$ layered perovskite as an intermediate temperature solid oxide fuel cell cathode," *Journal of Power Sources*, vol. 174, no. 1, pp. 255–263, 2007.

[58] J.-H. Kim, F. Prado, and A. Manthiram, "Characterization of $GdBa_{1-x}Sr_xCo_2O_{5+\delta}$ ($0 \leq x \leq 1.0$) double perovskites as cathodes for solid oxide fuel cells," *Journal of the Electrochemical Society*, vol. 155, no. 10, p. B1023, 2008.

Hindawi
International Journal of Chemical Engineering
Volume 2020, Article ID 8834471, 9 pages
https://doi.org/10.1155/2020/8834471

Research Article

Preparation and Application of Aromatic Polymer Proton Exchange Membrane with Low-Sulfonation Degree

Yushan Gao,[1] **Zhidan Zhang**,[1] **Shuangling Zhong**,[1] **and Reza Daneshfar**[2]

[1]*College of Resources and Environment, Jilin Agricultural University, Changchun 130118, China*
[2]*Department of Petroleum Engineering, Petroleum University of Technology (PUT), Ahwaz, Iran*

Correspondence should be addressed to Shuangling Zhong; zhongs1235@163.com and Reza Daneshfar; reza_daneshfar@ut.ac.ir

Received 30 August 2020; Revised 23 September 2020; Accepted 30 September 2020; Published 14 October 2020

Academic Editor: Mohammad Hossein Ahmadi

4,4′-Dichlorodiphenylsulfone-3,3′-disulfonic acid (disodium) salt and 4,4′-difluorodiphenylsulfone were used as sulfonated monomer. 4,4′-Fluorophenyl sulfones were used as the nonsulfonated monomer. 4,4′-Dihydroxy diphenyl ether or 4,4′-thiodibenzenethiol was used as the comonomer. The sulfonated poly (aryl ether sulfone) (SPES) and sulfonated poly (arylene thioether sulfone) (SPTES) with sulfonation degree of 30% and 50% were successfully prepared by nucleophilic polycondensation. Two kinds of aromatic polymer proton exchange membranes were prepared by using sulfonated poly phthalazinone ether ketone (SPPEK) material and fluidization method. The performance of the prepared aromatic polymer proton exchange membrane was researched by the micromorphology, ion exchange capacity, water absorption and swelling rate, oxidation stability, tensile properties, and proton conductivity. Experimental results show that there is no agglomeration in the prepared aromatic polymer proton exchange membrane. The ion exchange capacity is 0.76–1.15 mmol/g. The water absorption and swelling rate increase with the increase of sulfonation degree. The sulfonated poly (aryl ether sulfone) membrane shows better oxidation stability than sulfonated poly (aryl sulfide sulfone). They have good mechanical stability. The prepared aromatic polymer proton exchange membrane with low sulfonation degree has good performance, which can be widely used in portable power equipment, electric vehicles, fixed power stations, and other new energy fields.

1. Introduction

Energy is an important material basis for the survival and development of human society. With the development of society, the problems of environmental pollution, ecological damage, and climate change caused by the production, conversion, and use of fossil energy have posed a serious threat to human survival and development. In order to solve the contradiction between economic development, energy shortage, and environmental pollution, it is urgent to develop a clean, efficient, and sustainable new energy.

Fuel cell (FC) is considered as a new generation of power system with energy revolution significance after steam engine and internal combustion engine. It converts the chemical energy in fuel and oxidant directly into electric energy without combustion. Because it is not limited by Carnot cycle, its energy conversion efficiency reaches 40%~60%, and the actual use efficiency is 2~3 times of that of ordinary internal combustion engine. Fuel cell is also a kind of environment-friendly power generation device [1]. It hardly emits pollutants such as SOx and NOx to the outside world during its working process. It is these outstanding advantages that arouse people's extensive interest in fuel cell. The development of fuel cell has experienced a rather tortuous and long historical process. As early as 1839, grove successfully carried out the reverse reaction of electrolytic water, creating the world's first fuel cell model. Later, the slow progress of electrode reaction kinetics and the success of thermal engine process delayed the research of fuel cell for nearly a century, until the successful application of fuel cells in space flight has aroused people's research interest again [2], and the breakthrough progress of electrochemistry has also laid a solid theoretical foundation for the development of fuel cells. In the 90s of the 20th century, in the atmosphere

of energy shortage and serious environmental pollution, people gradually realized that fuel cell, as a kind of sustainable development clean energy, has incomparable advantages, thus setting off a new round of fuel cell research upsurge.

Fuel cells can be classified according to different standards. At present, the most common classification method is based on electrolyte, which can be roughly divided into five categories: alkaline fuel cell, phosphoric acid fuel cell, solid oxide fuel TV, molten carbonate fuel cell, and proton exchange membrane fuel cell. As the fifth generation fuel cell, proton exchange membrane fuel cell (PEMFC) has the advantages of high power density, high current density, low operating temperature, and fast start-up speed. In addition, due to the use of polymer as electrolyte, there are no electrolyte leakage and corrosion problems, less environmental pollution, and longer service life [3]. Proton exchange membrane fuel cell (PEMFC) can be used not only in the construction of decentralized power plants, but also as a mobile power source. Proton exchange membrane fuel cell research has become the mainstream of a variety of fuel cell research tide, and breakthroughs have been made in key materials and battery pack [4–7], which is expected to be commercialized as soon as possible.

Proton exchange membrane fuel cell (PEMFC) has a wide application prospect in the field of portable power equipment, electric vehicles, and fixed power stations due to its high energy density, high energy conversion efficiency, environmental friendliness, flexibility, and portability. In recent years, researchers have devoted themselves to developing PEM with high performance and low cost. Sulfonated aromatic polymers, such as sulfonated polyetherketones and sulfonated polyethersulfones, have excellent film-forming properties, good thermal stability, and high proton conductivity, which makes them promising as alternative materials for PEMFC applications. Similar to Nafion, sulfonated aromatic polymers also exhibit nano phase separation between hydrophobic main chain and hydrophilic side chain. However, compared with Nafion, sulfonated aromatic polymer membranes have narrower ion channel size, more "dead ends," and phase discontinuities, resulting in lower proton conductivity [8]. However, in order to obtain a higher degree of sulfonation in hot water, a higher degree of sulfonation strategy will lead to higher proton conductivity. Bai et al. prepared sulfonated poly (aryl sulfide sulfone) copolymer with high sulfonation degree. When the sulfonation degree reached 70%, the water absorption rate of the polymer membrane in hot water at 80°C exceeded 800% and even dissolved in water at 90°C; the sulfonated polyether ether ketone with sulfonation degree of 62.7% prepared by Zhang et al. was also dissolved in hot water at 70°C. How to balance the proton conductivity and dimensional stability is the main bottleneck restricting the development of sulfonated aromatic polymer proton exchange membrane [9]. In order to overcome these problems, researchers have adopted a variety of strategies to adjust the performance of the membrane and have carried out a lot of research on side chain type, block type, and composite type proton exchange membrane. Although the performance of the membrane has been improved by these methods, the preparation method is more cumbersome, especially difficult to meet the requirements of industrialization. In this paper, two kinds of sulfonated aromatic polymers with low sulfonation degree were prepared by simple nucleophilic polycondensation and changing the element composition of the main chain of the polymer. They were sulfonated poly (arylene thioether sulfone) (SPTES) and sulfonated poly (aryl ether sulfone) (SPES). The proton exchange membranes of the two kinds of low sulfonated aromatic polymers were compared, and the aromatic polymer protons with different properties were obtained. Exchange membranes can be used in applications with different requirements.

2. Materials and Methods

2.1. Main Raw Materials. Sulfonated poly phthalazinone ether ketone (SPPEK) and 4,4′-fluorophenyl sulfones (99% purity) were purchased from Dalian Baolimo New Materials Co., Ltd. Isopropanol recrystallization, 4,4′-thiodibenzenethiol (98% purity), phenol, 4,4′-oxybis- (98% purity), and potassium carbonate anhydrous (99% purity) were purchased from Sinopharm Chemical Reagent Co., Ltd., Beijing, China. N-Methyl pyrrolidone (high analytical grade) and isopropanol (high analytical grade) were purchased from Tianjin Fuchen Chemical Reagent Factory; Sulfolane (purity ≥ 99%) was purchased from Sinopharm Chemical Reagent, Co., Ltd., Beijing, China. Sodium chloride (high analytical grade) was purchased from Tianjin Fuchen Chemical Reagent Factory. Other reagents and solvents were of high analytical grade, which can be directly applied. The infrared spectrum characterization results of SPPEK of raw materials in this paper are shown in Figure 1. The number marked in the figure is the telescopic vibration peak.

2.2. Main Instruments. Nuclear magnetic resonance instrument, AVANCE 400, was purchased from Bruker BioSpin AG, Switzerland. Synchronous thermal analyzer, SDT/Q600, was purchased from TA Instruments, USA. Fourier transform infrared spectrometer, VECTOR 22, was purchased from Bruker, Germany. Field emission scanning electron microscope, Nova NanoSEM 450, was purchased FEI Company, USA. Electrochemical work station, CHI660D, was purchased from Shanghai Chenhua Instrument Co., Ltd. Microcomputer controlled electronic universal testing machine, CMT6104, was purchased from Shenzhen Century Tianyuan Instrument Co., Ltd.

2.3. Preparation of Proton Exchange Membrane. The transparent and strong proton exchange membranes of two polymers were prepared by tape casting method. The sulfonated poly (aryl ether sulfone) (SPES) and sulfonated poly (arylene thioether sulfone) (SPTES) with sulfonation degrees of 30% and 50% were prepared. SPES-50 and SPTES-50 were used as an example. Under the protection of

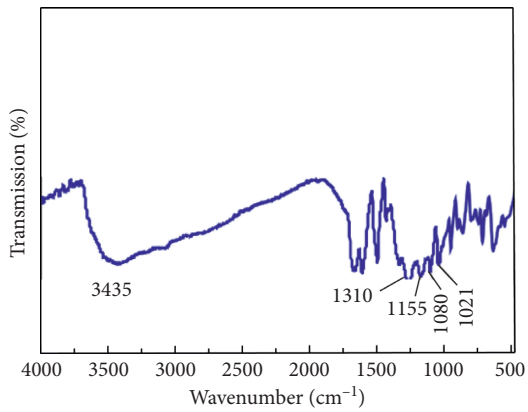

Figure 1: SPPEK Infrared characterization.

nitrogen, 2.29 g (5 mmol) of 3,3′-disulfonic acid salt-bis(4-chlorophenyl) sulfone, 1.259 g (5 mmol) of 4,4′- difluorodiphenyl sulfone, and 25 ml sulfolane (TMS) were successively added to the dry three-port flask equipped with magnetic stirrer, condenser, and water separator. When SPES-50 was synthesized, 2.02 g (10 mmol) of 4,4′-dihydroxydiphenyl ether was added. In the synthesis of SPTES-50, 2.504 g (10 mmol) of 4,4′-thiodibenzenethiol was added. They were stirred at room temperature for 30 min to make the monomer fully mixed. Two grams (3.312 g when SPTES-50 was synthesized) of anhydrous potassium carbonate and 10 ml of toluene were slowly heated to 160°C with water for three hours. The toluene was evaporated out of the reaction system and then it was heated to 180°C for twelve hours. After the reaction, the viscous reaction liquid was naturally cooled to room temperature [9] and poured into the mixed solution of methanol and glacial acetic acid (V (methanol): V (glacial acetic acid) = 8 : 2 precipitation). The polymers were shredded, filtered, and washed with hot deionized water for several times, and then they were extracted by Soxhlet extraction with methanol for 72 h and dried in a vacuum oven at 100°C for 24 h to obtain the dried polymer SPES-50 or SPTES-50. The yield of SPTES is 90% and the yield of SPES is 92%.

2.4. Sulfonation Reaction Process. SPPEK powder was dried in vacuum at 105°C for 24 hours to remove the water absorbed by the sample. In a completely dry four-port flask with a constant pressure drop funnel, SPPEK powder was dissolved in chloroform to produce a chloroform solution of 0.1 g/ml. After full dissolution, a certain proportion of concentrated sulfuric acid and fuming sulfuric acid were added to the solution with a constant pressure and low drop funnel for sulfonation [10]. The degree of sulfonation was controlled by controlling the reaction conditions. After the reaction, the mixture was poured into a large amount of ice and water mixture and precipitated to obtain fibrous precipitate. The residual acid was removed by repeated washing with water ions, and then it was filtered and dried to obtain sulfonated poly phthalazinone ether ketone (SPPEK). The sulfonation reaction was controlled by nucleophilic polycondensation.

2.5. Performance Test of Proton Exchange Membrane

2.5.1. Microscopic Appearance of Aromatic Polymer Proton Exchange Membrane. Before FEI sirion-200 scanning electron microscope was used to observe the micromorphology of the membrane, the samples were sputtered and sprayed with gold to prevent the discharge phenomenon.

2.5.2. Ion Exchange Capacity. Ion exchange capacity (IEC) is the amount of -SO_3H group substance contained in a unit mass polymer, and its unit is mmol/g. The equivalent weight (EW) is the reciprocal of ion exchange capacity. There are many methods to measure IEC value. In this experiment, acid-base back titration is used to measure IEC value [11]. Firstly, it is necessary to prepare 0.01 mol/L NaOH standard solution and 0.01 mol/L hydrochloric acid standard solution according to GB/T-601-2002. After accurately weighing and taking SPPEK dry film with certain quality, we cut it up and put it into a certain volume of NaOH standard solution for soaking for 24 hours and then titrated the blank solution. By repeating the measurement for three times, we take the average value. The formula of calculating the IEC value is shown as follows:

$$\mathrm{IEC} = V_{\mathrm{NaOH}} \times C_{\mathrm{NaOH}} - V_{\mathrm{HCl}} \times C_{\mathrm{HCl}}. \quad (1)$$

In Formula 1, C_{NaOH} denotes the molar concentration of NaOH standard solution. C_{HCl} denotes the molar concentration of HCl standard solution. V_{NaOH} denotes the volume of NaOH standard solution. V_{HCl} denotes the volume of HCl standard solution.

The sulfonation degree is the percentage of -SO_3H group in the total number of basic chain segments of polymer. One mol of molecular chain segment of SPPEK participates in the cyclization reaction (the molar mass of SPPEK is M_{PPEK}). The degree of sulfonation is represented by DS. When DS is less than 1, the chain segment of DS mol is sulfonated, and the mass of sulfonated polymer is DS ($M_{\mathrm{PPEK}} + 80$). Other (1-DS) mol chain segments do not contain -SO_3H groups, and their mass is (1-DS) M_{PPEK}. Thus, the formula of ion exchange capacity of SPPEK is

$$\mathrm{IES} = \frac{\mathrm{DS}}{\mathrm{DS}\left(M_{\mathrm{PPEK}} + 80\right) + (1 - \mathrm{DS})M_{\mathrm{PPEK}}}. \quad (2)$$

If more than one sulfonation site is replaced by -SO_3H group on the basic chain segment of each polymer, DS is more than 1. Formula (3) can be obtained by formula (2):

$$\mathrm{IES} = \frac{\mathrm{DS}}{M_{\mathrm{PPEK}} + 80\,\mathrm{DS}}. \quad (3)$$

The sulfonation degree can be obtained by ion exchange capacity.

The sulfonation degree of polymer is affected by the activity of sulfonating agent, concentration of polymer in sulfonating agent, reaction time, reaction temperature, and other factors [12], so different sulfonation degree products can be prepared by controlling sulfonation conditions.

2.5.3. Test of Water Absorption and Swelling. The water absorption and swelling rate of membrane are analyzed by the change of its mass and size. A 2 cm × 3 cm dry film is taken, and the mass of dry film is weighed. After soaking in deionized water at different temperatures for 24 h, it is necessary to make the film fully absorb water and swell, and then the mass and area of film are recorded at different temperatures, respectively [13]. The water absorption and swelling rate of membrane are calculated by

$$\text{Water absorption rate} = \frac{W_{\text{wte}} - W_{\text{dry}}}{W_{\text{dry}}} \times 100\%,$$
$$\text{Swelling rate} = \frac{A_{\text{wet}} - A_{\text{dry}}}{A_{\text{dry}}} \times 100\%. \quad (4)$$

In the previously mentioned formulas, W_{dry} and W_{wet} are, respectively, the mass of dry film and the mass of wet film after full water absorption and swelling, g. A_{dry} and A_{wet} are the area of dry film and the area of wet film after full water absorption and swelling, cm^2, respectively.

2.5.4. Oxidation Stability Test. Firstly, we immersed the 2 cm × 2 cm membrane in Fenton reagent (H_2O_2 solution containing 2 mg/kg $FeSO_4$ 3%) and kept it heated in water bath at 80°C [14]. After that, we recorded the remaining mass of membrane immersed in Fenton reagent for 1 h and the time of complete dissolution of membrane.

2.5.5. Tensile Property Test. According to GB-1040.3-2006 standard, the tensile properties of membrane samples were tested. The loading rate was 2 mm/min, and the formula to calculate the tensile strength was shown as follows:

$$\sigma_t = \frac{p}{b \cdot d}. \quad (5)$$

In formula (1), σ_t denotes the tensile strength of membrane. P denotes the maximum load, the breaking load and the yield load. b denotes the width of sample. d denotes the thickness of sample.

The formula of the breaking elongation of specimen is as follows:

$$\varepsilon_t = \frac{L - L_0}{L_0} \times 100\%. \quad (6)$$

In formula (2), ε_t denotes the breaking elongation. L_0 denotes the original line marking distance of sample. L denotes the distance between line markings when the sample breaks.

The formula of elastic modulus is shown as follows:

$$E_t = \frac{\sigma_t}{\varepsilon_t}. \quad (7)$$

In formula (7), E_t denotes the elastic model. σ_t denotes the tensile strength. ε_t denotes the elongation at break.

2.5.6. Proton Electroconductibility Test. The conductivity property of proton exchange membrane is generally characterized by conductivity. However, the measurement of conductivity is not as simple, convenient, and intuitive as liquid electrolyte. The carrier in proton exchange membrane is hydronium proton, and the carrier in conductor and electrode is electron. In the measurement process, the charge transfer may appear in the interface between electrode and proton exchange membrane [15], thus forming a double electric layer. In addition, the charge transfer impedance will be formed at the interface between the electrode and the proton exchange membrane, so the conductivity of proton exchange membrane cannot adopt the DC resistance method but should select the AC impedance method. The complex concentration polarization and ion accumulation at the electrode-proton exchange interface can be eliminated by AC impedance method, and the influence of charge transfer resistance on the electrode proton exchange interface can be avoided. We used EG&PARRC Potentiostat/Galvanostat Model 273 electrochemical workstation to test the conductivity of proton membrane. The test frequency ranged from 10 to 10^5 Hz, and the AC microdisturbance amplitude was 5 mV. During the test, two stainless steel inert electrodes were used to act on the cathode and anode, the test membrane was clamped between the cathode and the anode, and then the membrane and the electrode were fixed with polytetrafluoroethylene sleeve. After that, the stainless wire was connected to the instrument. The schematic diagram of test device and battery device is shown in Figure 2.

Before the test, the proton exchange membrane to be tested is immersed in deionized water for 24 hours, so that it is fully hydrated. And then, the proton is measured in deionized water.

The self-resistance Rb value of membrane is the abscissa value corresponding to the intersection of high-frequency semicircle and low-frequency straight line in Cole-Cole curve. If the test frequency is not too high or the system conductivity is high, the high-frequency semicircle does not appear, and the AC impedance curve is approximately a straight line in the high frequency [16]. Thus, Rb is the intersection of the straight line and the abscissa. The conductivity is calculated by formula (4):

$$\delta = \frac{L}{R_b \cdot S} \times 100\% \quad (8)$$

In formula (4), L denotes the membrane size between the two electrodes. R_b denotes the actual contact area of the two electrodes. S denotes the measured membrane resistance.

3. Results

3.1. Micromorphology of Aromatic Polymer Proton Exchange Membrane. The SEM photos of the surface direction and cross-section direction of proton exchange membrane of aromatic polymer are shown in Figure 3, where the graticule of electron microscope is 2 μm.

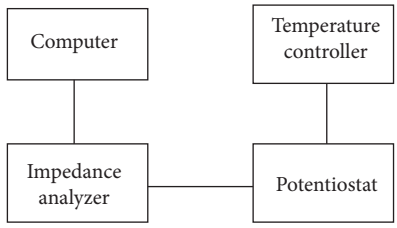

Figure 2: Schematic diagram of the proton conductivity test device.

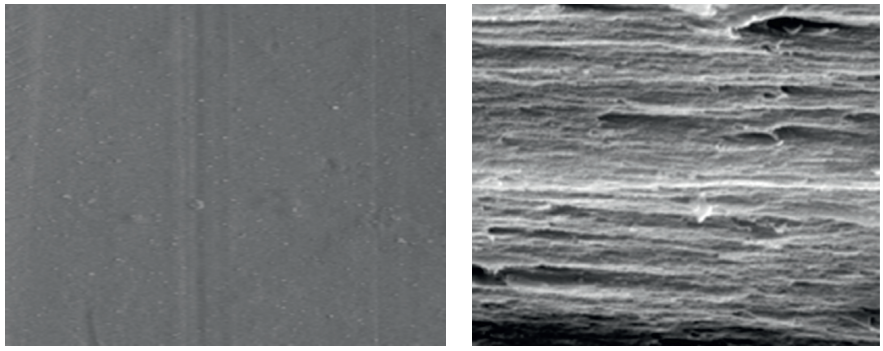

(a) (b)

Figure 3: SEM photo of 20% aromatic polymer proton exchange membrane. (a) Surface orientation before sulfonation. (b) Surface orientation after sulfonation.

According to experimental results in Figure 2, we can see that the reaction of aromatic polymer proton exchange membrane after the low-sulfonation reaction is relatively uniform without agglomeration. The structure of aromatic polymer proton exchange membrane with low sulfonation degree is fine and close. Thus, the effectiveness of the sulfonation reaction can be proved.

3.2. Ion Exchange Capacity. The changes of sulfonation degree of aromatic polymer proton exchange membrane in different reaction conditions are shown in Table 1.

Table 1 shows that when concentrated sulfonic acid was only used as sulfonating agent to react at room temperature for 24 hours, SPPEK was basically not sulfonated. When the reaction temperature was raised to 50°C for 24 hours, only SPPEK products with low sulfonation degree were obtained. Therefore, it was difficult to obtain SPPEK products with high sulfonation degree only by concentrated sulfuric acid. In this experiment, the mixture of fuming sulfur and concentrated sulfuric acid was used for sulfonation.

The ion exchange capacity of four aromatic polymer proton exchange membranes obtained by acid-base titration was tested. The theoretical value of ion exchange capacity was calculated by formula (1), and then the value was compared with Nafion-117 membrane. The test value and theoretical value of ion exchange capacity were shown in Table 2.

Table 2 shows that the IEC test value of copolymers ranges between 0.76 and 1.15 mmol/g. Due to the exchange equilibrium in the process of proton exchange, the H^+ in polymer cannot be completely replaced, and there are some residues. Meanwhile, there are absolute errors in the measurement, so the determination result is slightly lower than the theoretical value, but it is basically consistent with the theoretical value. The reaction is relatively completed. With the increase of sulfonation degree, more and more $-SO_3H$ groups are introduced into the main chain of polymer, and the IEC value of membrane is also increased.

3.3. Water Absorption and Swelling Rate of Membrane. As the carrier of proton transport, water content will influence the proton transport process, so the water absorption of the membrane has an important impact on the proton transport performance of proton exchange membrane. In addition, the water absorption affects the swelling performance of membrane, so as to influence the mechanical properties and stability of the membrane. Table 3 shows the test results of water absorption and swelling rate of polymer membrane.

From the experimental results in Table 3, we can see that the water absorption of SPES-50 and SPTES-50 membranes is much higher than that of Nafion-117 membrane. With the increase of temperature, the water absorption of the membrane shows an increasing trend. Because the increase of temperature, the molecular movement is intensified, and the movement of macromolecular chain is more active. Finally, the water absorption is increased. Due to the low sulfonation degree of SPES-30 and SPTES-30, the water absorption has little change with the increase of temperature. The water absorption of SPES-50 and SPTES-50 increases rapidly after the temperature is higher than 58°C, reaching 137.5% and 104.7%, respectively, at 80°C. SPES has higher

Table 1: Effect of reaction conditions on the degree of sulfonation.

SPPEK quality (g)	Sulfuric acid (ml)	Time (h)	Oleum (ml)	Temperature (°C)	IEC (mmol/g)	DS (%)
6	55	24	0	RT	≈0	≈0
6	55	48	0	RT	0.75	7
6	55	4	0	60	0.71	12
6	30	4	30	RT	0.63	20
6	0	4	30	60	1.06	36
6	0	8	30	60	1.08	48
6	0	24	30	60	1.12	56
6	0	6	30	60	1.14	67
12	0	6	50	60	1.15	85
12	0	7	50	60	1.15	91

Table 2: Ion exchange capacity of the aromatic polymer proton exchange membrane.

Polymers	Measurements (mmol/g)	Theoretical value (mmol/g)
SPES-30	1.86	1.85
SPES-50	2.12	2.11
SPTES-30	2.28	2.27
SPTES-50	2.06	2.05
Nafion-117	2.31	2.30

Table 3: Water absorption and swelling ratio of different polymer films.

	Polymers (°C)	SPES-30	SPES-50	SPTES-30	SPTES-50	Nafion-117
Bibulous rate (%)	18	16.8	50.7	11.2	35.7	16.7
	38	17.5	59.5	12.5	41.3	
	58	18.7	76.5	13.5	55.8	
	78	23.9	137.5	16.3	104.7	27.5
Swelling rate (%)	18	15.9	40.2	3.9	7.4	12.6
	38	17.2	50.1	5.9	12.5	
	58	18.8	73.8	7.2	24.5	
	78	22.9	115.4	9.8	69.8	20.8

water absorption than SPTES. This may be due to the formation of conjugated structure of sulfur atom, benzene ring, and sulfone group in SPTES, but the structure hinders the free movement of macromolecular chain and limits the water absorption of sulfonic acid group. The size stability is also an important index of fuel cell performance. Table 3 shows the test results of water absorption and swelling ratio of SPES and SPTES membranes and the relevant data of Nafion-117. With the increase of temperature, the swelling rate of all membranes is increased. Due to the higher water absorption, the swelling ratio of SPES-50 and SPTES-50 is higher than that of Nafion-117. Compared with the results of water absorption, the swelling rate of sulfonated polymer is consistent with the increasing trend of water absorption of sulfonated polymer. SPES has higher swelling ratio than SPTES. At 78°C, the swelling ratios of SPES -50 and SPTES-50 are 115.4% and 69.8%, respectively. SPTES-50 has lower swelling rate than SPES-30 before 50°C. The reason is the conjugation effect of sulfur atom and benzene ring in SPTES. At low temperature, the lack of chain segment movement limits the swelling of SPTES. When the temperature rises, the swelling of polymer breaks through the limit of insufficient chain movement with the increase of water absorption. Thus, the amount of water absorption dominates the swelling rate of polymer, so the swelling rate of SPTES-50 is more than SPES-30 when it rises to a certain temperature. Through the test of water absorption and swelling rate, it is found that there is a certain correlation between the swelling rate and water absorption, but there are many factors influencing the water absorption and swelling degree of sulfonated polymer. This experiment shows that the water absorption and swelling rate of polymer can be affected by increasing the intermolecular force.

3.4. Oxidation Stability of Membrane. It is unavoidable for proton exchange membrane to contact with air during the processing, storage, and use, and some free radicals such as HOO· and HO· will be formed in positive pole under the operating environment of fuel cell. It is easy to lead to the degradation of membrane materials, so the oxidation stability is another important performance index of proton exchange membrane.

Table 4 shows the residual mass ratio and the time of complete dissolution of polymer film in Feton's solution at 80°C for 1 h.

After 1 h oxidation in Feton's reagent, the residual mass of SPES-30 is 95.8% and the residual mass of SPES-50 is 93.2%, while the residual mass of SPTES-30 is 105.7% and

Table 4: Oxidation stability of the film.

Polymers	Remaining mass ratio (%)	Complete dissolution time (h)
SPES-30	95.8	>12
SPES-50	93.2	2.14
SPTES-30	105.7	>12
SPTES-50	99.8	2.68
Nafion-117	98.9	0

Table 5: Comparison of tensile properties of different aromatic polymer proton exchange membranes.

Polymers	Maximum stress (MPa)	Maximum strain (%)	Young's modulus
SPES-30	25.38	8.49	0.28
SPES-50	43.52	5.85	0.74
SPTES-30	43.52	3.45	2.42
SPTES-50	44.85	3.75	1.85
Nafion-117	28.46	3.85	0.08

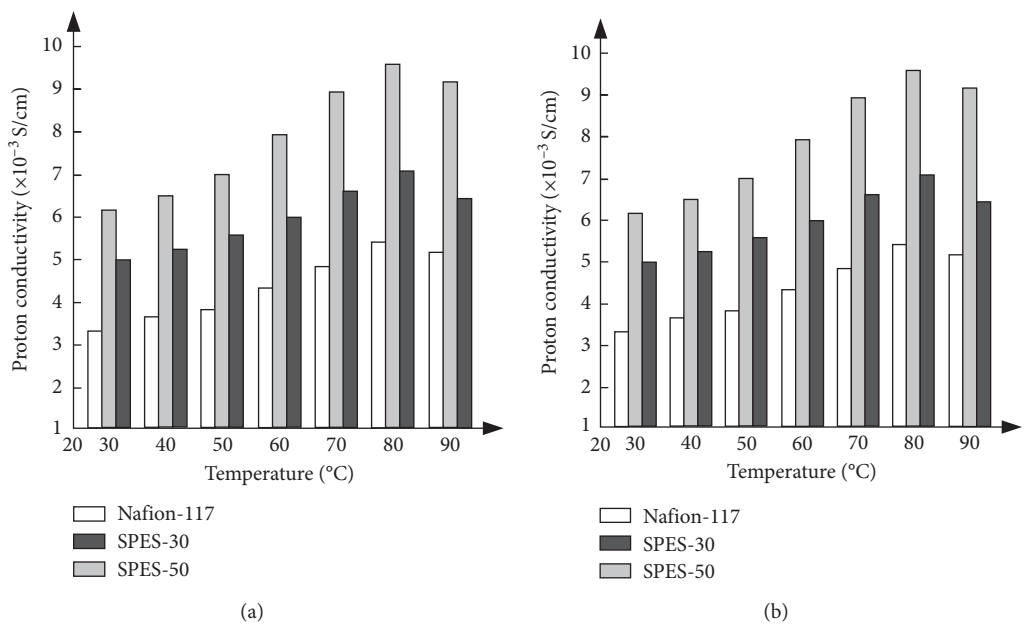

Figure 4: Effect of temperature on the proton conductivity of the aromatic polymer proton exchange membrane. (a) SPES membrane. (b) SPTES membrane.

the residual mass of SPTES-50 is 99.8%. These show an increasing trend in mass. SPES-50 and SPTES-50 are dissolved after 2.14 h and 2.68. SPES-30 and SPTES-30 membranes maintain complete after 12 h. The mass of SPTES membrane after 1 h oxidation is increased. This may be related to the C-S bond in polymer. The oxidation of thioether bond to sulfoxide bond results in the increase of membrane weight. The thioether group is converted into sulfoxide group by reaction with free radicals, so as to avoid the direct attack of hydroxyl radicals on the main chain of polymer. Therefore, SPTES membrane has better oxidation stability than that of SPTES. The increase of sulfonation degree of polymer leads to the decrease of oxidation stability of polymer. This is mainly because the oxidation attack of free radicals (HO· and HOO·) appears in the hydrophilic region, and more sulfonic groups lead to the poor oxidation stability of polymer.

3.5. Tensile Properties. The tensile properties of aromatic polymer proton exchange membrane were tested, and the tensile properties of Nafion-117 membrane were compared with it. The comparison results are shown in Table 5.

The following conclusions can be drawn from the experimental results in Table 5. Compared with Nafion-117 membrane, SPES membrane and SPTES membrane have higher tensile strength and lower elongation at break, so that they have better mechanical stability.

3.6. Proton Conductivity. The proton conductivity is one of the main indexes to evaluate the proton exchange performance. The proton conductivity of SPI-X membrane is measured by AC impedance method. The change curves of conductivity of SPES membrane, SPTES membrane, and Nafion-117 membrane with temperature are shown in Figure 3. Before the test, the aromatic polymer proton

exchange membrane was processed with acid for 24 hours, and thus it changed from salt form to proton form, and then it was kept in water for 24 hours to make the membrane fully hydrated (Figure 4).

At room temperature, the conductivity increased with the increase of sulfonation degree, and the conductivity of the SPES-30 membrane reached 5.1×10^{-3} S/cm. The proton conductivity of Nafion-117 membrane was always lower than that of the SPES-30 membrane under similar conditions. With the increase of temperature, SPES-30 increases the conductivity of membrane, causes molecular motion to accelerate, and promotes -SO_3H groups in the hydrated membrane and the formation of the ion clusters, whereas low temperature, relative to the high temperature, can provide more energy, on the side chain -SO_3H groups can be wandering degree increases, eventually leading increase in the speed of the proton transfer, and thus the proton conductivity increases. When the test temperature was high, the electrical conductivity of SPES-30 film reached a maximum of 6.8×10^{-3} S/cm at 87°C due to the influence of high temperature dehydration. The conductivity of SPES-30 membrane began to decrease at 80°C, which was due to the decrease of the number of -SO_3H groups and the decreased water retention capacity of the membrane. Proton conductivity was strongly dependent on the water content in the membrane, and the evaporation of water at high temperature had a more significant effect on the SPES membrane with a lower degree of sulfonation. The data viewing method of SPES-50 membrane, SPTES-30 membrane, SPTES-50 membrane, and Nafion-117 membrane is the same as that of SPES-30 membrane. According to the experimental data, the proton conductivity of the proton exchange membrane obtained in this paper is higher than that of the traditional proton exchange membrane, indicating that the research results in this paper have effective application results.

4. Conclusions

Through simple nucleophilic polycondensation, we have successfully prepared two kinds of sulfonated aromatic copolymers with low sulfonation degree: sulfonated poly (aryl ether sulfone) (SPES) and sulfonated poly (arylene thioether sulfone) (SPTES). Meanwhile, we can control the sulfonation degree of two kinds of polymers accurately. Both membranes are transparent and tough, and they have good mechanical properties. Their tensile strength is more than 40 MPa. Water absorption, swelling, and IEC are increased with the increase of sulfonation degree. The IEC of SPES-50 is 2.12 mequiv/g, while that of SPTES-50 is 2.06 mequiv/g. SPES and SPTES membranes show good comprehensive properties, so they have good future in application of proton exchange membrane fuel cell.

Data Availability

No datasets were generated or analyzed during the current study.

Conflicts of Interest

The authors declare that they have no conflicts of interest.

Acknowledgments

The research was supported by National Natural Science Foundation of China (no. 21106052) and Natural Science Foundation of Jilin Provincial Science and Technology Department (no. 20180101072 JC).

References

[1] Z. Wang, Y. Bin, and S. Liu, "Comparative analysis of simulations of two segmented models for proton exchange membrane fuel cell," *Journal of Power Supply*, vol. 17, pp. 177–187, 2019.

[2] Z. Wang, M. Hou, and Y. Jiang, "Preparation and properties of SPEEK/Nafion composite proton exchange membranes," *Chinese Journal of Power Sources*, vol. 42, pp. 50–54, 2018.

[3] L. Xu, Q. Zhang, and D. Liu, "Preparation of microporous-mesoporous ZSM-5 molecular sieve by alkali treatment and its application in alkylation reaction of phenol with tert-butanol," *Journal of Jilin University (Science Edition)*, vol. 57, pp. 433–437, 2019.

[4] J. Zhang, G. Shi, and W. Wang, "The application of VENT in the study of thermal comfort of straight-tunne thermal kang," *Computer Simulation*, vol. 36, pp. 284–289, 2019.

[5] W. Dong, D. M. Guiver, and Y. M. Lee, "Hydrocarbon-based polymer electrolyte membranes: importance of morphology onion transport and membrane stability," *Chemical Reviews*, vol. 117, p. 4759, 2017.

[6] L. Steve, C. Liu, and C. Tu, "Synthesis and properties of ABPPQ for high-temperature proton exchange membrane fuel cells," *Polymer Bulletin*, vol. 75, pp. 1–11, 2018.

[7] P. Jing, Q. Wang, B. Wang, X. Gao, Y. Zhang, and H. Wu, "Encapsulating yolk-shell FeS2@carbon microboxes into interconnected graphene framework for ultrafast lithium/sodium storage," *Carbon*, vol. 159, pp. 366–377, 2020.

[8] M. A. Imran, G. He, X. Wu, X. Yan, T. Li, and A. S. Khan, "Fabrication and characterization of sulfonated polybenzimidazole/sulfonated imidized graphene oxide hybrid membranes for high temperature proton exchange membrane fuel cells," *Journal of Applied Polymer Science*, vol. 136, no. 34, p. 47892, 2019.

[9] J. Zhou, P. Chen, Q. Shi, R. Wang, X. Chen, and Z. An, "Cross-linked poly(arylene ether sulfone)s with side-chain aromatic benzyltrimethyl ammonium for anion-exchange membranes," *Polymer Bulletin*, vol. 74, no. 10, pp. 4329–4348, 2017.

[10] J. R. Rowlett, V. Lilavivat, A. T. Shaver et al., "Multiblock poly(arylene ether nitrile) disulfonated poly(arylene ether sulfone) copolymers for proton exchange membranes: Part 2 electrochemical and H2/Air fuel cell analysis," *Polymer*, vol. 122, pp. 296–302, 2017.

[11] T. Kim, Y. Kwon, and J. Lee, "Development of hydrophilicity on the proton exchange using sulfonic acid on PEEK in the presence of water: a density functional theory study," *Theoretical Chemistry Accounts*, vol. 136, p. 130, 2017.

[12] A. R. Kim, M. Vinothkannan, J. S. Kim, and D. J. Yoo, "Proton-conducting phosphotungstic acid/sulfonated fluorinated block copolymer composite membrane for polymer electrolyte fuel cells with reduced hydrogen permeability," *Polymer Bulletin*, vol. 75, no. 7, pp. 2779–2804, 2018.

[13] S. Pierre, J. R. Duke, T. J. H. Hele, and N. Ananth, "A mapping variable ring polymer molecular dynamics study of condensed phase proton-coupled electron transfer," *The Journal of Chemical Physics*, vol. 147, no. 23, p. 234103, 2017.

[14] G. Jason, J. Brendel, and N. Cameron, "Imaging proton transport in giant vesicles through cyclic peptide-polymer conjugate nanotube transmembrane ion channels," *Macromolecular Rapid Communications*, vol. 39, Article ID 1700831, 2018.

[15] Y.-H. Cai, L.-S. Zhao, and L.-L. Tian, "Investigating the crystallization, melting behavior, and thermal stability of poly(l-lactic acid) using aromatic isoniazid derivative as nucleating agent," *Polymer Bulletin*, vol. 74, no. 9, pp. 3751–3764, 2017.

[16] A. Yu, S. Eliseeva, and A. Buryak, "The influence of experimental factors on the sorption of vanillin by a macroporous highly basic anion exchanger with a low degree of cross-linking," *Colloid Journal*, vol. 81, pp. 621–625, 2019.